IMAGING VORTEX DYNAMICS IN JOSEPHSON ARRAYS USING MAGNETIC FORCE MICROSCOPY

BY

TYLER R. NAIBERT

DISSERTATION

Submitted in partial fulfillment of the requirements
for the degree of Doctor of Philosophy in Physics
in the Graduate College of the
University of Illinois at Urbana-Champaign, 2017

Urbana, Illinois

Doctoral Committee:

Professor Dale Van Harlingen, Chair
Professor Raffi Budakian, Director of Research
Professor Smitha Vishveshwara
Professor Bryce Gadway

Abstract

Vortices and vortex lattices play a major role in determining the transport properties of type-II superconductors [1–3], and enable a platform to investigate exotic superconducting physics [4,5]. The study of vortex matter has generally focused on novel states in 2D films and structures, and has recently moved to investigating systems with constrained dimensions and smaller vortex numbers [6–11]. Vortices are responsible, for example, for some electrical transport regimes in superconducting films, as well as the Berezinkskii-Kosterlitz-Thouless phase transition in superconducting films [12]. Unconventional forms of superconductivity, such as the spin triplet pairing predicted in Sr_2RuO_4, or in topological insulators paired to *s*-wave superconductors, contain two condensates that may support two vortex lattices, and may display Majorana modes, signatures of which may have been seen in other superconducting systems [13–17]. The vortex-vortex interactions, or inter- and intra-condensate couplings in multicondensate systems, are important parameters that characterize the behavior of the systems that display such phenomena [18–20]. In investigating these parameters, a technique that can both probe the energies in a system, as well as manipulate the vortices therein, has long been desired.

In this work, we report on progress in determining the energy scales of vortex systems, as well as limited control over the vortex motion. Using a technique based on magnetic force microscopy, we can directly measure the resonant motion of vortices present in a superconducting lattice. We use a scanning magnetic tip to trap a small number of vortices in a superconducting Josephson junction array near the tip. By observing the resonant motion of the configuration of vortices, a map of the location of energy degeneracies between different stable configurations is generated. From this data, we use a simulation to extract the relative strengths of the characteristic energy scales for the system, including the vortex-magnetic field interaction, the vortex-vortex interaction strength, and the chemical potential for the vortices. The simulations for small numbers of vortices fits the data well for multiple field profiles and lattice spacings. The ability to tune the vortex number and configurations by changing the magnetic field profile from the tip, as well as the lattice parameters of the superconducting surface, are key portions of this technique. We demonstrate that the relative strengths of the chemical potential and vortex-vortex interactions can be

tuned relative to the vortex-magnetic field energy by changing the lattice spacing of the array. We also show that by moving the tip farther from or closer to the surface, which changes the potential well from the tip, that the configurations of vortices can be modified. From the experiments, we show that this technique can be used to both extract the strengths of the relative energy scales in this system and other superconducting systems, as well as for manipulating the vortex configurations for quantum computation applications.

To Nicole and family.

Acknowledgments

In looking over theses from former students in my lab, as well as those of collaborators and friends, it appears that the acknowledgments section is either the most, or the least, read section of a dissertation. I suppose at some point, whether or not this section is ever read is of no consequence, as it serves mostly as a place for me to thank those who made my journey to this thesis possible. Science, and moreover, life in general, does not take place in a vacuum. It is not one person toiling away in a basement to understand the universe themselves, but rather a group of people working to expand humanity's knowledge. Following are some of the people who worked beside me, in person or in spirit.

First, I would like to thank my advisor, Raffi Budakian, for everything he has done for me. Before arriving at this particular thesis project, there were many experiments that didn't fully pan out, as well as setbacks with equipment and other issues. Raffi was always pushing forward, questioning if there were other ways to move the research forward, and confident that things would work out. His confidence got me though many a late night in the lab and elsewhere in life, and I will always be grateful for that. I would also like to thank the other professors collaborating on this project, Nadya Mason and Taylor Hughes. They were a constant source of inspiration for new measurements, calculations, samples, etc. Without them, this project would not have happened as it has.

Other students have been a constant source of inspiration and assistance, as well as comradery throughout my graduate career. First amongst them, I would like to thank Xu Wang, who was my mentor when I joined Raffi's group. He taught me a great deal about how the machines around lab worked, as well as the proper way to interface with some of the support staff (bug them every day until they get to your stuff). John Nichol was also a great help, both as a friend and mentor in the lab. I greatly enjoyed the time we spent in the cleanrooms working and talking for hours. Of those who have now moved on to other locales, I also would like to thank Serena Eley. As both a running buddy and fellow student, it was a pleasure. I did not think that I would wind up working on a project that you had so much influence over, but here we are!

For my current lab mates and collaborators, thank you to all. Hryhoriy Polshyn has always been available when I needed to transfer late at night, and was the inventor of the simulated annealing technique that is

used in this paper. The two of us have spent much time working together to make samples, improve the instruments, and generally around the lab, and I look back upon those times with fondness. Thank you as well to Bill Rose. I always enjoyed our talks ranging from gaming to nuclear magnetic resonance. Brian Wolin was one of the students that I mentored in the use of the MFM instrument, and he is a great co-worker. Always willing to come in to lab late or on the weekends to transfer helium or help set things up, I am glad of the time we spent together. The Mason group, specifically Malcolm Durkin and Rita Garrido Menacho, were instrumental in this research. Malcolm and Rita did quite a bit of fab for me, as well as assisting with transport measurements, and being around to chat with late at night.

Friends have also gotten me through a lot of grad school that may not have otherwise. Special thanks to Tony Hegg and Umi Yamamoto, former roommates and good friends. You guys were always there when I needed you for a helping hand with brewing beer, and just to hang out, with some physics discussions thrown in the mix (OK, a lot of physics discussions). Thanks as well to Katie and Phillip Ansell. You guys have always been there to chat, hang out, etc., and I'm thankful for all you've done for me. Brent Pomeroy, always a pleasure to hike with you to get out of lab for a bit.

A special thank you to Nicole Koeppen, my current fiancée, and, assuming the world doesn't explode, soon-to-be wife. You are a constant source of everything that I need to continue this work and make it through the day. Without you, I'm not sure I'd be where I am today. My parents, as well, were always encouraging to myself and my brothers, pushing us to be the best we can be, as well as lending an ear whenever I needed to vent about how grad school was going more slowly than I would have liked. My love to you all.

I would also like to thank the support staff here at MRL, who have always been willing to help and aid in the research that happens in the building. Also a shout-out to the facilities staff, who keep the place clean and the lights on. I enjoyed our conversations, and wish you all the best. The staff in the Physics department, especially the undergraduate office and graduate office, have always been kind and helpful while teaching and researching. Thank you also to CUMTD, without whom I would never have gotten to work on time. Finally, thanks to the DOE, who supported this research and made these investigations possible.

This work was supported by the DOE Basic Energy Sciences under DE-SC0012649, and was carried out in part in the Frederick Seitz Materials Research Laboratory Central Research Facilities, University of Illinois.

Table of Contents

List of Figures

List of Symbols

B	Magnetic field
c	Conversion factor between laser position and tip position
ξ	Superconducting coherence length
Ψ	GL theory pseudowavefunction
n_s	Superconducting electron density
ϕ	Superconducting phase
k_B	Boltzmann constant
$\hbar$	Reduced Planck's constant
λ	Superconducting penetration depth
H_c	Superconducting critical field
$f_{s,n}$	Free energy in the superconducting or normal state
κ	GL parameter
I_c	Superconductor critical current
e	Electron charge
E_J	Josephson energy
Φ_0	Flux quantum
J	Coupling strength
γ	Gauge-invariant phase
f	Frustration
a	Lattice constant
k	Cantilever spring constant
Q	Cantilever quality factor
u(t)	Cantilever deflection
ω	Cantilever frequency
L	Length of cantilever
T	Temperature
μ	Chemical Potential

List of Abbreviations

AFM	Atomic Force Microscopy
AM	Amplitude Modulated
BCS	Bardeen Cooper Schrieffer Theory
BKT	Berezenskii-Kosterlitz-Thouless
EFM	Electric Force Microscopy
FIB	Focused Ion Beam
FM	Frequency Modulated
FPGA	Field Programmable Gate Array
GL	Ginzburg-Landau Theory
IVC	Inner Vacuum Chamber
MFM	Magnetic Force Microscopy
PID	Proportional Integral Derivative
PCB	Printed Circuit Board
PLL	Phase-Locked Loop
RF	Radio Frequency
SC	Superconducting
SEM	Scanning Electron Microscope
SFM	Scanning Force Microscopy
SNS	Superconductor-Normal Metal-Superconductor
SPM	Scanned Probe Microscopy
STM	Scanning Tunneling Microscopy
TEC	Thermo-Electric Cooler
UHV	Ultra-High Vacuum

Chapter 1

Introduction

1.1 Motivation

Understanding of superconducting vortex matter is integral to gaining more knowledge about the superconducting state. Most of the studies of vortex matter has concentrated on 2D states in films and structures, such as polycrystalline structures, Mott insulators, granular systems, etc. More recently, systems with smaller numbers of vortices and constrained dimensions have begun to be investigated. The studies presented in this thesis focus on investigating a small number of superconducting vortices trapped under a magnetic tip, and using their motion on a Josephson array to investigate their configurations and energetics. Through imaging with a magnetic force microscope, patterns are generated which show rich diversity and lead to insight about the underlying states. Also, by modifying the magnetic field generated by the tip via its shape, basic control over the vortex arrangement is demonstrated. This study is motivated by the applicability this technique could have on other superconducting systems from both a technological and fundamental standpoint. Below we discuss the superconducting state, concentrating on the role of vortices on the properties of such a state.

1.2 Introduction to Superconductivity

Superconductivity is a state of matter characterized by both a complete loss of electrical resistance and the emergence of perfect diamagnetism below a critical temperature. The immense technical applications and fundamental scientific value has made the study of the superconducting state one of the largest topics in physics since its discovery. Unlike conducting metals, where the electrical resistivity decreases until a finite value as the temperature is lowered to near zero, superconductors display a sudden drop to a zero resistance state at a transition temperature T_c, as illustrated in Fig. 1.1.

The T_c is dependent on the material, impurities, and isotope. Some materials, such as Cu or Au, do not show a superconducting transition. Elemental superconductors, such as Al, Sn, and Nb, have transition temperatures that vary from less than one Kelvin (Ir, Ti, etc.) up to a high of 9 K for Nb [31,32]. Alloys

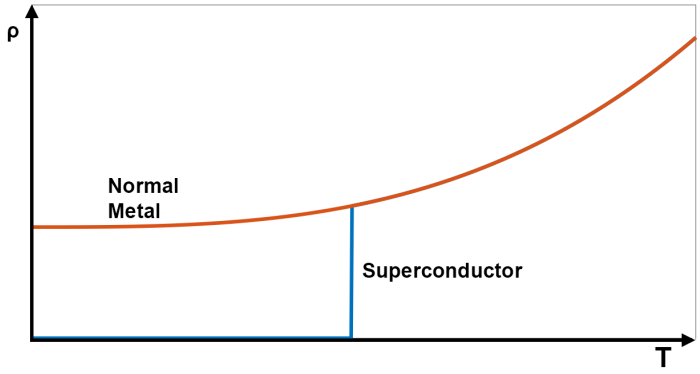

Figure 1.1: Illustration of difference between normal metals and superconductors.

can have even greater transition temperatures. Other materials that display superconductivity are of great interest, such as the cuprate superconductors, which display transition temperatures of over 100 K, and iron-based superconductors that were discovered in 2006 [33–35]. To understand such phenomena, a theory built using quantum mechanics is required. There are two major theories which are used to describe the phenomena of superconductivity: the Ginzburg-Landau (GL) theory and the Bardeen-Cooper-Schrieffer (BCS) theory. So-called conventional superconductors, such as Nb, are well described by the BCS theory, while other superconductors, such as the cuprates, seem to host many of the features predicted by BCS, but lack a full theoretical explanation of their superconducting state [33].

The basic element of the superconducting state is the Cooper pair [33,36], which is a pair of electrons bound to each other via interactions with the atomic lattice of the material. Essentially, at low temperatures, a small attractive force between electrons due to the atomic lattice is sufficient to form bound electron pairs, even in the presence of the larger, repulsive Coulomb force. These pairs have electrical charge $2e$, and a size given by the coherence length, ξ. Breaking these pairs into individual electrons requires an energy $2\Delta(T)$, where $\Delta(T)$ is known as the energy gap. The BCS theory was developed using these Cooper pairs as its building block and is a fully microscopic theory. Excellent agreement with experiment is found. For many macroscopic situations though, the microscopic BCS theory becomes intractable, and more reliance is placed upon GL theory [33]. GL theory is a macroscopic theory that was developed several years before BCS, and was shown by Gor'kov to be a limit of the full BCS theory [37].

Since Cooper pairs are bosons, they are not bound by the Pauli Exclusion Principle. The superconducting state occurs when the Cooper pairs condense into a many-body condensate wavefunction with some amplitude and phase that maintains phase coherence over macroscopic distances. In the Ginzburg-Landau

theory, superconducting regions have a psuedowavefunction

$$\Psi\left(\vec{r}\right) = \left|\Psi\left(\vec{r}\right)\right| e^{i\phi(\vec{r})} \tag{1.1}$$

with phase $\phi(\vec{r})$ and amplitude $|\Psi(\vec{r})|$. The squared magnitude of this order parameter gives the density of superconducting electrons as [25,33]

$$n_s = |\Psi|^2 \tag{1.2}$$

The total number of superconducting electrons, N, cannot be known precisely at the same time as its conjugate variable, the phase ϕ, due to the uncertainty relation $\Delta N \Delta\phi \geq 1$ [33].

When a superconductor is placed in contact with a normal metal, Cooper pairs from the superconductor can tunnel or diffuse into the normal metal, and single electrons from the metal diffuse into the superconductor. This phenomenon is known as the *proximity effect*, and occurs over distances set by a coherence length, ξ_N, of the normal material. If two superconductors are placed near to each other, but separated by a non-superconducting material, the proximity effect can allow the exchange of superconducting pairs between the two superconducting banks.

1.3 Superconductors in a Magnetic Field

Along with zero resistance, the second hallmark of the superconducting state is perfect diamagnetism, known as the Meissner effect. Superconductors in a field will attempt to expel all flux from within them, even if the field is applied prior to the system undergoing a superconducting transition. This also suggests that at some critical field, H_c, superconductivity will be destroyed. This critical field, which is dependent on the temperature, can be found by equating the magnetic field energy per unit volume with the condensation energy of the superconducting state

$$\frac{H_c^2(T)}{8\pi} = f_n(T) - f_s(T) \tag{1.3}$$

where $f_{n,s}(T)$ are the respective free energies per unit volume at zero field.

The Meissner effect, along with Maxwell's equations, imply that the magnetic field in a superconductor must be exponentially screened over a length λ, called the penetration depth (see Fig. 1.2). λ for different superconductors varies from very short (on the order of 1 nm) to much larger scale (order of microns for some materials) [32]. Taking a ratio of the penetration depth and the superconducting coherence length defines the GL parameter

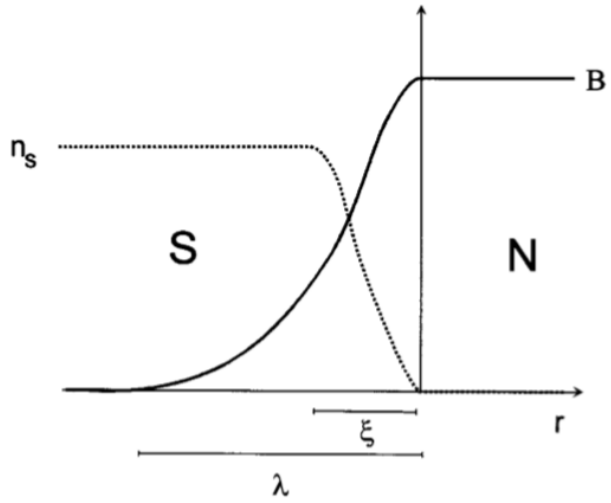

Figure 1.2: Illustration of the number of superconducting electrons, which is proportional to $|\Psi|^2$ (see Eq. 1.2) at the surface of a superconductor. When entering a superconductor, the magnetic field, B, is exponentially screened over a distance λ, known as the penetration depth. Figure from S. J. Bending [21].

$$\kappa = \frac{\lambda}{\xi} \tag{1.4}$$

This value is approximately independent of temperature, and is generally used to divide superconductors into two types. Many typical classical superconductors have a value of $\kappa < \frac{1}{\sqrt{2}}$. These are termed Type I superconductors, and will follow a discontinuous destruction of superconductivity at the critical field, H_c. For superconductors with $\kappa > \frac{1}{\sqrt{2}}$, there is a negative surface energy associated with the normal-superconductor interface, and so at a lower critical field H_{c1}, non-superconducting regions that contain one unit of flux each will begin to populate the superconductor. There flux tubes allow the superconductor to tolerate higher fields (see Fig. 1.3), as the flux is confined to non-superconducting regions. Around each of these flux tubes, there is a vortex of current flowing to constrain the field towards the normal flux tube. These vortices have size of order ξ, and will arrange themselves in a triangular pattern, called an Abrikosov lattice (Fig. 1.4), in an ideal superconductor [33]. Deviations from this triangular pattern have been seen, typically due to "pinning centers." At these pinning center locations, the energy to form a vortex is lowered due to effects such as magnetic impurities, crystalline defects, etc.

For a bulk superconductor, we can calculate the interaction force between two vortices if we make the approximation that $\kappa \gg 1$. In this approximation, and calculating the energy out to a cutoff length ξ, the line energy of the vortex is given by

$$E_1 \approx \left(\frac{\Phi_0}{4\pi\lambda}\right)^2 \ln\kappa \tag{1.5}$$

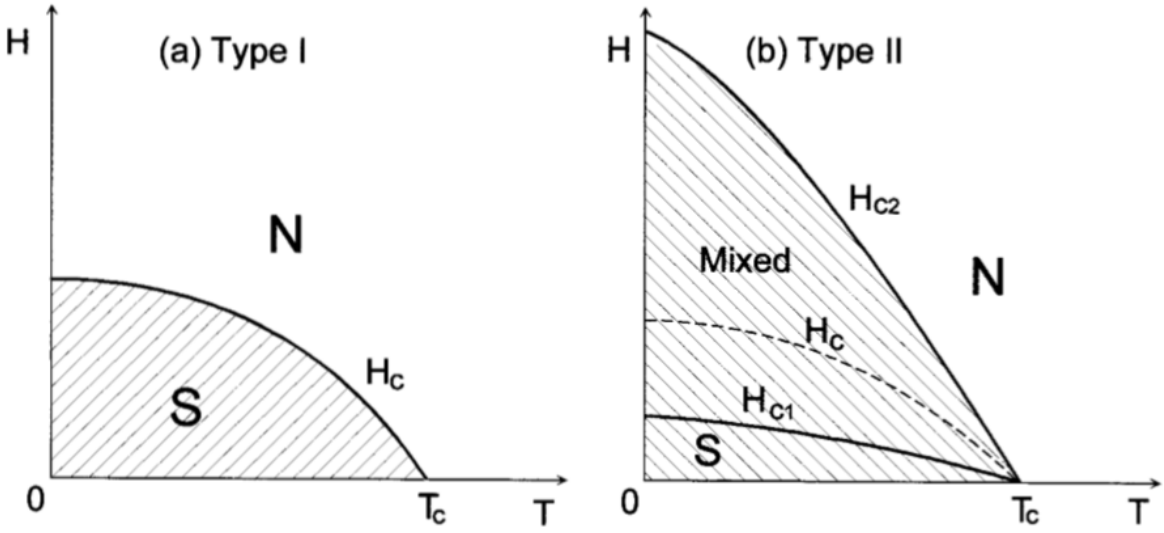

Figure 1.3: Phase diagram for (a) Type I and (b) Type II superconductors. In Type I superconductors, the superconducting phase is destroyed above H_c. In Type II, vortices begin populating the sample at H_{c1}, and continue building up until the loss of superconductivity at H_{c2}. Figure adapted from S. J. Bending [21]

where $\Phi_0 = h/2e$ is the flux quantum. The vortex-vortex interaction energy is given by

$$E_{12} = \frac{\Phi_0}{8\pi^2\lambda^2} K_0 \left(\frac{R_1 2}{\lambda} \right) \tag{1.6}$$

which falls off exponentially at large distances, and logarithmically at small distances. Since this interaction is repulsive for like vortices and attractive for oppositely-oriented vortices, the system will not be stable unless there is another pinning force present.

For films with a thickness less than the superconducting coherence length, ξ, the system is quasi-2D. These systems will often act as Type II superconductors due to the penetration depth being larger than the thickness, d, leading to an effective 2D penetration depth, $\Lambda = \lambda^2/d$, which is larger than in the bulk [38–40].In such films it can be expected that a vortex lattice will arise in a magnetic field. Additionally, thermally activated phase fluctuations of 2π may also produce a vortex or an anti-vortex (a vortex with oppositely directed currents), which can move when subjected to a current and dissipate energy.

In two dimensions, vortex-vortex interactions are different than in bulk superconductors. Pearl [41] derived the current distribution from these vortices falls off as $1/r$ at short distances, and at longer distances, as $1/r^2$. This is different from bulk superconductors, where vortex interactions fall off as $\ln(r/\lambda)$ and exponentially for short and long distances, respectively. These so-called Pearl vortices have been imaged in quasi-2D films [42]. As these 2D systems are cooled below a critical temperature T_{BKT}, the energy of bound pairs of vortices

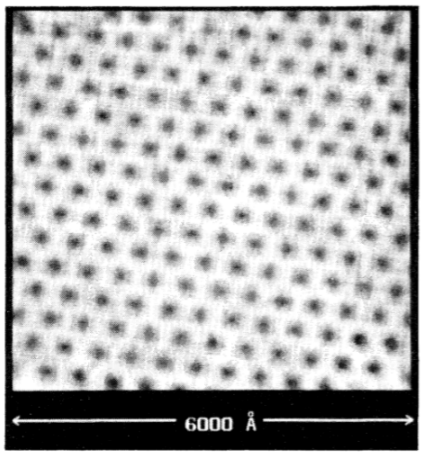

Figure 1.4: STM image of the triangular Abrikosov lattice. Figure from Hess et al [22]

becomes favorable for the system, and vortices and anti-vortices bind together. This is called the Berezenskii-Kosterlitz-Thouless (BKT) transition, and has been observed in granular thin film and Josephson Junction array samples [12,43–45]. For the data presented in this work, most images are taken at temperatures below T_{BKT}.

Novel states in 2D films and structures have been a primary focus of superconducting vortex matter research in the past. More recently, smaller number of vortices and samples with constrained dimensions have been explored [6–11]. In these mesoscopic samples, new effects have been observed, such as symmetry-induced generation of anti-vortices [6], Weber Blockades, which is the magnetic analogue of the Coulomb blockade [8], and re-entrant superconductivity in a magnetic field [46]. Additionally, the effects of collective motion of a small number of vortices have been seen in other experiments [9]. These experiments show that there are effects that cannot be investigated using data averaged over a large number of vortices, as given by techniques like transport data on large arrays, or by imaging individual vortices themselves. New samples and techniques are therefore required to investigate these mesoscopic phenomena.

1.4 The Josephson Effect

In 1962, it was predicted by Brian Josephson that there should exist a supercurrent between two superconductors separated by a thin (length $< \xi$) insulating barrier even at zero voltage difference [33,47]. This current

$$I_s = I_c \sin(\Delta\phi) \tag{1.7}$$

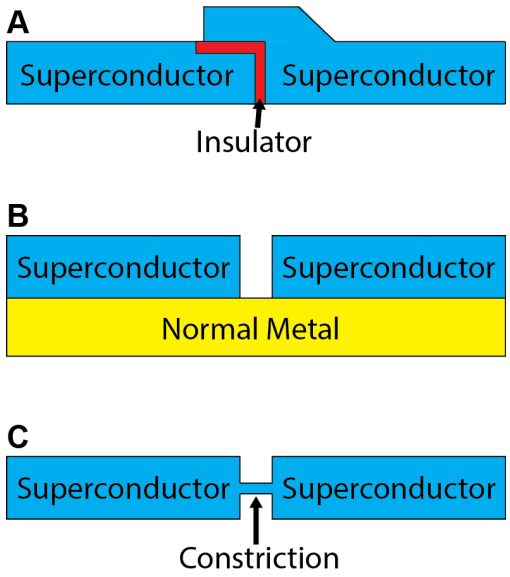

Figure 1.5: Types of Josephson junctions. (**A**) Junction made with an insulating barrier (SIS junction). (**B**) Junction formed by with a normal metal (SNS junction). (**C**) Junction formed by a narrow constriction (ScS junction).

is dependent only on the phase difference of the Ginzburg-Landau wavefunction of the two superconductors and the critical current, I_c, which is the maximum supercurrent the junction can support. If a voltage is applied to the system, the phase difference will evolve in time according to

$$\frac{d\left(\Delta\phi\right)}{dt} = \frac{2eV}{\hbar} \tag{1.8}$$

where V is the voltage across the junction. Therefore, the current will oscillate with amplitude I_c and frequency $\nu = 2eV/\hbar$. These two effects are known as the DC and AC Josephson effects. Additionally, the free energy stored in a Josephson junction is given by

$$F = -E_J \cos\left(\Delta\phi\right) \tag{1.9}$$

where $E_J = \hbar I_c/2e$.

As originally proposed, the Josephson effect was based on quantum tunneling of electrons through an insulating barrier, but the effect is more general, occurring when two superconducting banks are separated by a "weak link." This weak link can be formed from an insulator, normal metal, or a narrow superconducting constriction (see Fig. 1.5). Josephson junctions formed with normal metal are referred to as SNS (Superconductor-Normal Metal-Superconductor) junctions. In SNS junctions, the proximity effect makes the normal metal weakly superconducting, leading to the Josephson relation.

1.4.1 Josephson Junction Arrays

Many superconducting islands closely spaced on a metallic film form an array of SNS Josephson junctions. In these Josephson junction arrays (JJAs), vortices that are generated either thermally or through magnetic fields play an important role in the properties of the array. Other thin films and quasi-2D superconductors also have properties that are determined by vortices in the system, making Josephson junction arrays an excellent model for these systems. JJAs are typically lithographically defined, leading to the ability to change the system parameters in controllable ways. This makes JJAs ideal model systems for understanding quasi-2D superconductors. We now explore the energy landscape of JJAs to understand more about the vortex states present in such a system.

Generally, the energy of a Josephson junction array can be written as [48]

$$H = \frac{1}{2}\sum_{\langle i,j\rangle} q_i U_{ij} q_j - E_J \sum_{\langle i,j\rangle} \cos\left(\phi_i - \phi_j - \frac{2\pi}{\Phi_0} A_{ij}\right) \tag{1.10}$$

where the first term is the charging energy between islands, and the second is the Josephson coupling. In this equation, $E_J = \hbar I_c/2e$ is the Josephson energy, Φ_o is the flux quantum, and $\langle i,j\rangle$ denotes a sum over pairs of islands. U_{ij} is obtained through the capacitance matrix, which scales with the junction charging energy, $E_c = e^2/2C$. The Josephson energy will tend to establish phase coherence across the array, while the charging energy will tend to decrease charge fluctuations. Competition between the two energy scales will determine if the system becomes an insulator (E_c dominant) or superconductor (E_J dominant) at low temperatures. For SNS arrays such as ours, the capacitive contribution to the energy is typically small, and will be discounted in further sections [25,49]. Various models of Josephson arrays, such as the rotor model, Coulomb gas model, RCSJ model, etc., are more applicable in certain E_J/E_c ranges. These models will be discussed in detail in Chap. 4.

Resistance vs temperature of JJAs

For granular superconducting films near the critical temperature, a slight broadening of the resistance vs. temperature curves is seen (Fig. 1.6). This broadening was thought to occur due to either a spread in the critical temperatures of individual grains, or a BKT transition. Proximity-coupled SNS arrays give insight into this phenomenon, because if the arrays adhere to predictions for BKT, then it becomes more likely that vortex dynamics play a role in this broadening.

Studies such as Resnick et al [12] showed evidence of a BKT transition in a Pb island with Sn overlayer with a square lattice. These results showed a two-step transition to superconductivity where the second

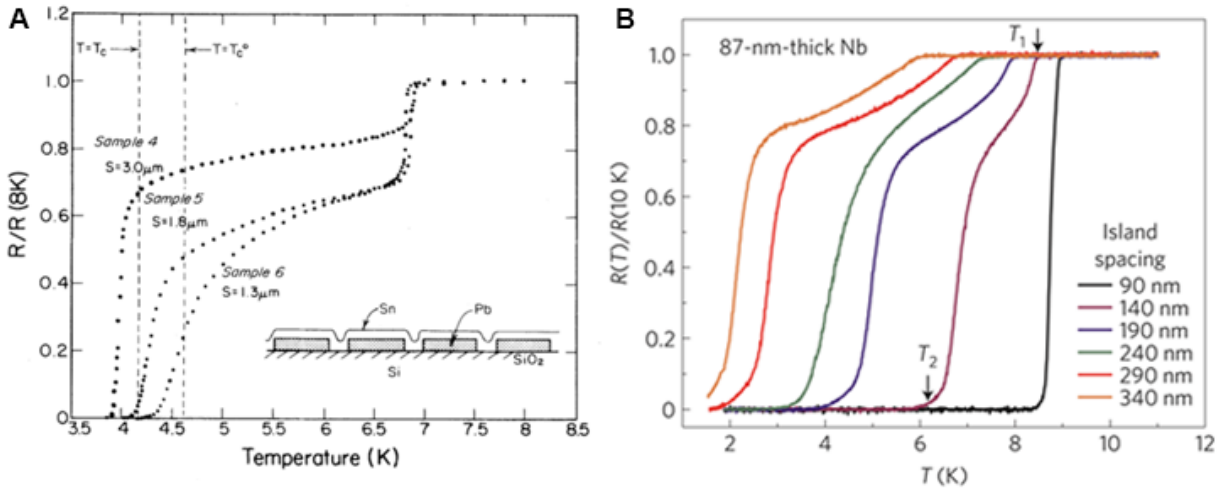

Figure 1.6: Figure showing the two-step transition to superconductivity. (**A**) Image extracted from Resnick et al[12]. The island spacing is denoted by S. T_c is marked for the arrays with spacing of 1.3 μm. (**B**) Image extracted from Eley et al[23] for a triangular array of islands of diameter 260 nm and various spacing. Black arrows and labels are for the islands with spacing $a = 140$ nm.

transition temperature was suppressed by greater separation of the Pb islands (see Fig. 1.6A). This behavior was explained by a model with several regions where elements became superconducting at different times, and showed results that were consistent with a BKT transition. The superconducting island size and spacing used in the study by Resnick et al.[12] were large (13 μm across with 1-3 μm spacing) compared to the samples used in this work. For arrays such as those considered in this work, where the island size is smaller and comparable to ξ, the theory needed to be modified to agree with experiment. In these systems, a superconducting path can traverse the sample at a temperature that is dependent on the lattice spacing of the array. A phenomenological model that works at these length scales was used to demonstrate the possibility of $T = 0$ metallic states in SNS arrays[23]. This model uses phase differences and coupling between superconducting grains on the same island (with coupling strength J) and grains of different islands (with coupling strength $J' < J$) to explain the different regions in the resistance vs. temperature plot. Fig. 1.7 shows this two-step transition as divided into five regions. These regions are described as follows:

- **Region I**: Above a temperature T_1, the island has individual grains with incoherent superconducting phases, resulting in a non-superconducting state.

- **Region II**: At T_1, phase coherence begins to be established among grains on the same island, resulting in a decrease in resistance due to Cooper pairs diffusing into the normal metal. As the sample is cooled below T_1, the phase coherence on individual islands strengthens (J increases), leading to a gradual

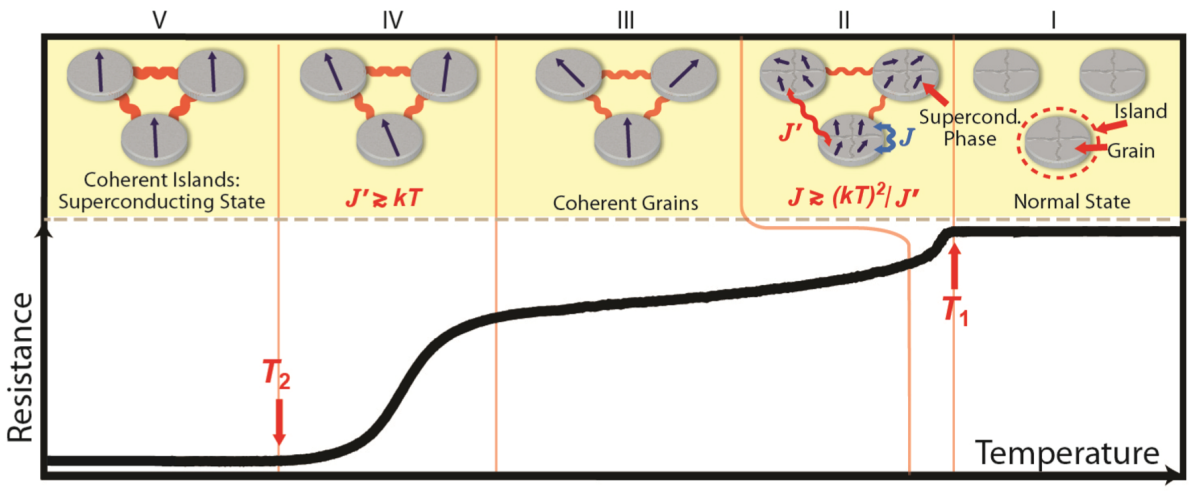

Figure 1.7: Illustration of the model of two-step superconductivity. Gray disks represent the superconducting islands, with various grains denoted by the wavy lines. Grains on a single island couple with strength J, while grains on separated islands couple with strength J'. Arrows on the grains/islands represent the phase of that grain/island. See text for details. Image extracted from Eley [24].

drop in the resistance.

- **Region III**: In this region, individual islands are fully superconducting, leading to a saturation in J. J' increases, and ξ_N, the normal metal coherence length, is increasing with decreasing temperature.
- **Region IV**: ξ_N increases to the point where it is comparable to the inter-island spacing. Phase coherence emerges between the islands, and at T_2, the array undergoes a BKT transition and enters a fully superconducting state.
- **Region V**: Below T_2, the system is fully superconducting.

1.4.2 Magnetic field effects on JJAs

For a Josephson junction array in a magnetic field, the Josephson relation between two superconductors i and j is modified to be

$$I_{ij} = I_c \sin\left(\phi_j - \phi_i - \frac{2e}{\hbar}\int_i^j \vec{A}\cdot d\vec{r}\right) \tag{1.11}$$

where ϕ_i is the phase of the i^{th} island and $\vec{A}$ is the vector potential. The phase difference between the islands is therefore

$$\Delta\phi_{ij} = \phi_j - \phi_i = \sin\left(\frac{I_s}{I_c}\right) + \frac{2\pi}{\hbar}\int_i^j \vec{A}\cdot\vec{r} \tag{1.12}$$

Summing around any closed path of junctions, the phase must change by some multiple of 2π. Since the path integral of the vector potential leads to the total flux enclosed, Φ, we assume summation around a single unit cell of junctions, called a plaquette, and find

$$\sum_{junctions} \sin^{-1}\left(\frac{I_s}{I_c}\right) = 2\pi\left(n - \frac{\Phi}{\Phi_0}\right) \tag{1.13}$$

where $\Phi_0 = \frac{\hbar}{2e}$ is the flux quantum and n is an integer. Each plaquette in the system must satisfy Eq. 1.13 with its own n and Φ. Replacing $\sin^{-1}\left(\frac{I_s}{I_c}\right) = \gamma_{ij}$, the gauge invariant phase difference, and neglecting effects from kinetic inductance[50], we find

$$\sum_{junctions} \gamma_{ij} = 2\pi\left(n - \frac{\Phi}{\Phi_0}\right) \tag{1.14}$$

Generalizing this to any contour, and letting $f_i = \frac{\Phi_i}{\Phi_0}$ be the *frustration* of plaquette i, we find

$$\sum_{contour} \gamma_i = 2\pi \sum_{\substack{enclosed \\ plaquettes}} \left(\hat{n}_j - \hat{f}_j\right) \tag{1.15}$$

Assuming a lack of screening effects, which is generally a good approximation for SNS arrays[50], a magnetic field applied perpendicularly to the array will be constant everywhere. This is referred to as a uniformly frustrated array, and the energy can be written as a sum over the single-junction energies as

$$E = E_J \sum_{array} (1 - \cos\gamma_i) \tag{1.16}$$

In the zero field case ($\Phi = 0$ for all plaquettes), and at $T = 0$, the energy of the array is minimized by having the phases of all superconducting islands be equal with $n = 0$.

The next state is one in which a lone vortex occupies the array. The vortex will be located at the center of one plaquette, where the superfluid density is lowest. In this case, the phase around any contour containing the vortex must vary by 2π. With arrays with center-to-center island spacing a, the values of γ_i must fall off as a/R, where R is the effective radius of the path. For small γ_i and using Eq. 1.16, the energy per junction is found to be approximately $E_J a^2/2R^2$. Combining this with the approximately $2\pi R/a$ junctions and approximating the sum as an integral, we find the total energy to be

$$E_{\substack{single\\vortex}} = \pi E_J \ln\left(\frac{R}{a}\right) \tag{1.17}$$

where R is the system size.

To determine vortex-vortex interaction energy scaling, consider a vortex-antivortex pair separated by a distance R_{12}. Following a similar argument to above, and noting that contours that contain both vortices will have the phase wrap by 0, the sum will be cut off at the separation of the two vortices, leading to an energy of

$$E_{12} = 2\pi E_J \ln\left(\frac{R_{12}}{a}\right) \tag{1.18}$$

This energy is increasing with increasing separation, so that vortices of opposite circulation will undergo an attractive force of approximately $2\pi E_J/R_{12}$.

JJAs in uniform magnetic fields

If a magnetic field is applied to an array, the lowest energy state will be one in which vortices enter such that there is no macroscopic circulation around the perimeter. Recalling the frustration $f = \frac{\Phi}{\Phi_0} = \frac{BA}{\Phi_0}$, where B is the magnetic field and A is the plaquette area ($A = \sqrt{3}a^2/4$ in the case of equilateral triangular arrays), the energy of the array will be minimized when the proportion of plaquettes that contain a vortex is equal to the frustration. The energy of each individual plaquette will not be minimized in this case, leading to the system being frustrated for non-integer frustration values.

As the applied field is varied, the vortex configuration present in the array will also change. As vortex motion is a source of dissipation, this is often seen in transport measurements as a resistance in the array as the field is varied. These magnetoresistance dips occur at certain rational frustration values (See Fig. 1.8 for an example) where vortices in the array are pinned by the presence of the other vortices. To have one vortex jump would create a configuration with higher energy, and the amount of energy required to move all the vortices in the array simultaneously is higher than can be supplied by thermal energy, so the vortices are pinned by the presence of the other vortices in the lattice. For triangular arrays of Josephson junctions, the strongest dips are typically seen at $f = \frac{1}{4}, \frac{1}{3}, \frac{3}{8}, \frac{1}{2}, \frac{5}{8}, \frac{2}{3}, \frac{3}{4}$, and 1 [24,43].These types of magnetoresistance oscillations have been measured in superconducting films with artificial pinning centers, which will be discussed below, as well as Josephson junction arrays like the ones discussed here [24,43,51–53].

The energy barrier for vortex motion between two adjacent plaquettes is also of interest. Using a single vortex in an array, and adjusting the position of the vortex between the center of a plaquette and the center

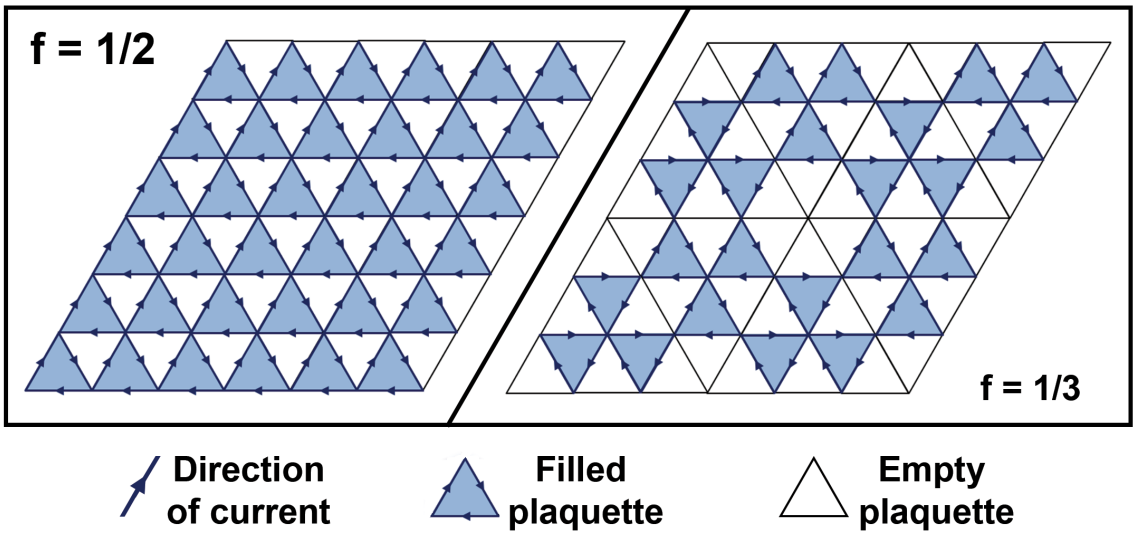

Figure 1.8: Examples of the vortex configuration for two rational frustrations, showing the current in each branch. Superconducting islands are located at the vertices of each triangle. The superconducting phases of these islands must wrap by 2π around an occupied plaquette.

of the link between two adjacent plaquettes, Lobb et al.[54] was able to numerically calculate this barrier height. For a triangular array of junctions, the barrier height was calculated to be $\approx 0.043E_J$. The value for a square array is found to be $0.199E_J$, which can be compared to experimental values of 0.3-0.5E_J[55]. Possible sources for this discrepancy are mutual inductance effects[50] or the variations in parameters that are present in real arrays[33]. An illustration of the "egg crate" potential that these barriers produce is shown in Fig. 1.9.

1.4.3 Other systems used to study vortex matter

Other artificially created systems are also used to study vortex matter in superconductors, as well as other effects such as pinning. We now discuss some of these other systems, which may display similar effects to those in Josephson junction arrays.

Superconducting wire networks

Superconducting wire networks (Fig. 1.10) show similar behavior to that of JJAs[56]. For wires that have a width of the order of the coherence length, ξ, and a length, s, longer than the width (and larger than ξ), the wires will act as weak links between the nodes of the array[26,56,57]. These wire arrays may be modeled as having a phase at each of the nodes, just like the islands have a definite phase in many Josephson arrays.

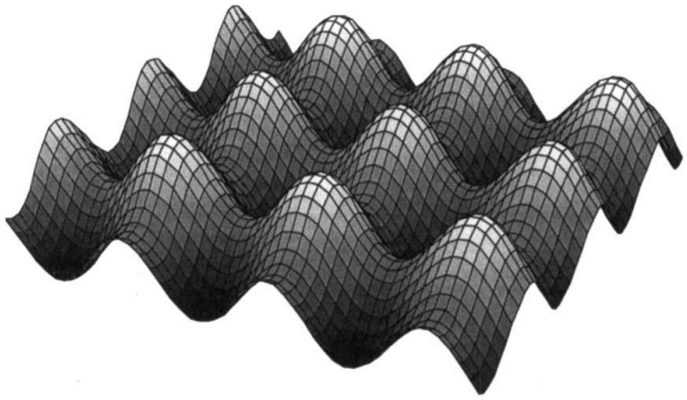

Figure 1.9: Illustration of the pinning potential for a square Josephson junction array. Figure from Newrock et al. [25]

For sufficiently small phase differences between the nodes, the energy in the system is linear in the current, and the wire network looks like a Josephson junction array with small phase differences [57].

These wire networks have also been used to study vortex phenomena in two-dimensional systems [26], as well as percolation networks and other network structures [58,59]. As discussed earlier, they show similar vortex configurations and magnetoresistance dips for rational frustrations [26,56,60], though the vortex mobility is lower than that of a Josephson array [57]. A linear approximation of the Josephson junction array can be created as a model for the data collected in this thesis, which compares well to a superconducting wire network. Details for this model will be discussed in Chap. 4.

Antidot arrays

Thin films with a lattice of holes or weaker superconducting regions, called antidots (Fig. 1.11), are frequently used to study pinning of vortices in 2D superconductors. In these systems, vortices will preferentially lie at the antidots, where the superconducting condensate is weak or, in the case of holes, non-existant. These antidot systems also show magnetoresistance oscillations like those seen in JJAs [27,61]. For larger antidots, multiquanta vortices may be trapped at each pinning center [62–64]. Magnetic fields that are strong enough to generate multiple vortices in some plaquettes can result in interstitial vortices that sit between antidots [27,64,65]. Guided motion of the vortices along the symmetry directions of the pinning array has been observed for these arrays as well [61].

Magnetic dot arrays

Arrays of magnetic dots deposited onto superconducting films also act as pinning centers by weakening the superconducting condensate beneath them. The pinning forces can be stronger than those from nonmagnetic

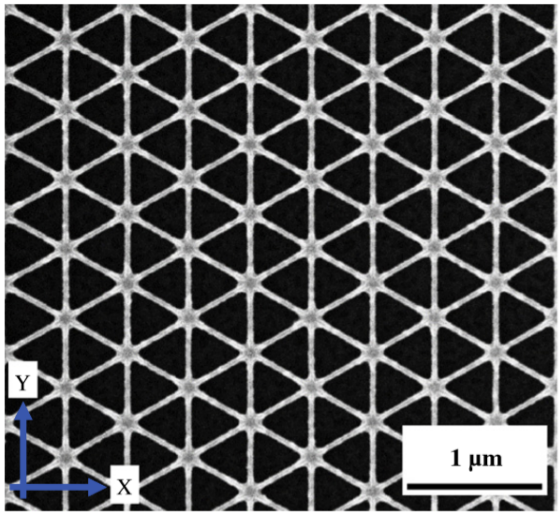

Figure 1.10: An SEM image of a triangular superconducting wire network by Zhang et al [26]. The wires are made from Nb, with the lattice constant for this network is 525 nm and a wire width of 40 nm.

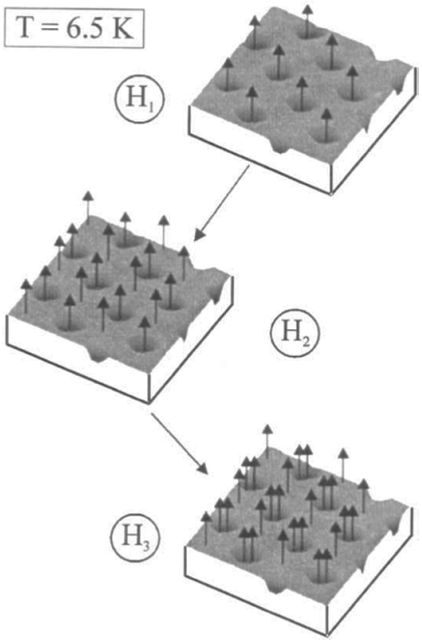

Figure 1.11: Illustration of the vortex locations in an antidot lattice at differing matching fields at temperatures near T_c. Vortices can be seen both at the antidots, and at interstitial sites. H_i corresponds to a flux of i quanta per unit cell. Figure from Moshchalkov *et al* [27].

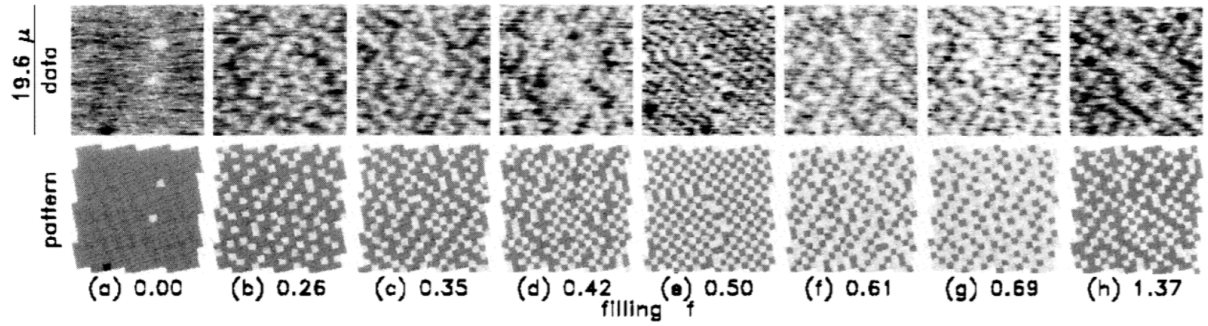

Figure 1.12: Scanning Hall probe images of a superconducting wire network at different frustration values. The image size is 19.6 μm, with a grid of Nb wires with 0.95×0.95 μm^2 holes. The upper image is the experimental data, while the lower image is the corresponding vortex pattern. On the patterns, white boxes contain vortices, while gray boxes are empty. Figure from Hallen *et al* [28].

pinning centers such as those discussed above, due to a combination of the proximity effect and magnetic fields [66]. The magnetic dot arrays are formed either with the magnetic dots underneath the superconductor or deposited on top. These magnetic dot arrays also show a field matching effect at integer frustrations in the resistance [66], critical current [67], and magnetization [68]. As with antidots, sufficiently high fields will cause vortices to be bound at interstitial sites [66]. Bound vortex-antivortex pairs have also been seen at the ends of elongated dots magnetized in-plane [69]. For triangular magnetic dots, ratchet effects in the motion of vortices have been observed [70]. These ratchet effects constrain the vortices to primarily move in one direction, which could be useful in controlling vortex motion for quantum computation and other purposes.

1.4.4 Previous imaging experiments on vortices and vortex matter

A number of techniques exist to image vortices in materials and artificial structures. Many of these techniques image single vortices at high spatial or magnetic resolution to determine information about the properties of the vortex states. Techniques that have been used previously include scanning SQUID microscopy [1,60], Hall probes [28,71], scanning tunneling microscopy (STM) [22], NV center magnetometry [72,73], cantilever-based techniques [74–78], and others [79]. In superconducting wire networks and Josephson junction array systems more specifically, some of these techniques have been used to investigate the vortices in the array and confirm vortex configurations such as the ones shown in Fig. 1.8 [28,60]. Other work using STM has recently shown the existence of vortex cores in Josephson vortices, present inside a single Josephson junction [80]. Arrays of π-rings have also been fabricated by Kirtley *et al.*, and show antiferromagnetic ordering when cooled in zero field [81].

Some studies have also been done on vortex dynamics in JJAs and other systems. Using low-temperature SEM, Lachenmann et al. were able to investigate the effects of a current bias on dynamics of Josephson arrays

with differing parameters[82]. In addition, scanning AC-susceptibility microscopy has also given insight into the motion of vortices in thin film systems. That technique works by using a small oscillating magnetic field from a coil, and reading the in-phase and out-of-phase components of the response of a Hall probe observing the vortices on the surface[65,83,84].

Manipulation of individual vortices

Manipulation of individual vortices has been used in the past to study vortex pinning and to control the vortex configuration in superconducting devices[85]. Moving individual vortices has been accomplished by several different techniques. Scanning SQUID is one technique where vortices can be moved. Plourde and Van Harlingen[86] observed that scanning the tip of a scanning SQUID microscope over the surface of MoGe films will shift the vortex positions. Gardner and Moler[85] used a similar technique, applying a local magnetic field supplied by a field coil in a SQUID microscope to move vortices in a YBCO crystal.

Magnetic force microscopy (MFM) has also been used to move vortices on the surface of superconductors[78]. By moving the magnetic tip of an MFM close to the surface, vortices can be attracted to the tip, and they can be dragged out of one potential well into neighboring wells. This has been used to study the pinning of vortices in thin films of Nb and YBCO[78,87,88]. "Vortex wiggling", where a transverse alternating force is added to the cantilever motion, has been shown to enhance vortex dragging in larger crystals[75]. The capability to move and image vortices may lead to quantum computing applications[89–91].

1.5 Introduction to Thesis Problem

In this thesis, we report on studies of superconducting Nb islands in a triangular arrangement set on a thin normal metal (Au) film. At temperatures slightly below the superconducting transition (zero resistance across the array), the array is imaged via MFM. Due to the role vortices play in a system such as this, we investigate the vortex states using sweeps of the external field and tip scanning height. In Chapter 2, we discuss the basics of MFM, and the particulars of our imaging setup. We also discuss the fabrication of the SNS arrays. In Chapter 3, we discuss the mechanism behind the formation of patterns seen in the images taken of the arrays. Chapter 4 will present the simulations of the data used to analyze the images formed by the vortex states. Chapter 5 presents initial data on imaging in the presence of a DC current bias.

Chapter 2

Experimental Techniques

2.1 Scanning Force Microscopy

Scanning force microscopy (SFM), an overarching term for technologies such as atomic force microscopy (AFM), magnetic force microscopy (MFM), and electric force microscopy (EFM), is a subset of scanning probe microscopy. The first scanning probe microscope, the scanning tunneling microscope (STM) was invented in 1982, by Binnig and Rohrer [92]. STM works by bringing an atomically sharp tip close enough to a surface that electrons can tunnel between the two. This tunneling current reflects the electronic structure of the surface of the material, and scanning the tip across the surface gives a map of this electronic structure. The tunneling current is also affected by the tip-sample separation, giving a highly accurate displacement probe. The first AFM was developed a few years later by Binnig, Quate, and Gerber in 1986 [29], which used a cantilever scanning a surface, the deflections of which were captured by an STM tip (see Fig. 2.1). This setup enabled measuring the forces between the atoms in the cantilever and those of the surface. In most present-day systems, the cantilever deflection is measured by a laser, which has advantages in the negligible force imparted to the cantilever, as well as being insensitive to many contaminants on the cantilever itself [93].

In brief, a SFM is operated by bringing a sharp tip into the range of whatever forces are to be analyzed. The tip, attached to a cantilever, is then deflected by the force, with the deflection being read out by some sensor. A spatial map of the forces is created by raster scanning the tip over the surface [30]. In MFM, first demonstrated by Martin and Wickramasinghe [94] in 1987, detection of magnetostatic forces with high spatial resolution is accomplished using a magnet attached to the tip [95].

2.1.1 Cantilevers

The mechanical properties of the cantilever play a primary role in determining the performance of the microscope. Cantilevers are usually found in two types: rectangular or triangular. Here, we present the mechanics of a rectangular cantilever probe, such as the one used in this work. Triangular cantilevers have more complex mechanics, and are not described in this work. Readers are referred elsewhere for more

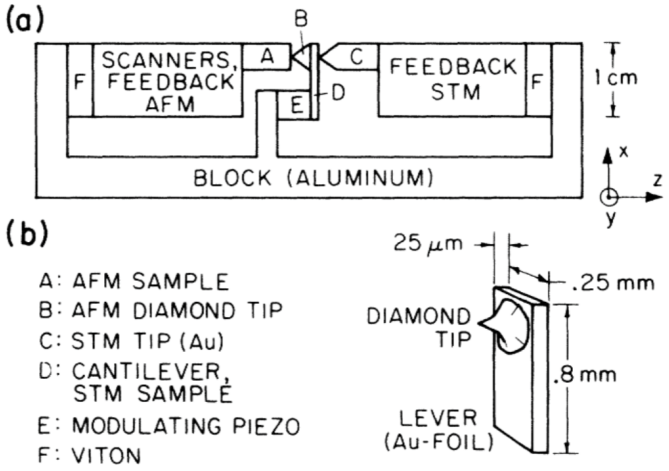

Figure 2.1: Design of the first AFM by Binnig *et al.*[29]

information on cantilevers of this type[96].

We consider a rectangular cantilever with length L, width w, and thickness d (See Fig. 2.2). The cantilever and base chip will be made of a single material with Young's modulus E. Then, the spring constant of the lever is given by[93,97]

$$k = \frac{Ewd^3}{4L^3} \tag{2.1}$$

The cantilever's motion is described by damped harmonic oscillator equation

$$m_{eff}\frac{d^2u}{dt^2} + \gamma\frac{du}{dt} + ku = F(t) \tag{2.2}$$

where $\gamma = \omega_0/Q$ (Q being the quality factor of the cantilever), and the resonant frequency of the cantilever, ω_0, is given by[93,97]

$$\omega_0^2 = \frac{k}{m_{eff}} \tag{2.3}$$

where $m_{eff} = 0.2427m_{cantilever} + m_{magnet}$ is the effective mass of the cantilever and magnet.

Solving this equation of motion for a sinusoidal driving force $F(t) = F_0\sin(\omega t)$ leads to

$$u(t) = u_0\sin(\omega t + \phi) \tag{2.4}$$

where u_0, the amplitude of oscillation, is given by

$$u_0(\omega) = \frac{F_0}{m_{eff}\sqrt{(\omega_0^2 - \omega^2)^2 + \left(\frac{\omega\omega_0}{Q}\right)^2}} \tag{2.5}$$

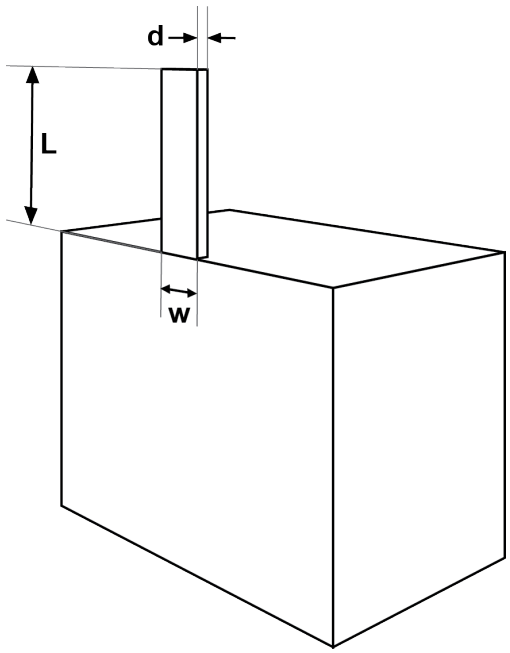

Figure 2.2: A diagram of a rectangular cantilever.

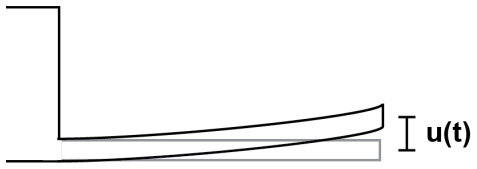

Figure 2.3: Cantilever deflection as seen from the side.

The maximum value of u occurs at a frequency $\omega_{max} = \omega_0\sqrt{1-(4Q^2)^{-1}}$. For the work presented here, $Q \approx 10^4$, so that $\omega_{max} \approx \omega_0$ [97]. At resonance, the maximum amplitude is then

$$u_{max} = \frac{F_0 Q}{m_{eff}\omega^2} \tag{2.6}$$

For our system, cantilever amplitude detection is done at a pad $\approx 80\%$ of the way to the end of the cantilever, as shown in Fig. 2.4. This pad has a greater width than the cantilever itself, in order to aid in reflection of the laser from the cantilever, as well as aiding with maintaining alignment of the laser with the cantilever while cooling to cryogenic temperatures, which can be problematic due to thermal contraction in the system. A conversion between the point the laser observes and the actual tip displacement is therefore necessary to determine the amplitude of oscillation of the cantilever tip.

We begin by describing the shape of an oscillating rectangular cantilever. Multiple eigenmodes are

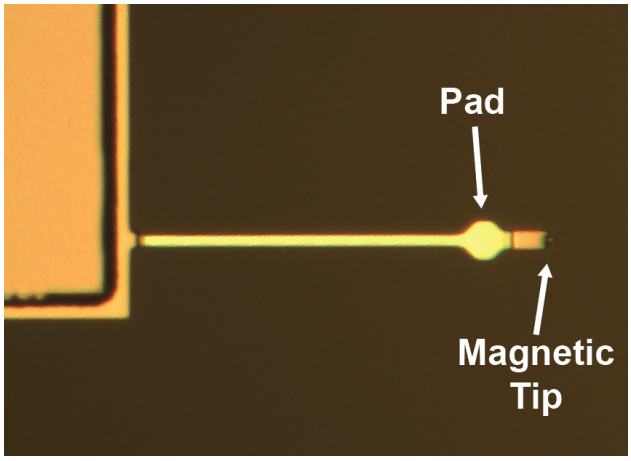

Figure 2.4: A cantilever similar to the ones used in the experiment, showing the optical pad and magnetic tip at end.

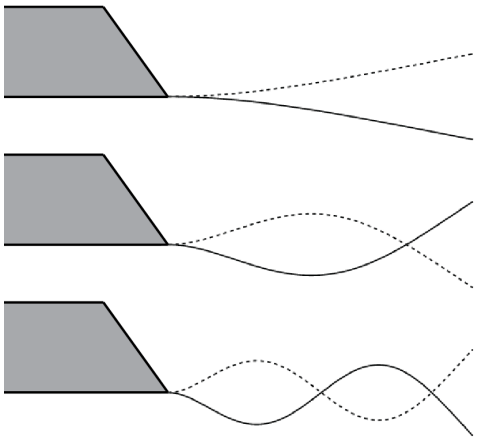

Figure 2.5: The first three eigenmodes of a vibrating lever. Amplitudes have been scaled to be equal. Displacement calculated using Eq. 2.7 with $\kappa L = 1.875$, 4.694, and 7.855.

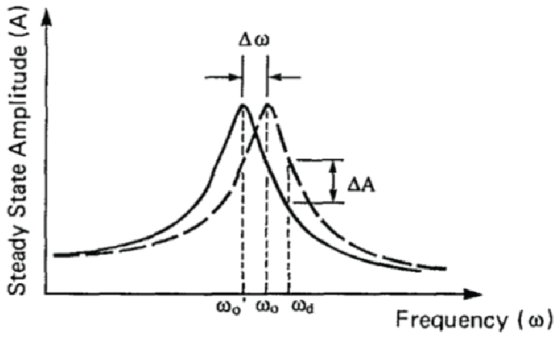

Figure 2.6: AM detection setup. The system is driven at a frequency slightly off resonance. When the frequency of the system changes in response to a stimulus, the amplitude of the oscillation changes. Figure extracted from Albrecht *et al.*[30]

present for such a lever, the first few of which can be seen in Fig. 2.5. The shape of these eigenmodes is given by[93,98,99] as

$$c(x) = A_0 \left(\cos(\kappa x) - \cosh(\kappa x) + \left(\frac{\sin(\kappa L) - \sinh(\kappa L)}{\cos(\kappa L) + \cosh(\kappa L)} \right) (\sin(\kappa x) - \sinh(\kappa x)) \right) \tag{2.7}$$

where x is the distance along the cantilever from the base, and A_0 is determined by the amplitude of vibration. κ is a parameter that depends on the mode. For the fundamental mode, which is used in this work, $\kappa L \approx 1.875$. To find the relative displacement in the fundamental mode, we set $A_0 = {}^1/_2$, so that $c(L) = 1$. Using this formula, and knowing how far the pad is from the base of the cantilever, allows calculation of the tip displacement via $u_{tip} = u_{pad}/c(x)$[93,99].

2.1.2 Force Detection Schemes

Two main force detection schemes are used in experiments, and have advantages for different applications and environments. The first, amplitude modulation (AM), works by observing the amplitude of the cantilever while oscillating at a fixed frequency. The frequency is picked to be slightly ($\approx 5\%$) off the resonant frequency of the cantilever (Fig. 2.6). As forces from the surface interact with the cantilever, the resonance peak shifts in frequency space, changing the oscillation amplitude of the cantilever, and allowing demodulation of the force signal[30,100]. The AM technique is often used in commercial AFMs due to its ability to measure very small height variations of the sample in an ambient environment[100].

When damping is small, AM becomes difficult due to the resonant peak becoming very sharp (high Q). This sharpness constricts the usable bandwidth of the cantilever to small values, often less than 1

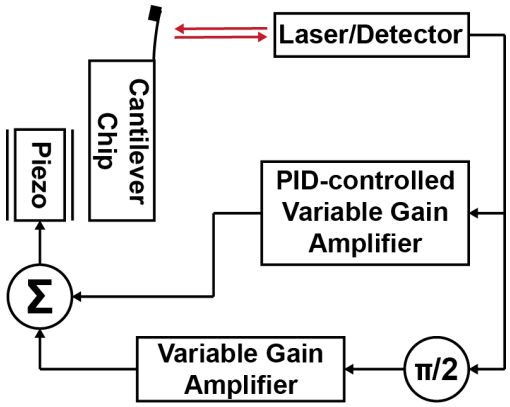

Figure 2.7: Schematic of the self-oscillation setup. The PID controlled variable gain amplifier controls the oscillation amplitude through the in-phase component of the driving signal.

Hz [30]. Decreased damping can be achieved by placing the cantilever in vacuum, as air damping becomes less important at pressures below approximately 10^{-3} Torr. For our setup, where pressures are typically $< 10^{-6}$ Torr, we utilize the other force detection scheme, which performs well with lower cantilever damping.

Frequency Modulated (FM) detection is used to take advantage of the increased Q in vacuum, as well as maximize the usable bandwidth [101]. The cantilever is maintained at its own instantaneous natural frequency, which is termed *self-oscillation*. Self-oscillation is achieved by way of sending the cantilever's own displacement signal back into a piezoelectric plate underneath the cantilever, with appropriate phase shifts applied [30,101]. The AC-coupled signal is sent into an amplitude control box, which produces two drive signals:

- In-phase: A variable gain amplifier is used to gain the displacement signal, controlled by another PID algorithm on the FPGA. This PID controls the cantilever amplitude at a set level specified by the user.
- Out-of-phase: A $\pi/2$ phase shift is applied to the cantilever signal and amplified by a variable gain amplifier.

The two drive signals are summed and sent to the piezoelectric plate underneath the cantilever, exciting the lever at its own resonant frequency (see Fig. 2.7). The quality factor of the cantilever, Q, can also be measured by oscillating the cantilever at a set amplitude, turning off the drive, and observing the decay of the oscillation amplitude. By fitting the decay to an exponential, the decay time, τ, can be determined. From this decay time, Q can then be derived using [93]

$$Q = \frac{\omega_0 \tau}{2} \tag{2.8}$$

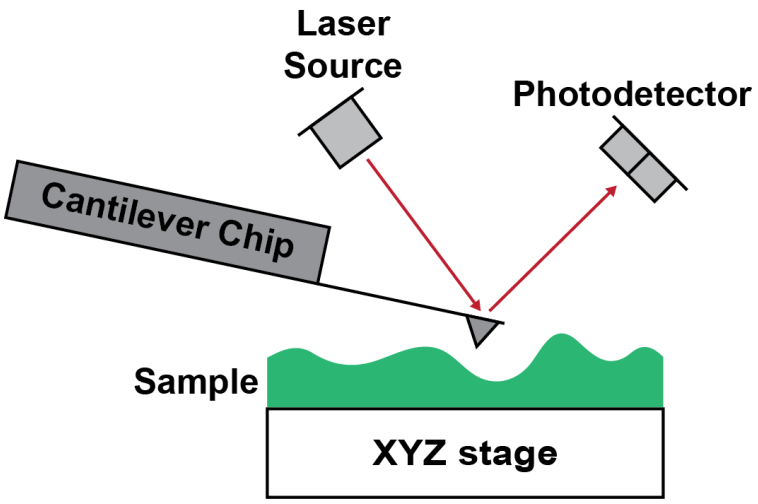

Figure 2.8: A diagram of the a common AFM displacement setup. This setup is not used in this work due to size constraints and issues with maintaining laser alignment during cooling/warming.

2.1.3 Detection Methods

Detection of the cantilever displacement can be done in a number of ways. The most common method currently used for SFM is the "laser bounce," where a laser beam is reflected off the cantilever into a set of photodetectors (see Fig. 2.8). The difference in light collected by the photodetectors gives a readout of the cantilever oscillation. Due to the larger area required, as well as possible issues with laser alignment during cooling, a different method of displacement detection is used in this experiment.

We utilize an interferometer for our setup, since it requires only a single optical fiber entering the vacuum space. The interferometer observes the optical path difference between reflections from the cleaved end of an optical fiber and the reflecting pad of the cantilever[102]. A deflection, u, of the cantilever will change the path difference between the light reflected from the fiber and that reflected from the cantilever. The intensity of the reflected signal will be given by the well-known formula

$$I(u) = I_f + I_c + 2\sqrt{I_f I_c}\cos\left(\frac{4\pi(u+Z)}{\lambda}\right) \tag{2.9}$$

where I_f, I_c are the intensity of light reflecting off the fiber and cantilever, Z is the equilibrium distance from the fiber to the cantilever, and λ is the wavelength of the laser. This intensity is converted into an analog voltage signal that will have minimum and maximum values V_{min} and V_{max}, respectively.

To determine the cantilever deflection through this setup, we utilize the fact that the cantilever deflection (typically < 50 nm) is much smaller than the laser wavelength (1510 nm). Using a thermo-electric cooler (TEC) installed in the laser diode, the laser wavelength can be finely-tuned so that $Z = \lambda(n + {}^1/_4)/2$.

Assuming small deflections, we can then expand the cosine function around the midpoint of the fringe (halfway between the minimum and maximum), leading to the voltage signal to be

$$V(u) = \frac{V_{max} + V_{min}}{2} + 2\pi u \left(\frac{V_{max} - V_{min}}{\lambda} \right) \tag{2.10}$$

V_{max} and V_{min} are the extrema of the interference fringe, measured while tuning the laser wavelength. This allows accurate measurement of the cantilever deflection.

2.1.4 Noise and Force Sensitivity

The interferometer allows monitoring of the cantilever vibration at one point along its length. Due to our knowledge of where the laser is positioned, as well as the vibration mode shape of the cantilever, we can find the room-mean-square (RMS) displacement of the cantilever tip, x_{rms}, which represents the amplitude of the cantilever vibration noise at a given temperature. Measurement of the RMS displacement is used at room temperature to determine the spring constant of the cantilever, according to the equipartition theorem [30,103]:

$$\frac{1}{2} k x_{rms}^2 = \frac{1}{2} k_b T_{eff} \tag{2.11}$$

where k is the spring constant, and k_b is the Boltzmann constant. At room temperature, T_{eff} generally follows the thermal noise in the system, although at lower temperatures, added noise from external sources, such as laser-induced heating of the cantilever and detector noise, among others, can increase the effective temperature of the cantilever. The system is vibrationally isolated from the room, minimizing errors from other vibrational sources.

For FM detection, and assuming the noise is thermally limited, the minimum detectable force gradient is then given by [30]

$$\delta F_{min} = \sqrt{\frac{4 k k_b T B}{\omega_0 Q x_{rms}}} \tag{2.12}$$

where B is the detection bandwidth. For high force resolution, the probe should be designed to have a low spring constant, k, be operated at a low temperature, T, and have high resonant frequency, ω_0, and high quality factor, Q.

Other considerations to maximize signal are also made. First, the laser wavelength was selected to ensure a photon energy less than the bandgap of silicon. Ensuring constructive interference for laser reflections maximizes the interferometer signal, and a 100 nm thick Si cantilever ensures the proper phase difference.

2.2 Fabrication

2.2.1 Cantilever and Magnet Fabrication

The cantilever used in this work is a custom-fabricated ultra-soft cantilever, made by Benjamin Chui and Trevis Crane at the Stanford Nanofabrication Facility. Cantilevers are fabricated from a (111)-oriented silicon-on-insulator wafer. Prior to use, the cantilevers are stored in a nitrogen dry box to minimize exposure to air. The spring constant of the cantilevers[1] are 100-300 μN/m, with frequencies of 4-8 kHz, and quality factors (at 4 K) of at least 30,000. Cantilever dimensions are approximately 100 μm length, 4 μm width, and 100 nm thickness, with an octagonal pad to aid in laser reflection $\sim$80% of the way up the lever (see Fig. 2.4).

Using a micro-manipulator, a small piece of $SmCo_5$ magnet is attached to the end of the cantilever. The magnet, <5 μm in size, is aligned with the cantilever axis using an external field, and affixed to the cantilever using Gatan G-1 epoxy. Curing of the epoxy is done in a nitrogen atmosphere to prevent oxidation of the magnet. The cantilever and magnet are then loaded into a testing setup at room temperature. The testing setup can apply a magnetic field up to 1000 Oe parallel to the cantilever axis. When this field is applied, the cantilever frequency will shift in response, allowing an estimate of the magnetic moment of the tip along the cantilever axis. Another set of data is taken on the bending of the cantilever with applied field, giving an estimate of the out-of-plane magnetic moment as well. By comparing these two moments, we gain an estimate of how well the magnetic moment aligns with the cantilever axis. If the two are fairly well aligned (generally $<10^\circ$), we then proceed to shape the tip. Problems with alignment are usually due to the particle being primarily magnetized in the out-of-plane axis, which is undesirable for this work.

Shaping of the tip is done in a focused ion beam (FIB) machine. This machine contains an SEM, as well as a Ga ion source that can be used for imaging or cutting of samples. Using the SEM as an imaging system, and taking care not to image the shaft of the cantilever, as this can damage the quality factor, the ion beam is used to cut away material on the end of the cantilever. Any Si at the tip is removed, so that the $SmCo_5$ is close to the surface. Multiple tips/cantilevers are used in this work, with two general designs. On the first, $SmCo_5$ is also shaped so that there is a roughly cubical piece attached to the cantilever, with a smaller section jutting out past the end of the cantilever itself as shown in Fig. 2.9A. The cubical piece is used to keep the smaller section magnetic, as some ion damage does occur on the magnet, even with the small ($<$10 pA) ion currents used for shaping the tip. The second lacks the spike jutting from the larger portion, and is shaped into a slight taper at the end, as can be seen in Fig. 2.9B. After shaping, the cantilever is

[1] Spring constant is measured from the thermal spectrum of the cantilever

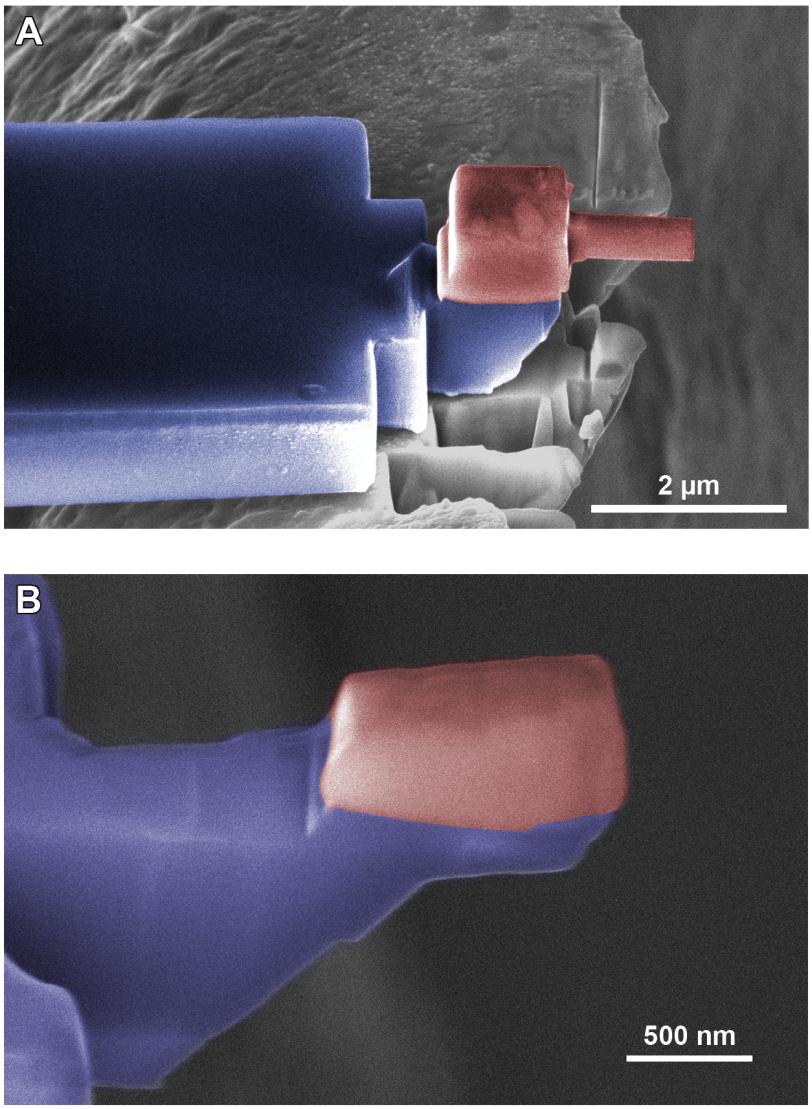

Figure 2.9: SEM images of two $SmCo_5$ tips (red) attached to the end of Si cantilevers (blue). (**A**) A cubical tip with a 300 × 300 nm^2 spike extending towards the surface. (**B**) A cubical tip with slight taper.

again loaded into the testing system to confirm the magnetism of the tip before being loaded into the low temperature system.

2.2.2 Sample Fabrication

For this experiment, SNS arrays were fabricated in an equilateral triangular arrangement[2]. The substrates used were Si, with an insulating oxide layer (thickness 300 or 1000 nm) grown on the surface via thermal oxidation. Definition of features was done for all metal layers using an electron-beam (e-beam) lithography device (Raith e-Line) and PMMA e-beam sensitive resist. All metal layers were grown using an UHV e-beam evaporator with a base pressure of $< 1 \times 10^{-9}$ Torr. The normal metal layer, deposited first, is 18 nm thick Au, with a 1 nm Ti layer underneath to promote adhesion to the substrate. In one sample used in this work, the Au was in a four-point configuration for measurement of electrical properties of the array. For the other sample, the Au layer was formed into a long wire with several meanders, as can be seen in Fig. 2.10. Island arrays were designed to be placed in several areas of the wire, with voltage leads on select array areas.

Next, a series of 50 nm tall registration marks are defined and deposited. These registration marks are 45 nm tall Al, also with a Ti adhesion layer of thickness 5 nm. Each registration mark is a unique geometric code, along with a piece to define a direction to make interpretation unambiguous. These marks are used in navigating the surface of the sample with the cantilever. They are spaced every 20 μm in the $\hat{x}$- and $\hat{y}$-directions, so that one falls within our scan range at base temperature. Registration marks were not placed within ~ 20 μm of the SNS arrays, to minimize possible proximity induced effects from their presence. Al was selected as a material for these registration marks due to it being used on the sample chip for a separate experiment, as well as the superconducting transition temperature (~ 1.1 K) being sufficiently low compared to that of Nb so that it would be in the normal state while collecting data on the SNS arrays.

A bilayer of PMMA, consisting of a layer of 495k A2 PMMA underneath a layer of 950k A2 PMMA was used to define the Nb islands. The lower molecular weight of PMMA will dissolve more readily in the MIBK developer used in this experiment, leading to an undercut in the resist. This undercut aids lift-off of the Nb and helps alleviate "dog-ears", or small fingers of metal that jut up from the edge of the islands. These fingers can be several hundred nm tall, so preventing them is critical to scanning close to the surface, as well as preventing possible damage to the cantilever tip from impacts with the dog-ears. Prior to the evaporation of the Nb, the Au surface is Ar^+ ion milled for ~ 30 seconds to remove contaminants, as well as promote a clean interface. The 80 nm tall Nb islands are then deposited at a pressure of $< 8 \times 10^{-10}$ Torr, as the superconducting transition temperature of Nb is very sensitive to contaminants. The evaporation was done

[2]Malcolm Durkin and Rita Garrido-Menacho fabricated or aided in the fabrication of the samples.

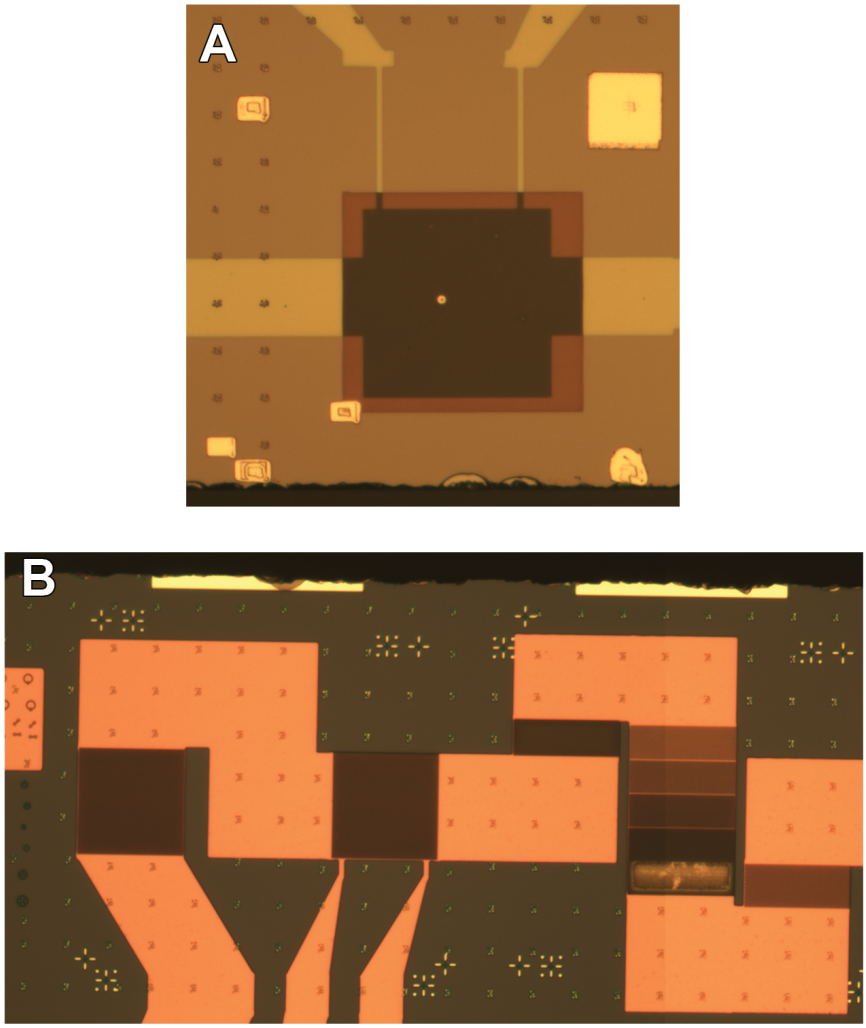

Figure 2.10: Images of the samples used in this work. (**A**) 80 $\times$80 μm^2 array of 500 nm center-to-center islands. (**B**) Multiple arrays on a long Au wire. The two square arrays (50 $\times$ 50 μm^2) on the left are spaced 500 nm center-to-center. The stacked rectangular arrays (50 $\times$ 15 μm^2) are, from second to the bottom (bottom is solid Nb): 440 nm, 500 nm, 560 nm, and 620 nm center-to-center spacing. The other two rectangular arrays at far right and middle are not used in this work.

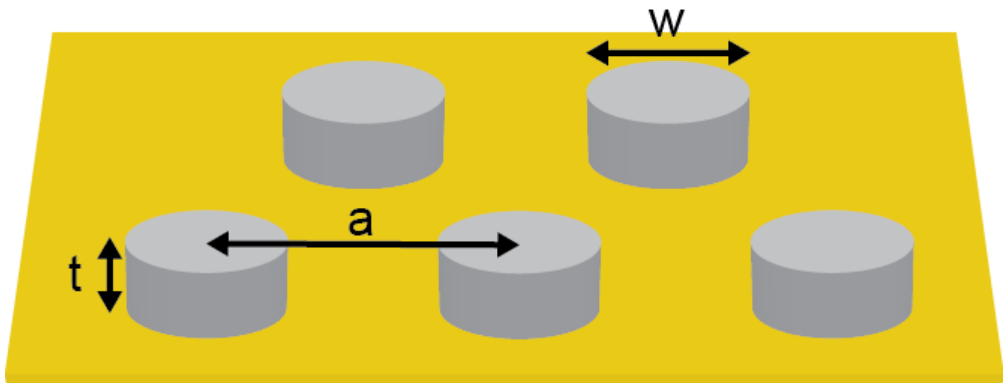

Figure 2.11: Nb islands are arranged in a triangular pattern, with center-to-center island spacing a, which varies from 440 nm to 560 nm in this work. The island thickness is set at $d = 80$ nm for all arrays. The island diameter is approximately $w = 260$ nm.

in two parts to prevent excessive heating of the vacuum system, without breaking vacuum on the sample in between. These strategies enable deposition of a superconducting Nb film via e-beam evaporation with a transition temperature near that of bulk Nb (9.2 K).

The metals used for the SNS arrays were selected previous to this work by Serena Eley [24]. A brief overview will be given here. Au was selected as the normal metal due to its resistance to oxidation, non-magnetic character, and ability to form a continuous film. Nb was selected due to its high superconducting transition temperature (9.2 K in bulk), clean lift-off properties, and compatibility with the Au film.

The array dimensions (Fig. 2.11) were chosen based on previous work done by Nadya Mason's group at UIUC. For this work, the Au underlayer is 18 nm thick, with a 1 nm Ti sticking layer. The Au thickness was increased from previous works by that group to strengthen the superconducting condensate in between the islands. The Nb thickness of 80 nm was chosen to keep the superconducting transition temperature of the system high, while still allowing the cantilever tip to get relatively close to the Au surface, and the island separations were also chosen to ensure that both transition temperatures (for the islands and full array itself) would be in an accessible range for our ^{3}He microscope. The island separation for the majority of this work is 500 nm center-to-center, with some arrays having a spacing of 440 or 560 nm. Unless noted, the array spacing is 500 nm. The island diameter of approximately 260 nm is the same in all cases.

After all lift-off steps are completed, the sample is coated in photoresist (AZ5214, Microchem), and left to dry at room temperature in a nitrogen atmosphere for several hours. Baking of the photoresist was found to impact the superconducting properties of the sample, possibly due to diffusion at the Au/Nb interface. Once the photoresist is dry, the sample is mounted to dicing tape and diced on a wafer saw. The diced edge is <150 μm from all arrays. This distance is necessary with the cantilever set up in a pendulum configuration

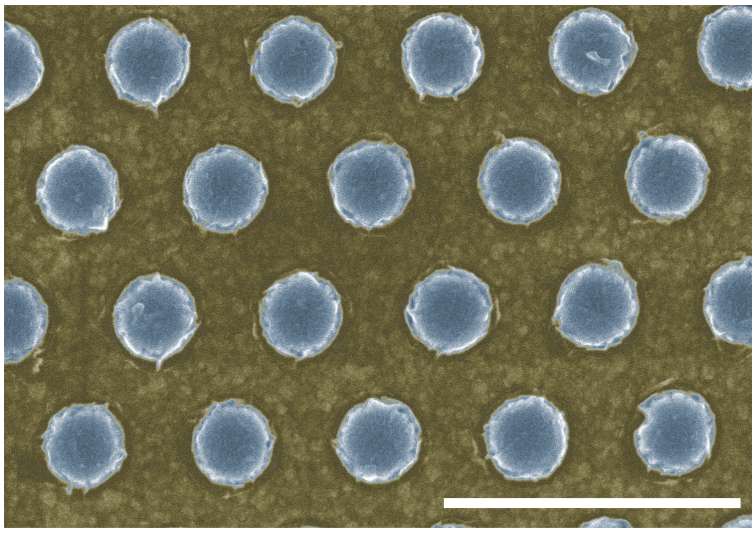

Figure 2.12: False color SEM image of an island array with 500 nm center-to-center spacing. Scale bar is 1 μm.

as in this work, as the laser may also reflect from the edge of the chip, lowering the visible signal from the cantilever itself.

2.2.3 Array Transition temperature and magnetoresistance

To determine if the arrays were superconducting, as well as the transition temperature of the arrays, transport data was collected using a four-point configuration. For the first sample (Fig. 2.10A), the system began to transition at approximately 6.0 K, with superconductivity established across the array at approximately 4.0 K, as can be seen in Fig. 2.13. The second sample (Fig 2.10B) has a higher transition to superconductivity across the array at approximately 6.0 K (Fig. 2.13c). This higher transition temperature is likely due to a better interface between the Nb and Au, as well as more pure Nb from deposition at lower pressures, as Nb is sensitive to impurities. For this sample, only a single 50×50 μm array can be measured via transport, owing to a lack of wiring on the sample and in the microscope.

The magnetoresistance of the samples (Figs. 2.13 b and d) show the expected behavior. The magnetoresistance dips at certain rational frustrations where the vortex lattice is commensurate with the Josephson junction array. At these frustrations, the vortices are pinned by the presence of the other vortices in the array, making it hard for vortices to move and dissipate energy. At these magnetic field values, therefore, the resistance of the array decreases. The prominent dips line up with the most prominent dips as seen in other arrays of this type[24,43]. These magnetoresistance curves, as well as the resistance vs. temperature data, make us confident that the arrays are superconducting at the temperatures that are used in these

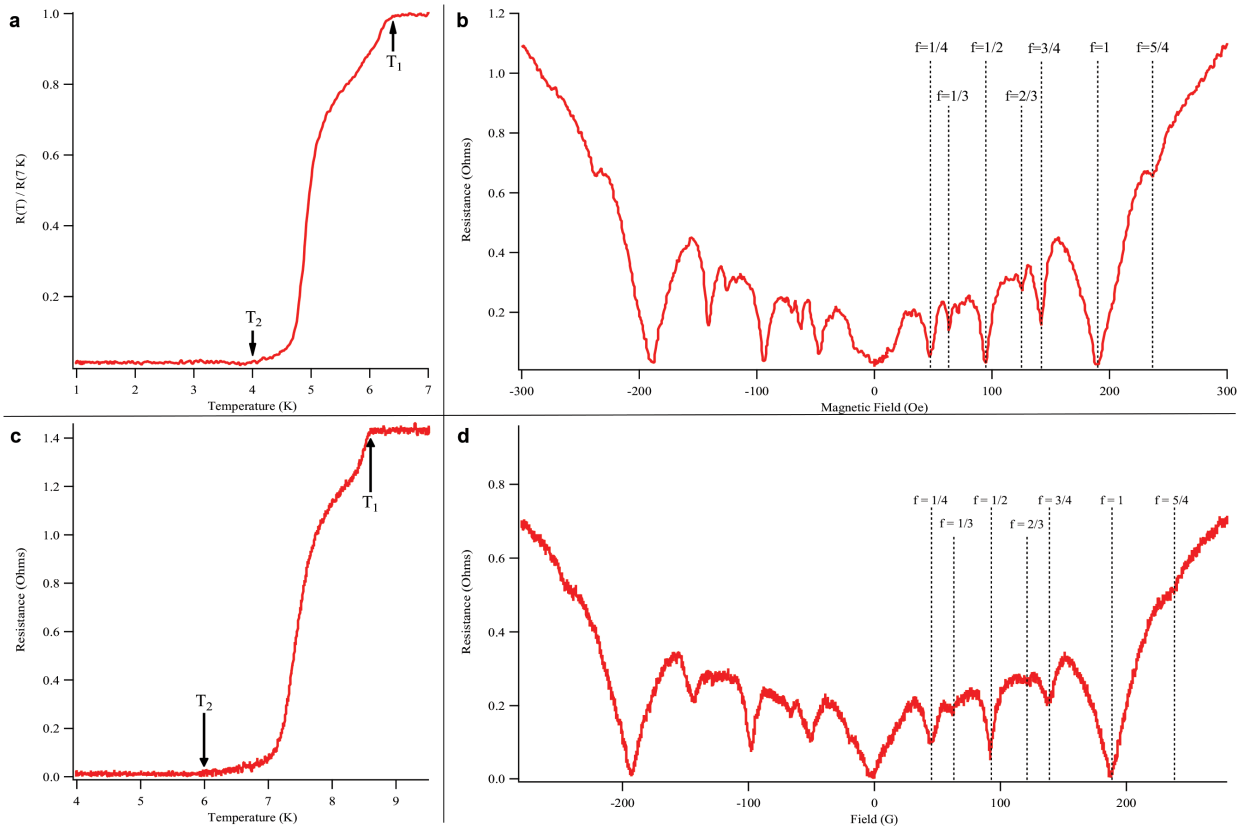

Figure 2.13: Transition temperatures and magnetoresistance curves for the samples presented in this thesis. (**a**) Resistance vs. temperature for the array displayed in Fig. 2.10A, showing superconductivity across the array at 4.0 K. (**b**) Magnetoresistance for the same array, displaying dips in the magnetoresistance at commensurate fillings, where the vortex pattern is pinned. (**c**) R vs. T for the 50 $\times$ 50 μm array with voltage taps shown in Fig. 2.10B. This array had a higher transition temperature of approximately 6.0 K. (**d**) Magnetoresistance of the 50 $\times$ 50 μm array, showing the same magnetoresistance dips as the previous sample, as expected.

MFM experiments.

2.3 Instrumentation and Setup

2.3.1 ^{3}He Microscope

Data is taken on a continuous-flow ^{3}He microscope with a base temperature of 280 mK when used in a single-shot mode. The sample and cantilever are placed inside a ultra-high vacuum (UHV) chamber at the bottom of the microscope (See Fig. 2.14), with typical pressures of $\sim 10^{-8}$ Torr, which minimizes damping of the cantilever due to the surrounding atmosphere. Surrounding the UHV chamber is an inner vaccum chamber (IVC), which thermally separates the ^{3}He portion of the microscope from the warmer ^{4}He bath. At the top of the IVC is a 1K pot. The 1K pot is a chamber that is filled with ^{4}He from the bath surrounding the IVC, and the helium inside is pumped to achieve temperatures of approximately 1 K. The ^{3}He gas is passed through this reservoir, then adiabatically expanded to further cool it, at which point it liquefies. The liquid can then boil off and the gas is pumped away from the liquid. While in continuous flow, a base temperature of $\sim$ 350 mK is typical. ^{3}He gas that boils off is cleaned of impurities in a LN_2 trap, and returned to the microscope. A 6 Telsa superconducting magnet (Cryomagnetics, Inc.), with field perpendicular to sample surface, is also installed in the system to enable magnetic field studies.

2.3.2 Sample Mounting

The sample is mounted onto a copper (Cu) mounting block by way of two steel spring clips on the edges of the sample. The sample is mounted so that the area to be scanned is on or overhanging one edge of the sample mount, so that it can be accessed by the cantilever and laser interferometer. The end of the mount opposite the cantilever contains a PCB board which is used for the strain relief of the sample's electrical connections. A wedge bonder is used to connect the sample to this PCB for electrical measurements. From the PCB to the microscope body, Cu wires are used for the current paths, while phosophor-bronze wires are used for the voltage leads. All wires are paired and twisted to reduce electrical noise.

The Cu sample mount is attached to the imaging stack by a pair of set screws. The top portion of the imaging stack is a Cu piece that also holds two temperature sensors, a heater, and a grounding wire. The two temperature sensors have different temperature ranges: a Cernox CX-1070 (Lake Shore Cryotronics, Inc.), used above 20 K, and a Ruthenium Oxide (RuOx) sensor (RX-102A, Lake Shore Cryotronics), used below 20 K. Both sensors have very low magnetic field response in their respective ranges, and the RuOx sensor is accurate at low currents, minimizing heating effects from the sensor. A temperature controller (Lake Shore

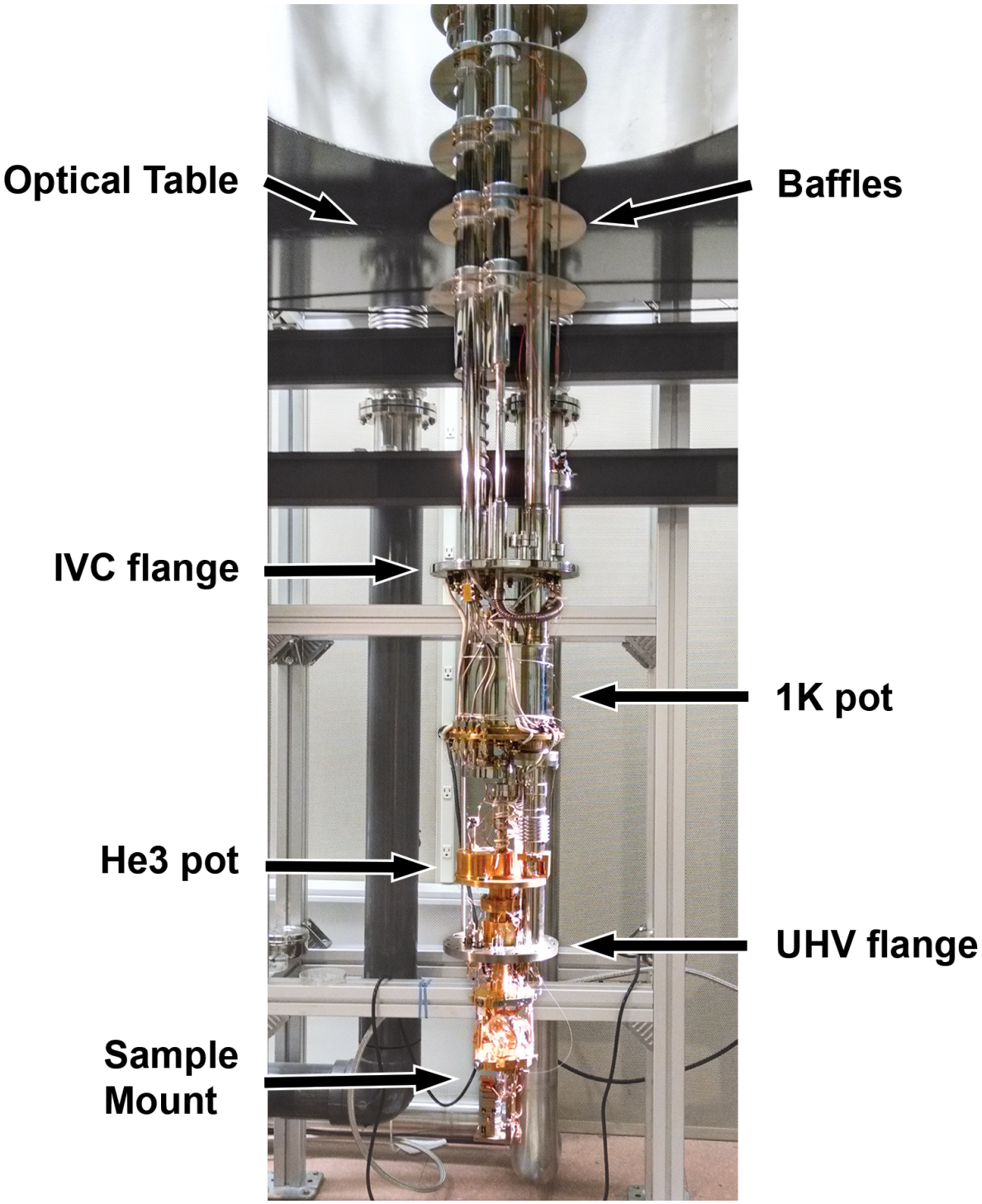

Figure 2.14: The MFM microscope mounted in a ^{3}He fridge. When in operation, a UHV can will be installed on the UHV flange, and another can on the IVC flange so those areas can be vacuum pumped. The system fits inside a dewar with a 6 Tesla magnet installed.

340) is used to regulate the temperature of the sample within <5 mK of the desired temperature via a PID loop. At temperatures above $\sim$ 6 K, the ^{3}He is removed from the system, and the IVC filled with ^{4}He exchange gas to better regulate the sample temperature by placing it in thermal contact with the ^{4}He bath.

Above the sample, the cantilever is mounted in a pendulum orientation. This orientation is necessary due to the extremely small spring constant of the cantilever. In the more common horizontal orientation, cantilevers with small values of k exhibit "snap-in", where Van-der-Waals forces attract and hold the cantilever to the surface when it is approached, precluding scanning [98,104]. The cantilever is held in place by a spring clip, and a piezoelectric plate sits underneath. The piezoelectric plate is used to drive the cantilever oscillation, as discussed below.

2.3.3 Movement stack

The lower section of the imaging stack holds the positioners and scanner for the experiment, as seen in Fig. 2.15. On top is a three-axis Ti piezoelectric scanner (Attocube ANSxyz100) used for the scanning and fine positioning of the sample. The scanner has a range of $30 \times 30 \times 15$ μm^3 in the x, y, and z directions, respectively, at 4 K. Underneath the scanner are three Ti-body piezoelectric stick-slip positioners ((2x) ANPx100 and (1x) ANPz100, Attocube), used for coarse positioning of the sample. The range of the scanners is $5 \times 5 \times 5$ mm^3. Resistive encoders built into the positioners read the relative position of the sample. Positioners are turned off (no position readout) while scanning to minimize unwanted heating of the sample.

The sample and cantilever mounts are separated from the rest of the microscope by springs to minimize mechanical noise driving the cantilever, with Cu braids maintaining thermal contact. The microscope and He dewar are held by an optical table, which is also floating on compressed air to prevent mechanical vibration. During low-temperature scanning, the turbo-pumps used to evacuate the UHV chamber and IVC are turned off to eliminate vibration from the operation of the pumps themselves. The table and system are contained in a noise-damping room in the basement level to minimize vibration from other sources.

2.3.4 Fiber-optic interferometer setup

The cantilever oscillations are detected by a fiber-optic laser interferometer. A fiber-coupled laser diode (OL5109L-5A 5mW 1510 nm DFB Laser, OKI Optoelectronics) is used as the laser source. Power is supplied by a low noise current source (LDX-3620, ILX Lightwave), typically set at 17 mA. The current is modulated by a 200 MHz RF signal, generated by a voltage-controlled oscillator (ZX95-400, Mini-Circuits), which is passed through a voltage-variable attenuator (5 dB, Mini-Circuits). This modulation reduces optical

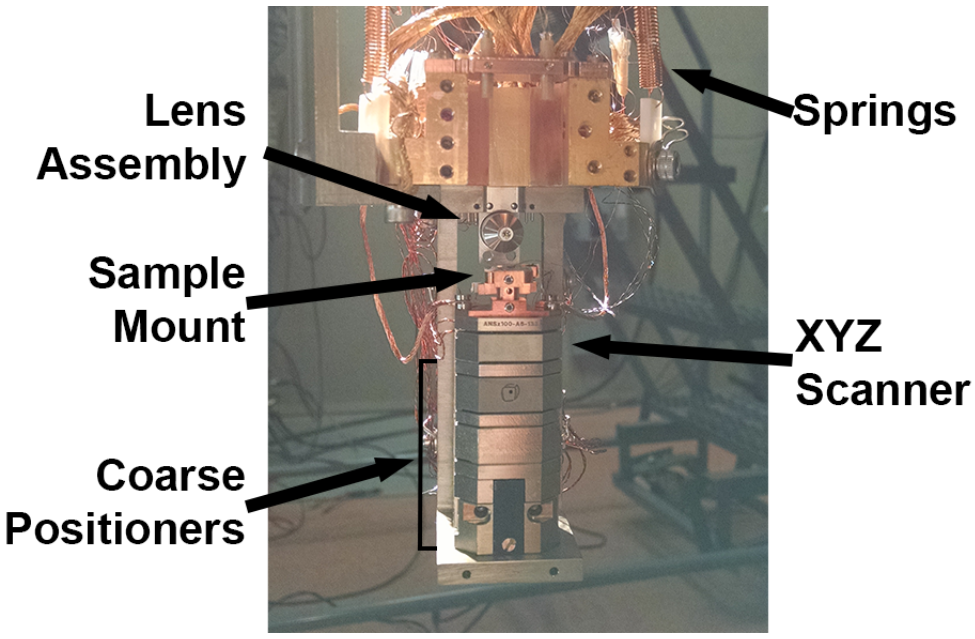

Figure 2.15: Image of the scanning setup in the UHV chamber.

feedback noise and interference noise by reducing the laser coherence length. Absent the modulation, the laser coherence length is several centimeters. The laser wavelength is tuned using a thermoelectric cooler installed in the laser diode, and controlled using a home-built controller and LabVIEW program. Signal from the laser is converted into a voltage using a photodiode in conjunction with a transimpedence amplifier (LMC6001, Texas Instruments), and amplified using DC-coupled and AC-coupled SRS560 low-noise preamplifiers.

The laser path to the cantilever is shown in Fig. 2.16. The output of the laser is fiber-coupled, and is connected to a voltage controlled optical attenuator (MMVOV-1-1550-5-9/125-3A3A-0.25-1, OZ Optics). A PID loop controls the attenuation so that a desired laser power may be set, with laser powers (sent to the cantilever) in these experiments ranging from about 25 nW to 1 μW. The laser driving current is not changed during the experiment. The output of the attenuator goes into the input port of a 99:1 directional coupler (FFC-X142PB1XX-SFO572, JDS Uniphase). The majority (transmission terminal) of the laser light is sent to a fiber-coupled photodiode (FCI-InGaAs-70-SM-FC, OSI Optoelectronics), which is used to determine the power of the laser. The forward coupled laser light is sent into a long fiber, which leads into the UHV chamber of the microscope to monitor the cantilever. Feeding the fiber into the vacuum space was done using a Swagelok connector and Teflon ferrule[3], following the design of Ref.[105]. The back coupled laser light enters a photodiode identical to the transmission terminal to generate the laser signal.

To get a good interferometry signal from the cantilever, the fiber end is cut using a commercial optical

[3]Teflon and Swagelok are trade names, and are used only for identification

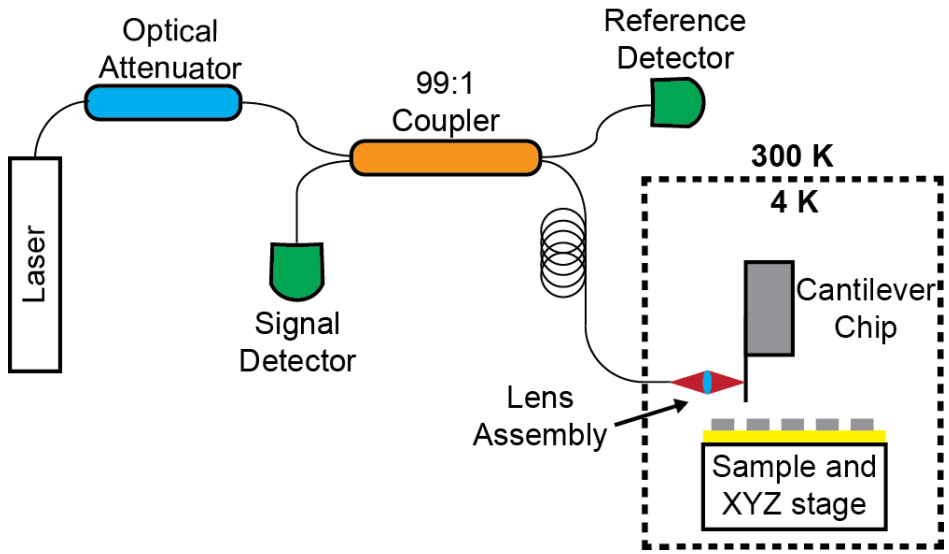

Figure 2.16: Schematic of the fiber-optic Fabry-Perot interferometer. This setup is well suited for cryogenic applications due to the small size of the package in vacuum, as well as only requiring one cryogenic feedthrough.

fiber cleaver (S323, FITEL), with the coating layer stripped. Approximately 4% of the laser light is reflected from the end of the cut fiber. The end of the fiber is inserted into a lens assembly, consisting of a machined stainless steel tube, with a borosilicate ferrule of dimensions 14 mm length, 129 μm ID, and 1 mm OD (BD ACCU-GLASS) epoxied into it. At the end of the steel tube, a small lens (350350C00 coating:10238, LightPath) with focal length 1.6 mm, is epoxied using TorrSeal (Varian, Inc.). This setup is used to position the end of the fiber at the focus of the lens, where it is epoxied into place using Torr Seal. This tube is then inserted into a stainless steel fiber positioner for alignment with the cantilever.

2.3.5 Interferometer Design

The DC-coupled cantilever signal, after leaving the preamplifier, goes to the input of an FPGA. The FPGA controls the thermoelectric cooler attached to the laser diode, and will change the current going to the cooler to adjust the wavelength of the laser so that the interferometer signal is in the center of a fringe (highest slope). This is done because the highest distance/voltage change occurs at the fringe center.

The AC-coupled cantilever signal is split, going to both a second port on the FPGA, and to an amplitude control box. The FPGA uses a phase-locked loop (PLL) to determine the cantilever frequency, as diagrammed in Fig. 2.17. The displacement signal is sampled using a square wave generated by a function generator (Agilent 22330A, Agilent) as a trigger. Samples are summed in the first and second halves, and the difference between sums (half-sum-difference) is computed. A PID algorithm running on the FPGA compares this

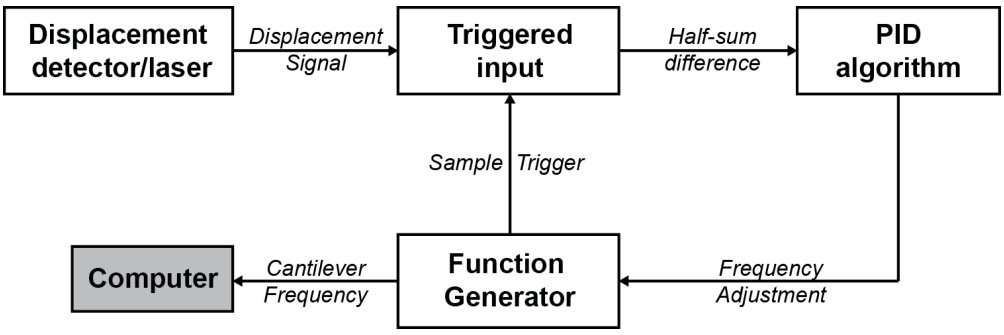

Figure 2.17: The Phase-Locked-Loop setup used for determining the frequency of the cantilever.

half-sum-difference to a set point of zero, and adjusts the frequency of the square wave to minimize the half-sum-difference. The frequency of the function generator is then used to determine the frequency of the cantilever.

2.3.6 Scanning

The sample is raster-scanned in one direction to form the images, followed by a faster (non-scanning) motion to the beginning of the next line. Though the scan can be done in any orientation, the fast scan axis is in the $\hat{y}$-direction, unless otherwise noted. The slow scan axis goes from left to right in the images presented here. Scanner positioning is done by an FPGA in conjunction with a 3-axis piezo controller (Thorlabs MDT693B). The FPGA exports the sample position, along with the cantilever frequency, dissipation, amplitude, and two extra read-in ports, to the computer. Prior to scanning the surface, touch points are determined for four positions surrounding the scan area. A plane is generated from these points, and the tip is scanned at a fixed height above this sample plane in each scan. Scanning speed and density of sample points is also set for each scan. Typical scanning speeds in this work are <300 nm/sec. Prior to scanning each line, the cantilever is paused for a short period to eliminate any spurious oscillations that may have been caused by the faster motion to the start of the new line.

Chapter 3

Imaging

3.1 Pattern Formation

When placed above the surface of the Josephson Junction Array, the magnetic field of the tip attached to the end of the cantilever creates a potential well for vortices to lie in. An external field can be used to change the depth of this well, and the height of the tip modifies the depth and width simultaneously. For the arrays under consideration here, when the tip is 200-700 nm above the Au surface (Nb height is 80 nm), this potential well traps a small number (1 to approximately 15) of vortices underneath the tip. These vortices, which sit at the center of the array plaquettes, will follow the potential well as the tip moves over the surface to scan, and will re-configure themselves to minimize their energy. Outside the potential well from the tip, anti-vortices (vortices with opposite circulation) will be generated by the external field.

With the cantilever positioned above the sample surface, the vortices trapped underneath the tip will adopt some configuration to minimize the system energy. Then, as the tip scans over the surface, it will reach points at which the energy of the first configuration becomes degenerate with the energy of another distinct vortex configuration. At these points, the oscillation of the tip, along with the thermal motion of the vortices, can cause the vortices to hop between the two configurations, a phenomena known as *stochastic resonance*. Currents from the vortices will then also shift between two configurations to reflect the change in vortex configuration. When the currents change back and forth between the two configurations, they change the force on the cantilever tip, and may cause a shift in the resonance frequency of the cantilever if the shifting force is along the oscillation direction of the cantilever. This method of imaging has recently been described[106], and is termed Φ_0-MFM. In Fig. 3.1, this frequency shift is seen as dark lines. The lighter areas in this figure are points at which the vortex configuration is stable, or there is no shifting force on the cantilever in the $\hat{y}$-direction. The $\hat{y}$-direction is the oscillation direction of the cantilever, and the spring constant of the cantilever is lowest bending in that direction, and thus its sensitivity is highest. Changes to the vortex configuration that result in forces on the cantilever in purely the $\hat{x}$-direction will not be visible, owing to the fact that the cantilever is stiff in that direction. Fig 3.2 illustrates how the darker lines are

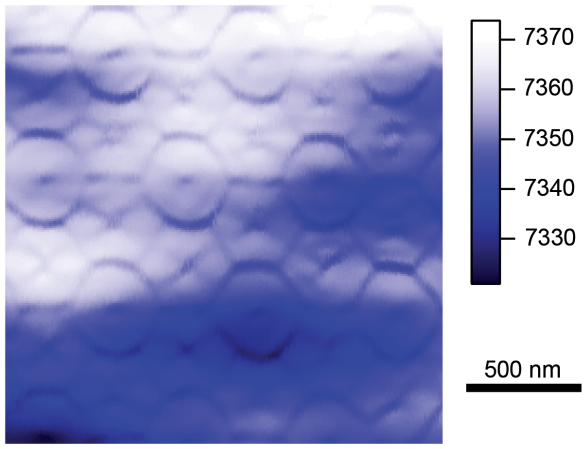

Figure 3.1: Image showing a hexagonal pattern generated by scanning over the JJA. A small number of vortices are trapped underneath the tip. As the tip scans, this vortex configuration becomes equal in energy with another configuration, and the vortices oscillate between the two configurations in sync with the cantilever, changing the cantilever frequency. This frequency shift is visible as dark lines on the image. Lighter areas are where the vortex configuration is stable.

formed when the vortices switch between two configurations.

A slowly varying background is also visible in many of the images. This background is primarily due to topographic and material changes on the surface, and not the vortex configuration changes that we are interested in. Since this background is very diffuse as compared to the energy degeneracy lines, we remove the background by applying a Gaussian filter to the data and subtracting the result of that filter from the frequency shift data given in the experiment. Fig. 3.3 shows the data, filtered data, and subsequent clean image. By doing this, we highlight the patterns showing the energy degeneracy points and gain more easily visible data on the locations of the energy degeneracies. Most data presented below in this thesis will have the background removed to highlight the discussed features.

Fig. 3.4 displays a few vortex patterns with the background subtracted. The different subfigures show the patterns generated as different numbers of vortices change configurations underneath the tip. From a relatively simple triangular pattern in the three vortex image (Fig. 3.4a), the pattern shifts to "dots" (4 vortices, Fig. 3.4b), to more complicated patterns with 5 and 6 vortices (Fig. 3.4c and d). Below the images themselves are the vortex configurations as determined via an energy minimization procedure (see Chap. 4 for detail). The positions of these vortex configuration changes, and thus the energy degeneracy points, are repeatable over many scans.

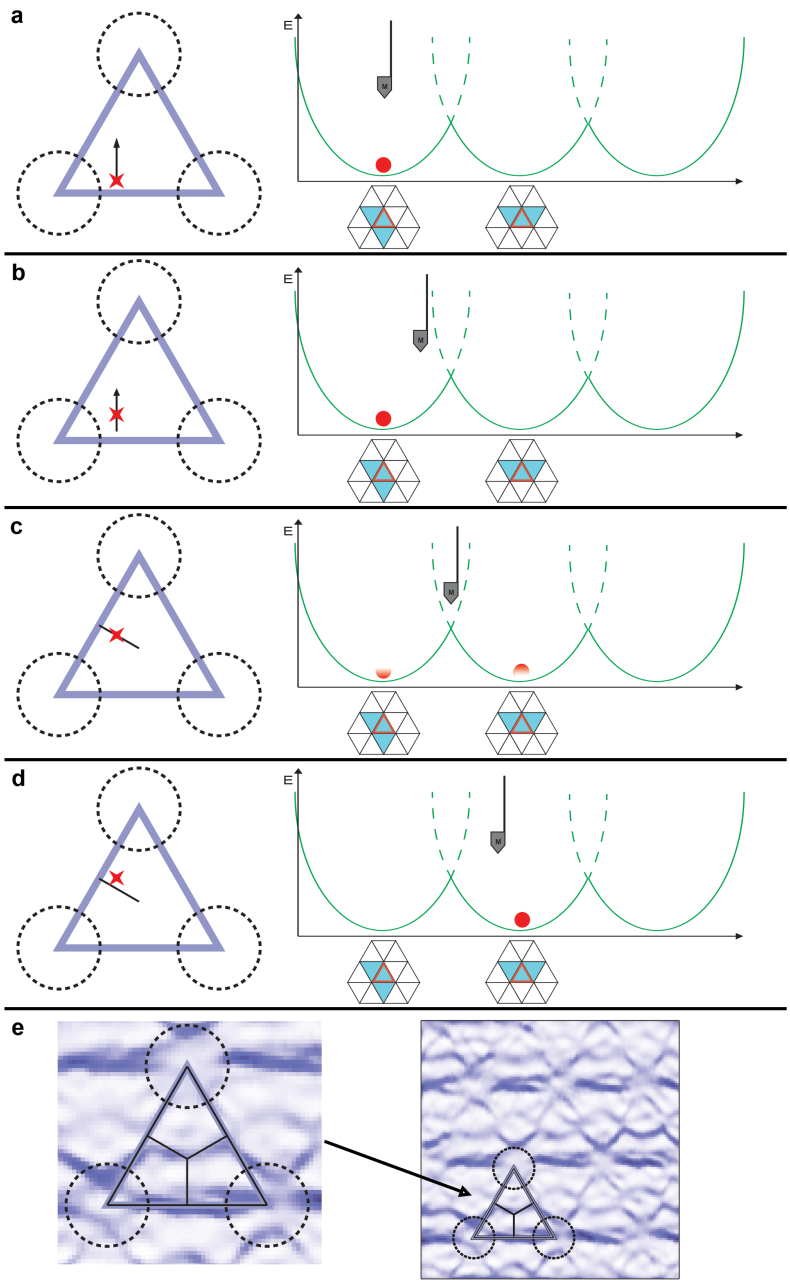

Figure 3.2: Figure showing how the image is formed. To the left is a plaquette, with the tip location marked by the red star. On the right is the energy of different vortex configurations. Starting in (**a**), the tip begins a scan at some location. The vortex configuration adopts the lowest energy state for the tip location. (**b**) As the tip moves, the energy of the vortex configuration begins to increase. (**c**) When a point of energy degeneracy between two vortex configurations is reached, the tip oscillation, along with thermal energy of the vortices, causes the vortices to hop between two configurations. This changes the frequency of the cantilever. (**d**) As the tip moves past the energy degeneracy point, the vortex configuration settles into a new lowest energy state, and the cantilever frequency returns to its natural resonance frequency. (**e**) Imaging continues until all of the visible degeneracy points are mapped, resulting in a pattern in the image.

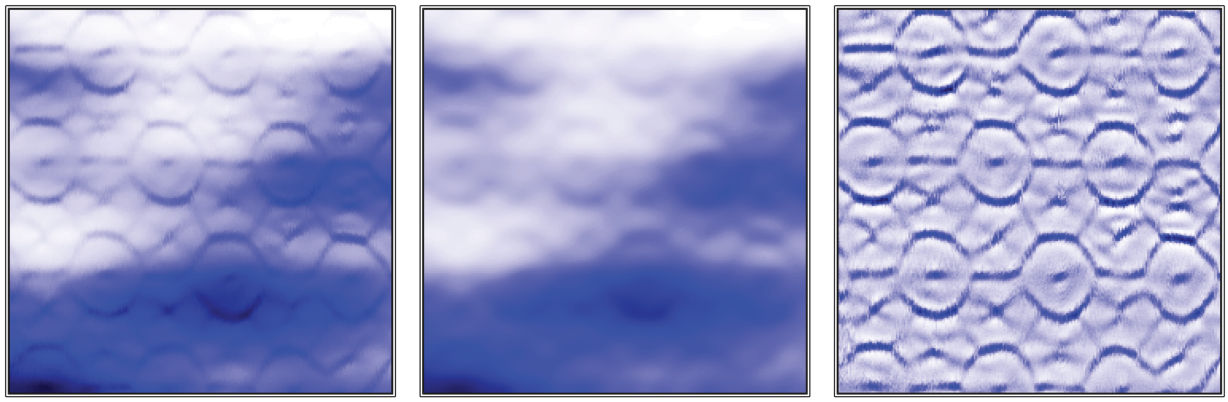

Figure 3.3: Example of the background subtraction. (**a**) The original frequency data, as in 3.1. (**b**) A Gaussian filter is used to fit the data and extract the background. (**c**) The background data is subtracted from the original data, highlighting the pattern formed by the stochastic resonance imaging. All images are $1.6 \times 1.6 \mu\text{m}^2$.

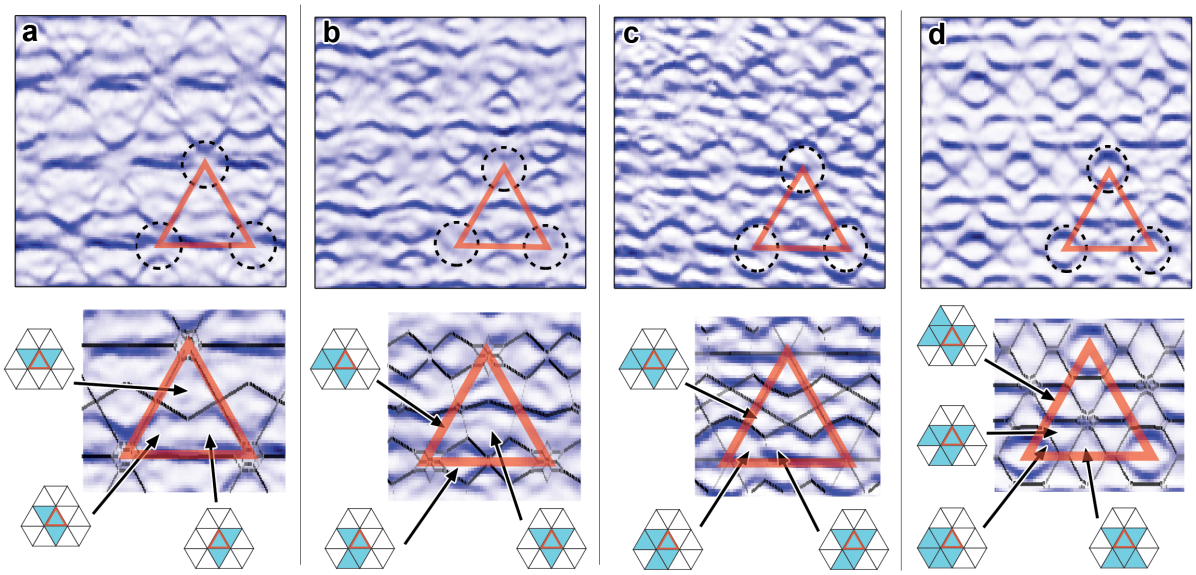

Figure 3.4: Another set of images of patterns formed at different fields. Island positions and an example plaquette are overlaid. Below each image is a diagram showing the vortex configurations, as determined in Chap. 4. (**a**) is a pattern with 3 vortices underneath the tip at 124 Oe. (**b**) 4 vortices at 104 Oe, (**c**) 5 vortices at 89 Oe, (**d**) 6 vortices at 79 Oe.

3.2 Stochastic Resonance

Stochastic resonance is a phenomena in which a small signal is amplified by the presence of noise in the system [107]. In this work, the thermal energy of the vortices in the array, when added to the oscillations of the tip, drive the vortices between two configurations in resonance with the tip oscillations, giving rise to a measurable frequency shift. We will briefly review the principles of stochastic resonance and its application to our system.

To explain the basics behind stochastic resonance, we turn to a particle trapped in a double-well potential (see Fig. 3.5). We modulate the depth of the two wells at some frequency f_{well}, with the two wells being 180° out of phase. Let this periodic tilting of the system be small in comparison to the barrier height between the wells. The particle also has some thermal energy that will cause it to hop between the two wells with average time between hopping of T_K. The tilting alone is not enough to cause the particle to hop between the wells, but the thermal noise-induced hopping can become synchronized with the tilting. This synchronization will occur when the thermal hopping time is half of f_{well}, or

$$2T_K = 1/f_{well} \tag{3.1}$$

When the thermal hopping occurs at half the well tilting period, then (statistically) each time the well tilts, the particle hops over the barrier due to its thermal energy and reaches the lowest energy state. In this way, the thermal energy causes a resonance between the well tilt and particle position.

For our system, this picture still holds, with the double-well being the energies of two vortex configurations and the energy barrier separating the two configurations preventing the vortices from moving between the two configurations. The tip oscillation is the small tilt given to the potential well, as it will lower the energy of one configuration relative to the other as it swings back and forth, and thermal energy plays the role of the noise. At points of energy degeneracy between two vortex configurations, the tip oscillations will change the energies so that one configuration has slightly lower energy than the other. If the thermal energy of the vortices is sufficient, they can overcome the barrier and enter the lowest energy state. As the cantilever swings back, the first configuration will be lower in energy again due to the potential well moving, and the vortices will thermally hop back to their original configuration. If this happens roughly in sync with the cantilever oscillation, the cantilever frequency will change. For this to occur, the temperature of the system must be high enough so that the vortices can reliably hop between configurations.

For the images shown in Fig. 3.4, the temperature is relatively high, being 3.7 K and just below T_c. In Fig. 3.6, as we begin to lower the temperature, the stochastic resonance remains at the highest temperatures

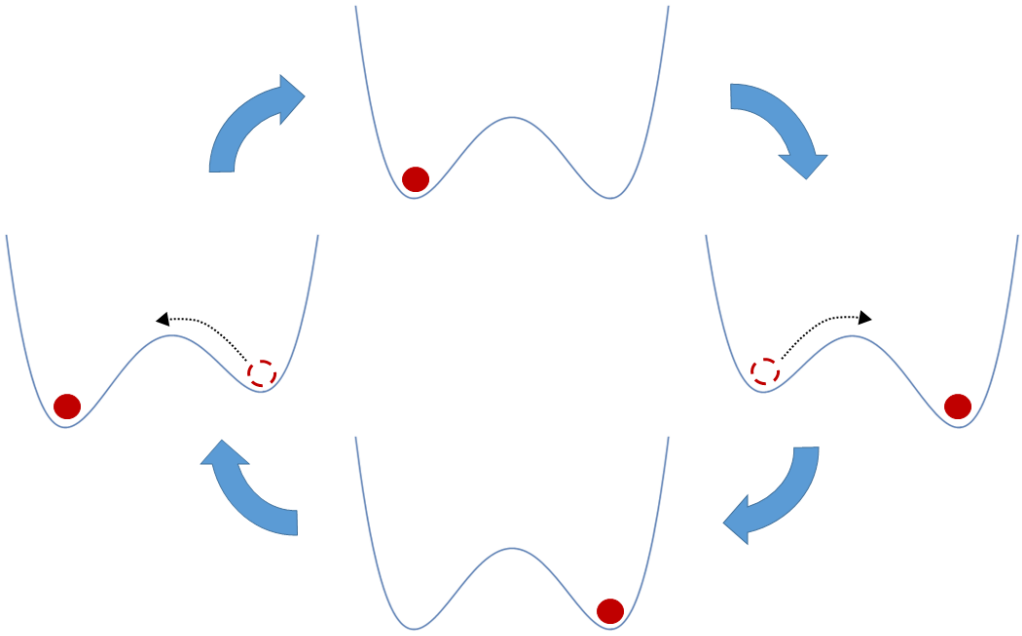

Figure 3.5: Illustration of stochastic resonance in a doublewell potential. Two wells start with equal energies, and are then tilted periodically. The tilt is not sufficient to move a particle from one well to the other alone. A particle with sufficient thermal energy is able to overcome the barrier and lower its total energy. If the thermal motion of the particle causes it to change wells every time another well becomes a lower energy, the two frequencies are in resonance.

shown. Then, at moderately lower temperatures, the images start to display random frequency jumps from vortices moving out-of-sync with the cantilever as the temperature is decreased. Decreasing the temperature further results in the loss of a pattern, with only noise being visible. This effect is what we expect if stochastic resonance effects are responsible for the frequency changes.

3.3 Identification of Island Locations

To interpret the patterns that are found in the images, we need to identify the locations of the islands relative to the patterns. Identification of the island locations is done by first imaging the surface well above the superconducting transition temperature, T_c. Above T_c, the frequency shift of the cantilever is primarily due to topographic and material changes on the surface. By scanning above the superconducting transitions, we identify the locations of the islands in the scan range. We then step the temperature down and scan the surface repeatedly, moving the tip to stay at an appropriate distance from the surface to obtain a reasonable imaging resolution without collision with the surface. By tracking the motion of the various features of the surface and how they change, we can reliably locate the island locations below T_c, where the topographic frequency shifts are obscured by other shifts due to superconducting effects. Fig. 3.7 shows a series of scans beginning at 7.0 K, and decreasing temperature in 0.5 K steps (**b** through **f**). In Fig. 3.7g and h, the system is below T_c, with a field having been applied in h. The island locations in the topographic image are slightly offset from the symmetry points of the vortex pattern. This is due to an offset between the location of the physical tip center and the maximum magnetic field generated by the tip.

3.4 Varying patterns with an external field

3.4.1 Scans with external field antiparallel to tip field

Patterns are due to vortices changing their configuration in a potential well generated by the magnetic tip. The depth of the potential well that the vortices occupy can be modified by changing the external field applied to the surface. The magnetic field that we apply is oriented anti-parallel to the field from the tip (referred to as positive fields in this thesis), meaning the well depth will decrease for increasing external fields. The shallower potential well and the lesser flux penetrating the surface associated with it, will give rise to fewer vortices on the surface that can move and generate the observed patterns.

Fig. 3.8 shows a progression of the vortex patterns seen on the surface as the external field is increased from 0 Oe to 125 Oe. At zero field, no symmetric pattern is observed, as seen in Fig. 3.8a. Fig. 3.8b shows

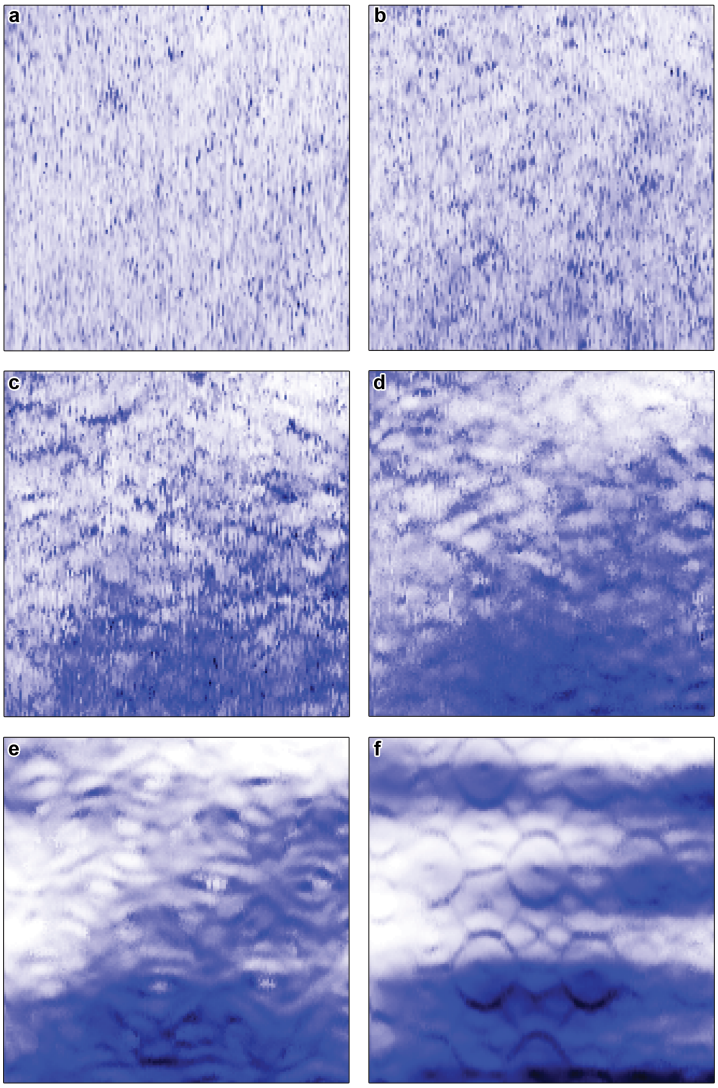

Figure 3.6: Images showing the effects of temperature on the stochastic resonance effect. At low temperatures, such as in (**a**): 2.0 K, (**b**): 2.6 K, and (**c**): 3.0 K, the frequency is noisy, and no resonance is seen. In (**d**): 3.2 K, the frequency begins to settle. At higher temperatures, such as (**e**): 3.4 K and (**f**): 3.6 K, stochastic resonance allows mapping of the energy degeneracies of vortex configurations. Images **a-e** taken approximately 400 nm from the surface, (**f**) taken 300 nm from surface. All images in an external field of 83 Oe. No background subtraction applied to these images.

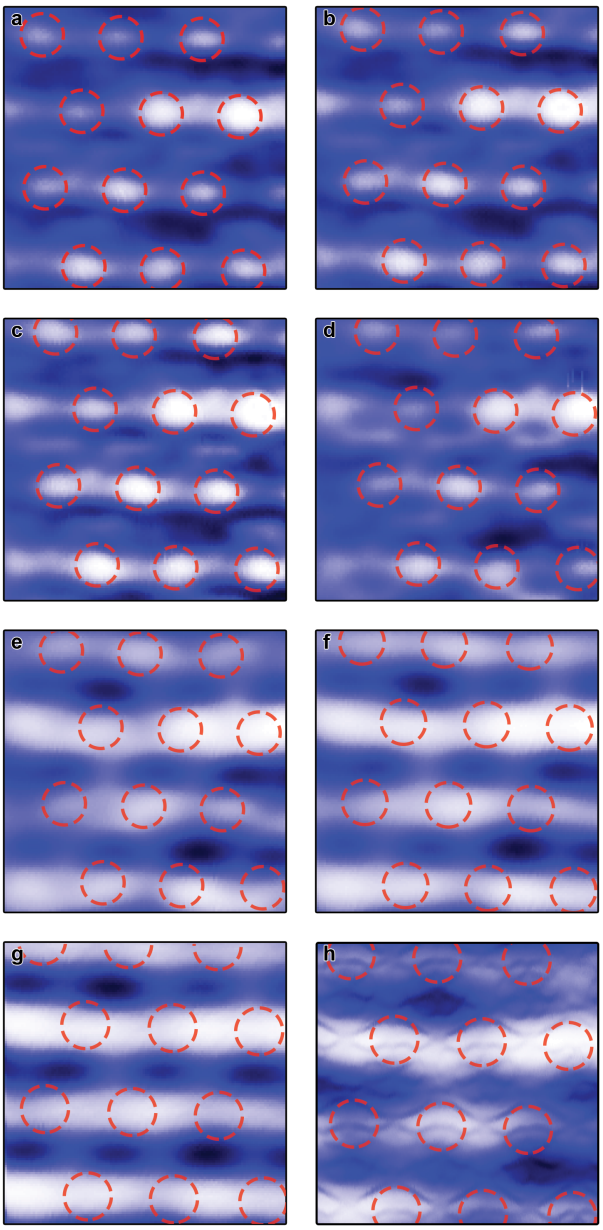

Figure 3.7: Determining island locations below T_c. Island locations are determined by a frequency image above T_c, then the temperature is slowly lowered. Starting from 7.0 K in (**a**), temperature is lowered in 0.5 K increments (**b** - **f**). (**g**): Below T_c at 3.7 K. Upon applying a field (**h**), the island locations can be seen in relation to the pattern. As can be seen, the topographic pattern and magnetic pattern have an offset due to an offset between the location of the tip center and the position of the maximum magnetic field.

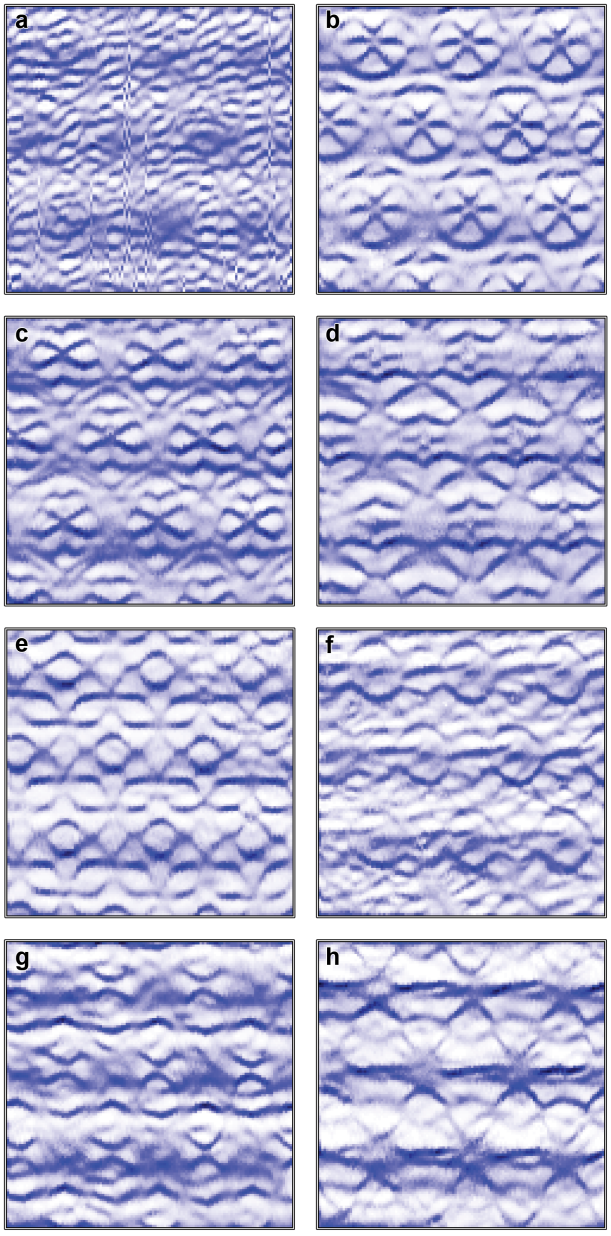

Figure 3.8: Imaging with increasing field, showing the patterns from different vortex numbers trapped underneath the cantilever tip. (**a**) 0 Oe. (**b**) 50 Oe. (**c**) 60 Oe. (**d**) 70 Oe. (**e**) 80 Oe. (**f**) 90 Oe. (**g**) 110 Oe. (**h**) 125 Oe. All images are taken at 3.70 K and 350 nm scan height.

the pattern from what we find to be 9 vortices underneath the tip at 50 Oe, as will be explained in the next chapter. Fig. 3.8c-f shows the progression of the pattern with magnetic field increasing in 10 Oe steps, with the vortex configuration losing one vortex on each step. The final two images use larger steps in field, and show 4 and 3 vortices (3.8g-h) at 110 and 125 Oe. As can be seen, many vortex patterns are visible by varying the field and keeping the scan height constant.

Fig. 3.9 shows another set of scans with increasing fields above one filling and closer to the surface. Above one filling, the vortices being considered may be non-circulating plaquettes on a background of anti-vortices, since there is an additional (negative) flux quantum penetrating each plaquette. Different patterns are present in these images, showing the large number of vortex configuration spaces that can be imaged with this method. It can also be seen that patterns that are shared between the two fillings show different strengths for some lines, which may be a result of the different, but related, situations.

3.4.2 Scans with external field parallel to tip

If the external magnetic field applied to the surface is in the same direction as the field from the tip (referred to as negative fields), the patterns seen with anti-parallel fields do not appear. In this case, there are a large number of vortices present in the system that all crowd towards the tip, leading to a large number of vortices trapped underneath the tip. These vortices can then change configuration often, and probe a large configuration space, so there may not be a stochastic resonance effect from their motion owing to the large number of possible configurations. As seen in Fig. 3.10, at negative fields (a-f) no patterns can be seen in the image. This set of images span -10 Oe (Fig. 3.10a) to -110 Oe (3.10f) in -20 Oe steps. The last two images in the figure (Fig. 3.10g-h, taken at +85 Oe and +105 Oe, respectively) show the effects at roughly the same positive fields at the same tip height, displaying patterns that are very prominent. This illustrates the lack of resonance lines when the magnetic field is oriented in the same direction as the field from the tip.

3.4.3 Pattern repetition at f+1

As noted in the introduction, the filling or frustration of the system is given by $f = \Phi/\Phi_0$. At filling fractions above 1, one anti-vortex is present in each site. A portion $f - 1$ of the plaquettes lack this anti-vortex, and the non-vortex plaquettes can move to minimize energy much like the vortices. This implies that at fillings of f and $f + 1$, the same pattern should be present, since the same number of excitations are mobile in both cases.

In our experiment, this is exactly the behavior that is seen. Fig. 3.11 shows a number of patterns, and the same pattern at one additional filling. As can be seen, when the field is increased by approximately

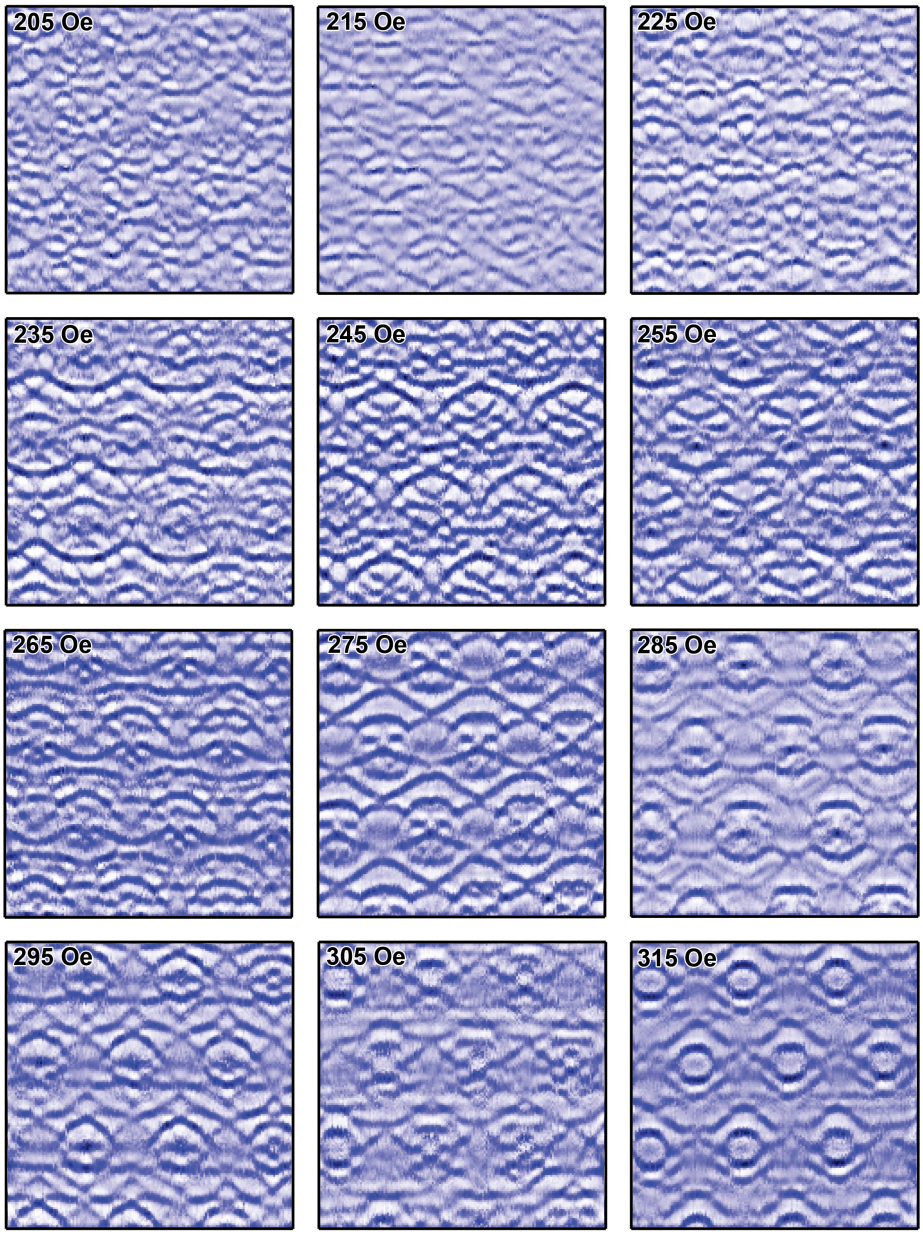

Figure 3.9: Another field ramp done at 3.60 K at higher fields, with a tip scanning height of 300 nm. All images are taken above $f = 1$, with the fields listed in the corner of each image. Many different patterns are seen at different fields and tip heights.

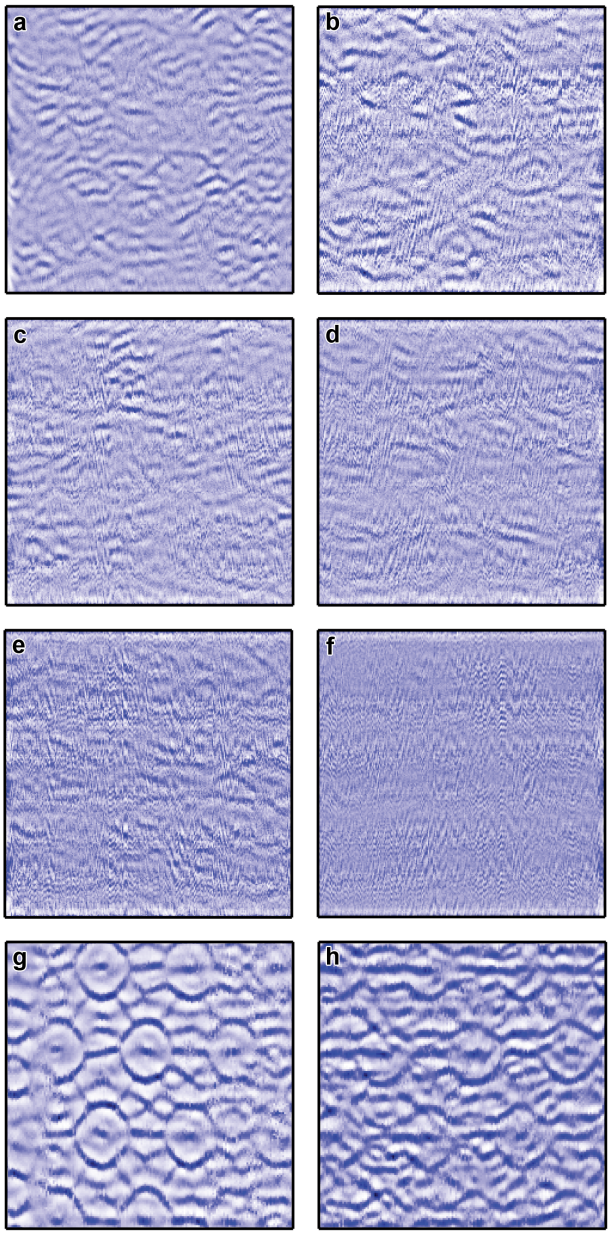

Figure 3.10: (**a**-**f**) Patterns are not present in fields parallel to the tip (negative fields), as can be seen in these images. Scans start at -10 Oe in (**a**) and increment by -20 Oe until -110 Oe is reached in (**f**). (**g**-**h**) At comparable positive fields at the same height patterns are prominent and easily seen. (**g**) is taken at +85 Oe. (**h**) is taken at +105 Oe. Negative field images are taken at 3.70 K, while the positive field images are taken at 3.60 K. All images are taken at a tip height of 300 nm, and are the same size.

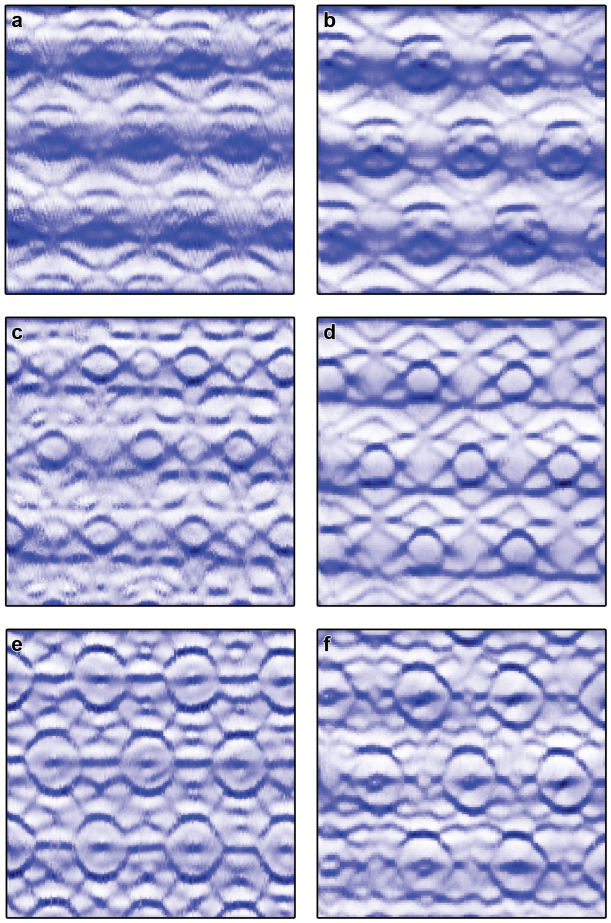

Figure 3.11: Repeating patterns with one additional filling. Patterns that are seen at a given filling ($f = 0.43$ / B = 83 Oe here) in **a**, **c**, and **e**, are also seen at $f + 1$ ($f + 1 = 1.42$ / B = 272 Oe) in **b**, **d**, and **f**. Some minor differences can be seen, and may be due to differences between motion of the excitations.

$f = 1$ (B = 191 Oe for the arrays spaced by 50 nm center-to-center), the patterns repeat. It can be seen that some differences exist between the figures for different fillings, in the form of bolder or thinner lines and extra or missing features. We believe this to be due to differences in the well depths and energies of the different configurations because of the presence or absence of the "bed" of vortices. The majority of the features are present in both images, showing that the configurations of the vortices or non-circulating plaquettes are essentially the same.

3.5 Varying patterns with tip-surface separation

Like varying the external field, changing the tip-surface separation changes the depth of the potential well. Changes in the tip-surface height also modify the width of the well, as the field from the tip will give negative

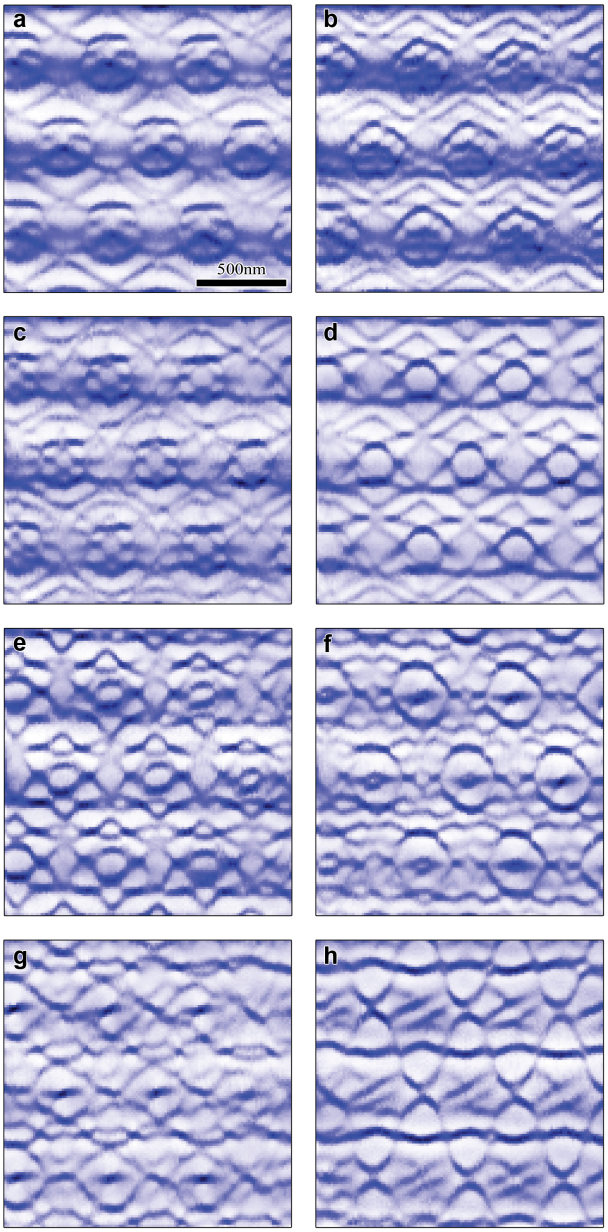

Figure 3.12: Patterns generated as the tip is pulled back from the surface. Patterns start 150 nm from the surface, with distance increasing by 20 nm for each image. External field is 272 Oe, and temperature is 3.70 K for all images. (**a**) 7 vortices underneath the tip. (**b-c**) 6-7 vortex transitions. (**d-e**) 6 vortices. (**f**) 5 vortices. (**g**) 4-5 vortex transition. (**h**) 4 vortices underneath the tip. Scale bar shown on first image only, scales are the same on all images.

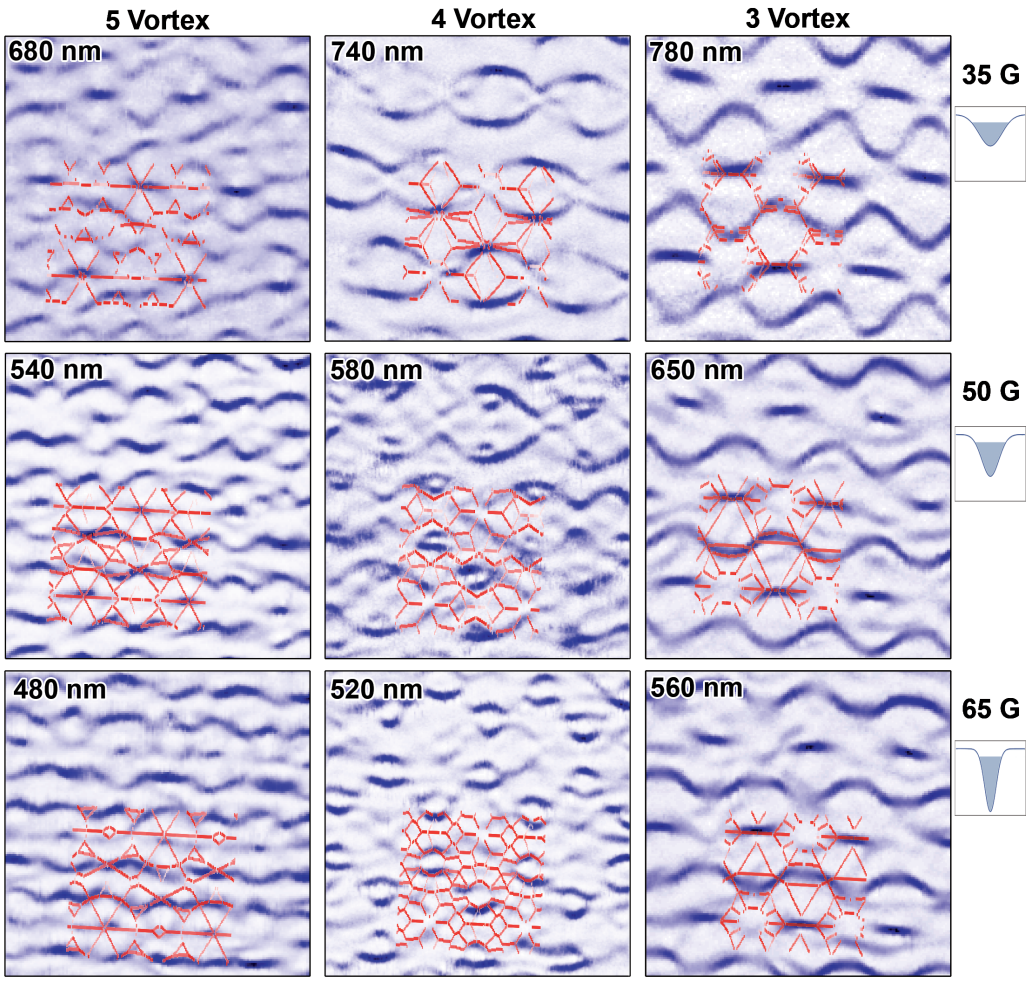

Figure 3.13: Vortex patterns with varying tip scanning height. The patterns for 3 vortices (right) are relatively stable as the tip height is increased. 4 vortex patterns (center) show some regions close up and disappear for larger tip-surface separations, showing that the vortex configurations in those areas are not stable at larger heights. The 5 vortex patterns (left) show similar behavior as the 3 vortex, with some lines becoming less prominent while the pattern remains similar. Images are shown for three external field values, at left, with diagrams illustrating the relative width/height of the potential well in each row.

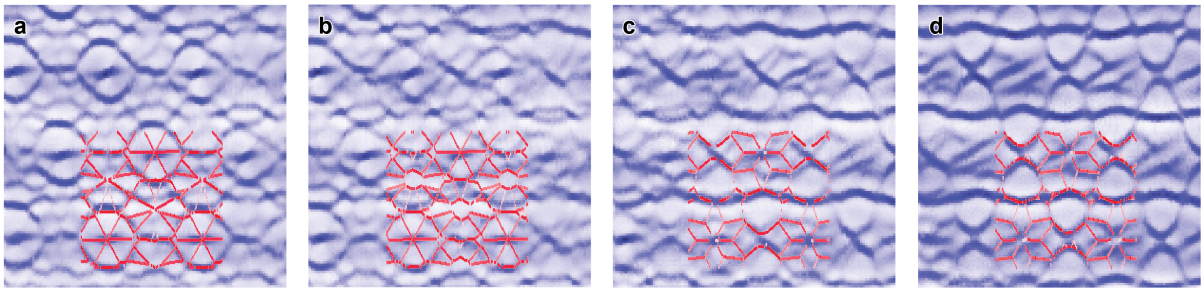

Figure 3.14: Patterns as the number of vortices beneath the tip transitions between five and four. In (**a**), there are five vortices underneath the tip at most locations in the scan. As the tip is moved back in 10 nm increments (**b-d**), regions where four vortices is more energetically favorable open up (hourglass patterns) and eventually dominate the image. Images taken on a 500 nm spaced lattice, with temperature of 3.70 K and an external field of 248 Oe. Red lines are simulated vortex transition locations for this transition.

vortex energies for an area that is larger or smaller. Figs. 3.12 and 3.13 shows the effect on the pattern as the tip-surface separation is increased. Fig. 3.12 shows vortex patterns when the tip is scanned at 272 Oe, for distances of 150-290 nm. The number of vortices (or non-anti-vortex plaquettes) underneath the tip changes from 7 to 4 over this distance. In Fig. 3.13, 3, 4, and 5 vortex patterns are shown for different tip-surface separations at fields of 35, 50, and 65 Oe. The three vortex patterns (right) are relatively stable regardless of tip height, while the four vortex patterns (center) show some regions shrink and disappear. In these regions, vortex configurations that are stable at lower heights are no longer the minimum energy state due to the tip height. At higher tip heights, the field from the tip is weaker, and so the field-vortex energy becomes less important than the vortex-vortex interactions as the tip height is increased. The patterns for five vortices (left) show similar progression to those of the three vortex patterns.

While the vortex pattern can change abruptly while the tip height is changed, it can also change gradually, with regions containing a different number of vortices underneath the tip opening up and slowly becoming dominant in the image. Fig. 3.14 shows this effect for a transition between five vortices and four vortices. On the left, the pattern is primarily one with five vortices underneath the tip. As the tip is moved back in 10 nm increments, circular regions appear that contain four vortices. These regions expand, and other four vortex regions enter, until the full scan contains only four vortices underneath the tip at all points. On these images, a red outline of the simulated transition positions has been added, as will be described in Chap. 4. Similar transitional images have been observed for many different tip height and field combinations.

Since we can modify the vortex patterns by changing both the external field and tip-surface separation, we can create a "phase-diagram" of sorts that reflects the patterns that are seen as a function of both field and tip height. In Fig. 3.15, a simple diagram has been made for an array with 500 nm center-to-center spacing. Each pattern that was shown above corresponds to a particular number of vortices trapped

underneath the tip. By extracting this number through the simulations that will be described in the next chapter, we can find regions where a particular number of vortices is stable underneath the cantilever for one particular magnetic tip. Though the figure displays sharp changes between vortex numbers, the transition between two differently numbered regions can be broad, as shown in Fig. 3.14. In these regions, different vortex numbers are present at different locations in the images. These transition regions are not displayed here for clarity. We can also use this diagram to track vortex pattern changes as they slowly change due to the well depth and/or width changing, allowing assignment of vortex numbers to all relevant patterns. Matching the simulations to reflect similar diagrams aids in extraction of relevant parameters, as will be described in the next chapter.

3.6 Changes with lattice spacing

Changing the lattice spacing of the array has a number of effects on the system. First, the transition temperature, T_c, of the array is dependent on lattice spacing, as discussed in Chap. 1. This change in T_c affects the temperatures that the stochastic resonance effect is seen at. The change in T_c is due to a change in the Josephson coupling between the islands, which affects the vortex-vortex interactions present in the system, making them stronger if the lattice size is decreased and vice versa. The magnetic field required to add one vortex to the system also changes with lattice spacing. For the 500 nm array, which data was shown for above, the magnetic field required to generate a vortex at every site is 191 Oe. For a spacing of 440 nm, this increases to 247 Oe, while the 560 nm spaced array requires 152 Oe.

These effects change the vortex patterns seen for a given external field and height. As seen in Fig. 3.16, changing the lattice spacing by 12% can change where the patterns appear in field and height. In this figure, each column is a different lattice spacing, where all images are taken with a set external field. Each row shows the pattern generated by a different vortex number at a scan height shown in the corner of each image. The four vortex patterns show a change in the appearance of the patterns, with the pattern shifting like that of Fig. 3.13 despite the scan height decreasing to the left. This is due to the changing lattice spacing and associated effects referenced above. The six vortex pattern (3^{rd} row) also shows some regions shrinking as the lattice spacing is decreased. The five and seven vortex patterns (2^{nd} and last rows, respectively) do not show significant changes with lattice spacings. As seen, the 440 nm array generally shows patterns and features similar to those of the 500 nm array, but these patterns occur closer to the surface and at higher fields, owing to the higher magnetic field needed to generate vortices in the system. The 560 nm array displays the opposite effects, as expected.

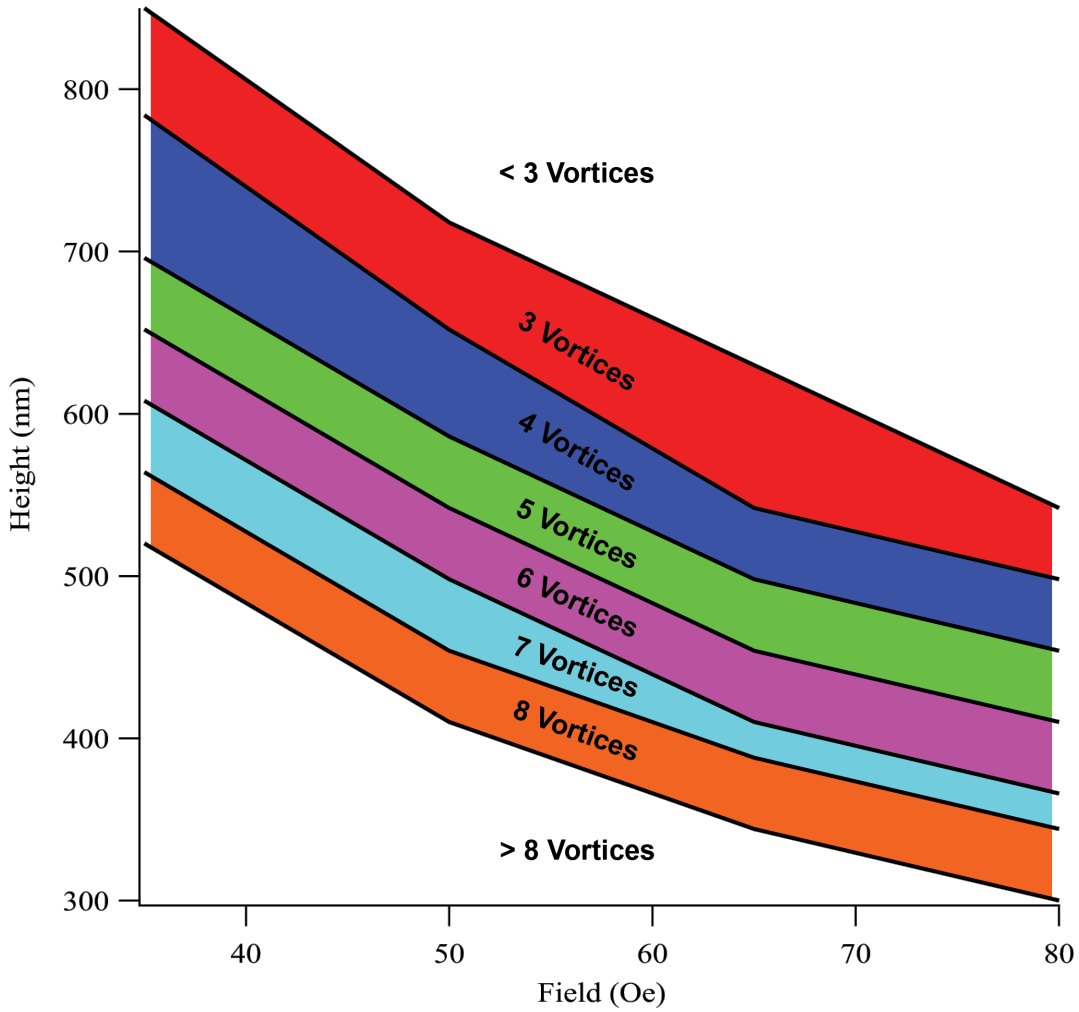

Figure 3.15: Number of vortices trapped underneath a magnetic tip for islands spaced by 500 nm center-to-center. Shaded regions denote the regions where a given number of vortices will be found underneath the magnetic tip. The number of vortices can be modified by both the height of the tip and the external field. This "phase diagram" is dependent on the tip used in the given experiment.

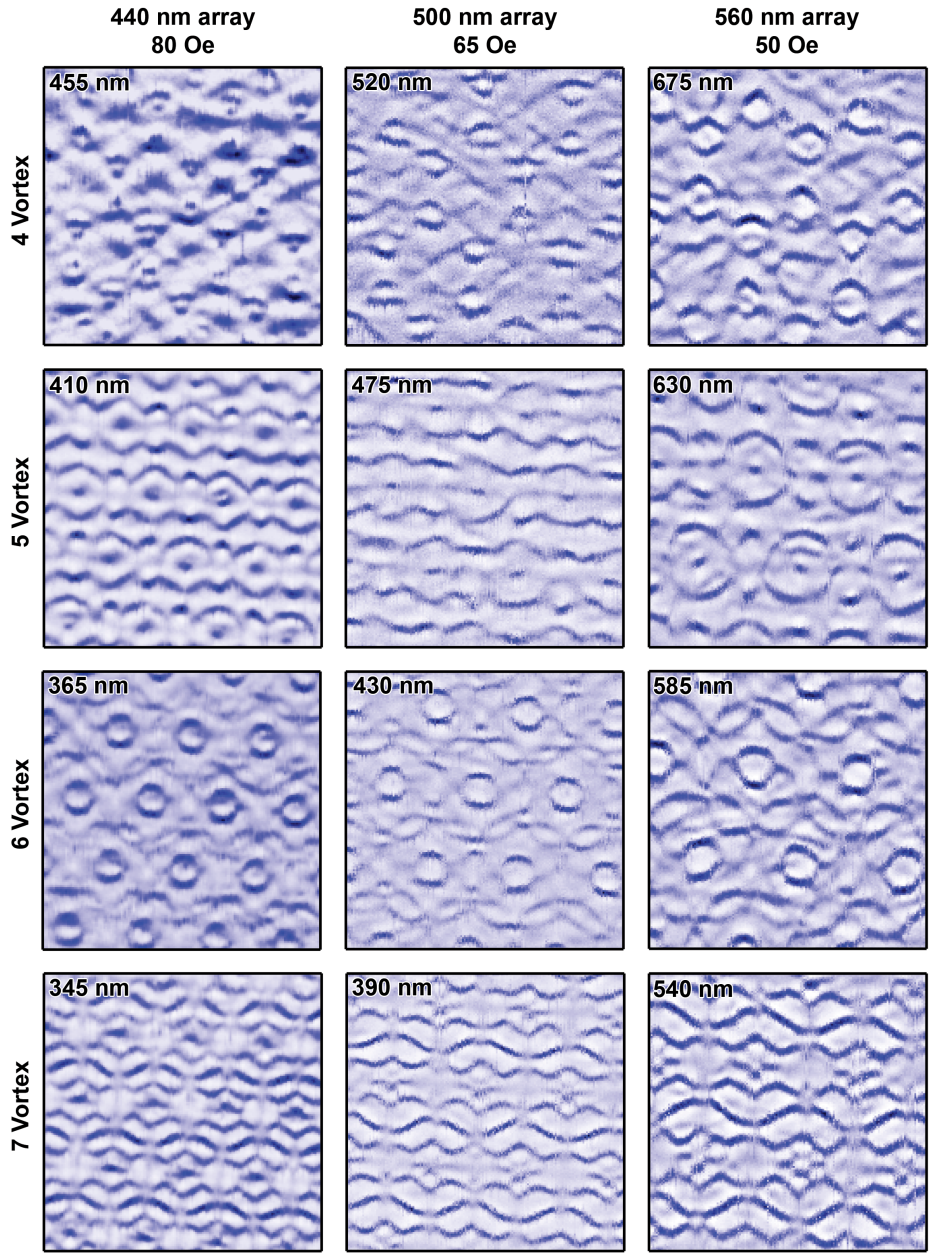

Figure 3.16: Patterns for three different lattice spacings with equal vortex number underneath the tip. The external field for each lattice spacing was kept constant and tip-surface separation varied. Tip-surface separations are listed in the corner of each image. For the four vortex patterns (top row), changes to the pattern can be seen as the spacing and heights are changed. The six vortex patterns (3rd row) also show some regions shrinking. These effects occur even though the tip is closer to the surface for the tighter lattice spacings. The five vortex (2nd row) and seven vortex (last row) do not show much dependence on height. 440 nm images were taken at 7.70 K, 500 nm images at 5.70 K, and 560 nm images at 3.85 K. Image size is 1.6×1.6 μm^2 for all images.

We have shown many different patterns generated by a small number of vortices moving underneath a magnetic tip attached to a cantilever. These patterns range from simple to complicated, though all reflect the symmetry of the lattice containing them. In the next chapter, we will explain how we determine the number of vortices trapped under the tip, and the simulations used to extract the relative energy scales of the system.

Chapter 4

Simulations

4.1 Overview of Monte Carlo Simulations

Monte Carlo methods are techniques for simulating various phenomena using randomly generated numbers. The technique was named by Ulam and von Neumann, who solved neutron diffraction problems using the technique in the 1940's [108]. The technique is widely used in scientific fields due to its ability to approximately determine quantities without needing an exact analytical form.

In our case, we chose to use a Metropolis Monte Carlo method to determine the vortex configuration corresponding to the lowest energy state due to the large number of configurations that were possible in the simulations. We generally used a simulated lattice with 85 plaquettes, so for a given number of vortices, n, there are $\binom{85}{n}$ possible vortex configurations, too many to calculate energy for quickly. Since the minimum energy state for neighboring tip positions should only have small changes in the vortex configurations, such as one or two vortices changing positions, utilizing the Monte Carlo method described below allows quick determination of the lowest energy configuration. We can also easily change the parameters of the simulations and re-run them with differing fields, tip heights, etc.

In this chapter, we will derive an approximate energy form for the system that allows quick determination of the energy of a vortex configuration. We then explain how we use this formula to do simulated annealing of the system to determine the lowest energy vortex configuration for a given number of vortices. These states are then used in a minimization procedure that allows us to extract the relative energy scales of the interactions present in the system.

4.2 Other simulation methods used on JJAs

Other methods that have been used to simulate Josephson junction array systems include the RCSJ model and molecular vortex simulations. In the RCSJ (resistively and capacitively shunted junction) model, a Josephson junction is modeled as an ideal Josephson junction in parallel with a resistor and a capacitor [33].

The resistor adds dissipation when finite voltages are added across the system, while the capacitance models the shunting capacitance between the two electrodes in the junction. Using this model, the motion of single vortices at different frustrations, f, have been modeled [109].

In molecular vortex simulations, a portion of the superconductor is modeled with vortices present. Pinning centers are added, and a driving force is applied to the vortices. The vortices will follow paths given by the forces acting on them, and measurable quantities such as the voltage are simulated based on the vortex motion. This model can be used to determine where the vortices will flow, as well as the phase of the system by studying the vortex motion [110,111]. A molecular vortex simulation of our system has been partially constructed by Taylor Hughes' group[1]. These simulations showed similar minimum energy plots to the simulated annealing we discuss in this chapter. Use of these simulations may be interesting to compare to our simulated annealing results in the future.

4.3 Bilinear Form

A JJA has free energy given by [33,48]

$$F = E_J \sum_{<i,j>} 1 - \cos\left(\phi_i - \phi_j - \frac{2\pi}{\Phi_0} A_{ij}\right) \tag{4.1}$$

where $E_J = \frac{\hbar I_c}{2e}$ is the Josephson energy, Φ_0 the flux quantum, A_{ij} is the vector potential between islands i and j, and $< i, j >$ denotes a sum over all pairs of islands. Assigning $\gamma_i = \phi_i - \phi_j - \frac{2\pi}{\Phi_0} A_{ij}$ as the gauge-invariant phase of link from i to j and approximating the cosine, the energy of the array is approximately

$$F = E_J \sum_{<i,j>} \frac{\gamma_{ij}^2}{2} \tag{4.2}$$

To determine γ_{ij} for each link, and therefore the energy, we first note that the phase on each island must be single-valued, resulting in the condition

$$\sum_{plaquette} \gamma_{ij} = 2\pi \left(f_i - n_i\right) \tag{4.3}$$

where $f_i = \frac{\Phi}{\Phi_0}$ is the frustration of plaquette i, and n_i is the integer vorticity of the plaquette. Additionally, recalling that the Josephson current is given by $I = I_c \sin\gamma_{ij}$, we again take γ_{ij} to be small, and

[1] Victor Chua and Ian Mondragon-Shem created these simulations

let

$$I = I_c \gamma_{ij} \tag{4.4}$$

Applying Kirchoff's current law, the total current entering and leaving an island must be zero to keep the phase constant. Since we have linearized the current in terms of γ_{ij}, we then have

$$\sum_{\substack{j=\text{nearest} \\ \text{neighbors of } i}} \gamma_{ij} = 0 \tag{4.5}$$

With these equations, we are now ready to begin building our model of the JJA. We start by assuming that all vortices will sit at the center of each plaquette. We also note that, from the above, the energy is only dependent on the number of vortices in each plaquette (n_i) as well as the frustration of each plaquette (f_i). The flux through each plaquette will be determined by the sum of the external field with the field generated by the magnetic tip. As mentioned in the introduction, self-inductance effects are usually negligible for SNS arrays, and so will be ignored. We also note that with the replacement of γ_{ij} in Eqs. 4.3 and 4.5 by I_{ij}, the equations become those for a superconducting wire network, up to a constant dependent on the wire parameters.

We now rewrite the equations for γ_{ij} in matrix form, and absorb constants into a constant a. With this replacement, 4.3 and 4.5 become

$$a \sum_k \gamma_k = f_i - n_i \tag{4.6}$$

$$\sum_{\substack{k \text{ links around} \\ \text{the } l^{th} \text{ node}}} \gamma_k = 0 \tag{4.7}$$

where in the first equation we sum the k links surrounding plaquette i, and in the second we sum the k links touching node l. We consider a finite portion of the hexagonal lattice that contains N plaquettes, N_{nodes} islands (nodes), and N_{links} links between nodes. $N_{links} = N + N_{nodes} - 1$ in this area. There will be N independent equations like 4.6, and $N_{node} - 1$ independent equations like 4.7. Putting these into matrix form:

$$a\begin{pmatrix} 1 & 1 & 1 & 0 & \cdots \\ 0 & 1 & -1 & 1 & \cdots \\ \vdots & \vdots & \vdots & \vdots & \ddots \end{pmatrix}_{[N,N_{links}]} \begin{pmatrix} \gamma_1 \\ \gamma_2 \\ \vdots \\ \gamma_{N_{links}} \end{pmatrix} = \hat{P}_{[N,N_{links}]}\vec{\gamma} = \vec{f} - \vec{n} \tag{4.8}$$

$$\begin{pmatrix} 1 & -1 & 1 & \cdots \\ 0 & 0 & -1 & \cdots \\ \vdots & \vdots & \vdots & \ddots \end{pmatrix}_{[N_{node}-1,N_{links}]} \begin{pmatrix} \gamma_1 \\ \gamma_2 \\ \vdots \\ \gamma_{N_{links}} \end{pmatrix} = \hat{Q}_{[N_{nodes}-1,N_{links}]}\vec{\gamma} = 0 \tag{4.9}$$

Combining these equations into a single matrix, $\hat{M}$:

$$a\hat{M}\vec{\gamma} = a\begin{pmatrix} \hat{P} \\ \hat{Q} \end{pmatrix}_{[N_{links},N_{links}]} \begin{pmatrix} \gamma_1 \\ \gamma_2 \\ \vdots \\ \gamma_{N_{links}} \end{pmatrix} = \begin{pmatrix} (f_1 - n_1) \\ \vdots \\ (f_N - n_N) \\ 0 \\ \vdots \end{pmatrix}_{[N_{links},1]} \tag{4.10}$$

We can now invert this matrix to solve for the phases, $\vec{\gamma}$.

$$\vec{\gamma} = a^{-1}\hat{M}\begin{pmatrix} (f_1 - n_1) \\ \vdots \\ (f_N - n_N) \\ 0 \\ \vdots \end{pmatrix} \tag{4.11}$$

Combining this with 4.2 gives the energy of the system:

$$\begin{aligned} F &= \left(\vec{f} - \vec{n}\right)^T \hat{B}^T\hat{B}\left(\vec{f} - \vec{n}\right) \\ &= \vec{f}^{\,T}\hat{B}^T\hat{B}\vec{f} - 2\vec{f}^{\,T}\hat{B}^T\hat{B}\vec{n} + \vec{n}^T\hat{B}^T\hat{B}\vec{n} \end{aligned} \tag{4.12}$$

where $\hat{B}$ is the first N columns of M^{-1}, and a absorbed other constants and was set to one, since its only effect is to scale the total energy of the system. If we now make the assignments $F_0(\vec{f}) = \vec{f}\hat{B}^T\hat{B}\vec{f}$, $\hat{U(\vec{f}} = 2\vec{f}^T\hat{B}^T\hat{B}$, and $\hat{V} = \hat{B}^T\hat{B}$, we find

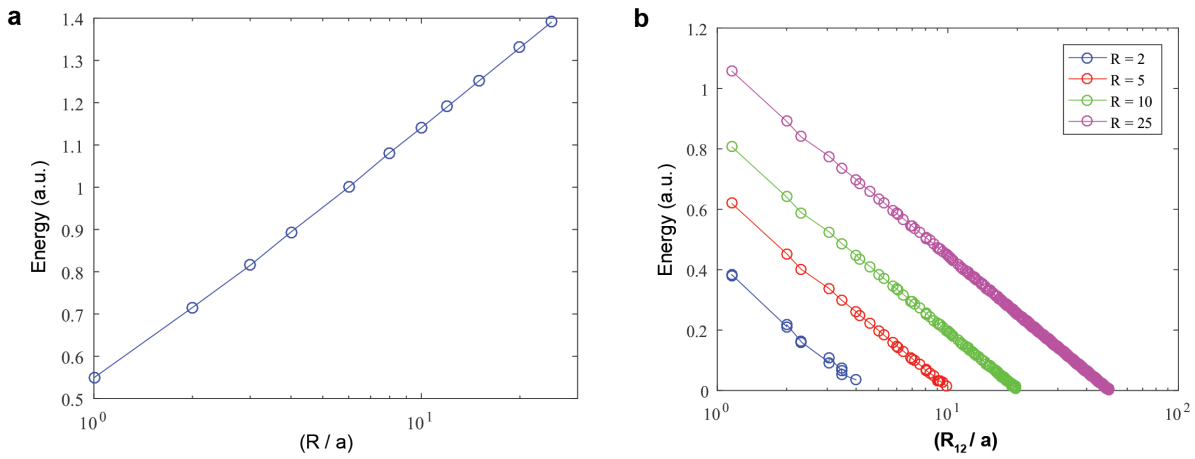

Figure 4.1: Energy scaling of the linearized vortex interactions. (**a**) Vortex energies as a function of system size, showing a roughly logarithmic relationship. This corresponds well to the scaling of rectangular JJAs, which also scale as $\ln(R/a)$. (**b**) Vortex-vortex energies as a function of distance for different system sizes (R is the system radius). The energy is for two vortices of the same sign, and also shows roughly logarithmic dependence on the distance in agreement with JJAs.

$$F = F_0(\vec{f}) + \hat{U}(\vec{f})\vec{n} + \vec{n}^T\hat{V}\vec{n} \tag{4.13}$$

Assuming that the flux through each plaquette is known, and we only change the vorticity of the plaquettes, we find the free energy to be

$$F = F_0 + \sum_{i=1}^{N} U_i n_i + \sum_{i,j=1}^{N} V_{ij} n_i n_j \tag{4.14}$$

This linearized energy can now be minimized via a simulated annealing procedure by changing the vortex configurations contained in the winding numbers, n_i. The linearized energy is not exact for the Josephson Junction array, but will be shown to give good agreement with many of the patterns seen. Additionally, if we look at the matrix $\hat{V}$, we can see that diagonal elements correspond to vortex self-energies, while off-diagonal elements are vortex-vortex interactions. Plotting V_{ii} as a function of the simulated system radius, R, (see Fig. 4.1a) shows logarithmic behavior, where the on-site energy scales as $F \propto \ln(R/a)$, where a is the lattice spacing. This proportionality is the same as that for JJAs, as shown in Eq. 1.17. V_{ij}, the vortex-vortex interactions, should scale as $F \propto \ln(R_{12}/a)$ for JJAs (Eq. 1.18), where R_{12} is the distance between two vortices. For our expression, the same proportionality holds, as seen in Fig. 4.1b.

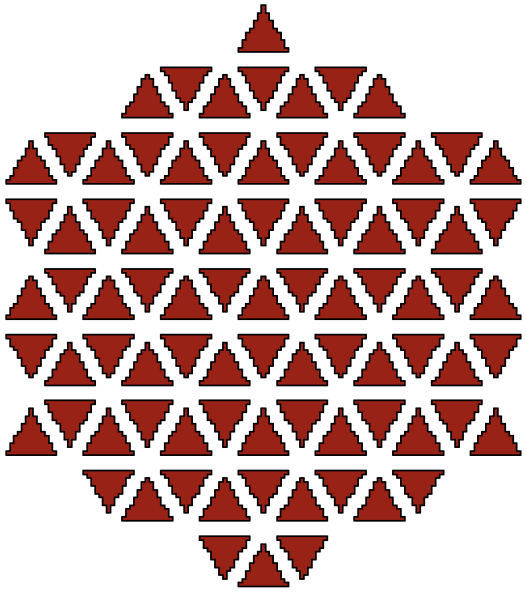

Figure 4.2: Shape of the 85 plaquette array used in the simulated annealing calculations. Energies used for each array position are from an array of several thousand plaquettes.

4.4 Simulated Annealing

With the set of equations from the previous section, we now focus on the energy minimization procedure. As discussed previously, a large number of possible vortex configurations exist for a given number of vortices. We will use a Metropolis type Monte Carlo simulation to minimize the energy for a set number of vortices underneath the tip. Starting with the equations above, we generate equations for the energies of vortices sitting in a triangular grid of 85 plaquettes, as shown in Fig. 4.2. To minimize issues from vortex energies being too low due to the radius of the array being smaller, we use the energies for the 85 plaquettes as calculated for an array of several thousand plaquettes, i.e. we calculate the energies for a large array and consider only the center 85 plaquettes.

Inputting the external field and field profile from the tip at a given tip location, along with the lattice spacing allows calculation of the flux in each plaquette. Flux values that are negative (field antiparallel to tip) are truncated at 0 to remove negative vortices. This procedure is implemented to keep the number of vortices positive, as well as make the simulation more stable. With "negative" vortices present, the simulated results are often very noisy, due to vortices near the edges of the simulated area having nearly degenerate energies in a number of positions. This causes the simulated annealing to land randomly on a number of approximately equal energy states with differing configurations, even when the configuration of

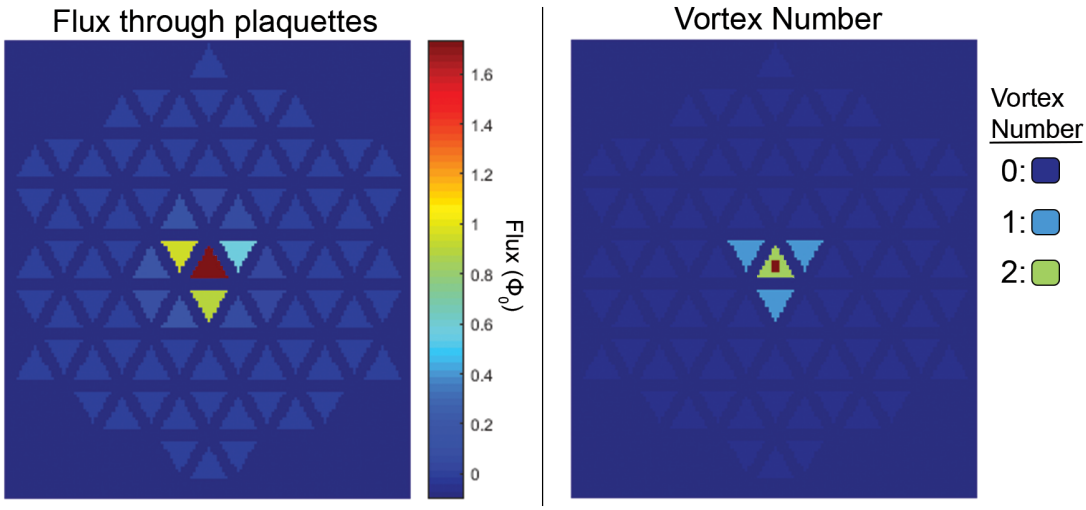

Figure 4.3: Flux calculation leading to an initial vortex configuration. Flux values for each plaquette in units of Φ_0 are initially found, as seen in the left figure. The flux values are rounded to give the vortex configuration seen at right. **Right** Colors indicate the number of vortices in each plaquette. The red dot indicated the position of the tip above the array. If additional vortices are needed to equal the total flux through the system, a new vortex will be added to the plaquette with the most remaining flux after adjusting for the already-placed vortices.

positive vortices near the tip are stable. We make this approximation for this reason, and also due to the fact that the patterns seem to be primarily caused by the small number of positive vortices near the center.

With negative flux values truncated, we then round the values of flux to the nearest flux quantum in each plaquette to get a starting vortex configuration, as seen in Fig. 4.3. We also sum the total number of flux quanta in the array and add (subtract) vortices from the plaquette(s) with the most (least) remaining flux so that the number of vortices we have in the array is equal to the number of flux quanta passing through the array. Starting from this initial configuration of vortices, the energy of the vortex configuration is calculated, and the simulated annealing process begins.

To minimize the energy of the array, a pair of plaquettes in the array are chosen at random, as seen in Fig. 4.4. We add a vortex to one of the plaquettes, and an anti-vortex to the other. The energy of this new configuration is then calculated. If the new vortex configuration has lower energy, we accept that as the new state and repeat the procedure. If the energy is higher than the old state, the new state is accepted if it satisfies $\exp(-(E_{new} - E_{old})/T) >$ rand, where rand is a random number between 0 and 1, and T is the annealing temperature, which is slowly lowered while the simulation runs. The simulation is run at least $2 \times (N_{plaquettes})^2$ times so that each pair of plaquettes is chosen during a run, on average. If a new state is accepted, the simulation counter resets to zero so that each pair of plaquettes is exchanged for the new configuration. If no lower energy state is found after the requisite number of pairs are tested, the

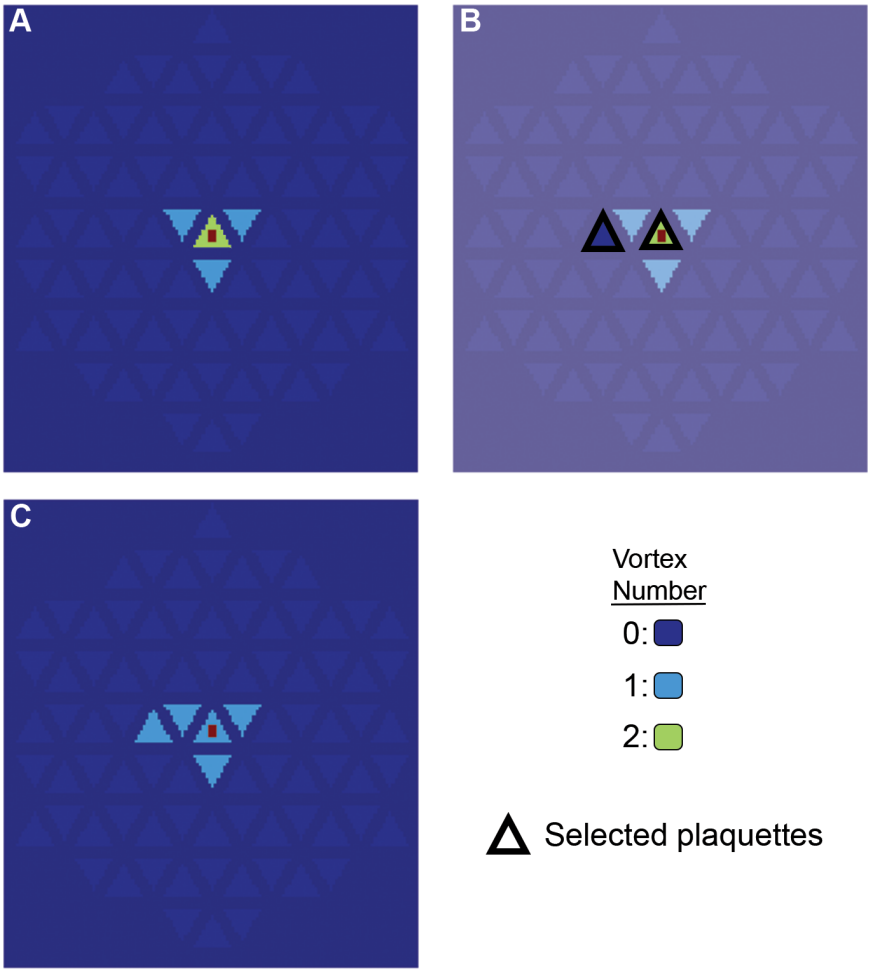

Figure 4.4: Illustration of increasing/decreasing the vorticity of plaquettes in pairs. (**A**) The system starts in some confguration. (**B**) A pair of plaquettes are chosen at random, and the vorticity is increased by one, and decreased on the other. (**C**) If the change in vorticities is accepted, the new configuration is used for the next step in the simulated annealing process.

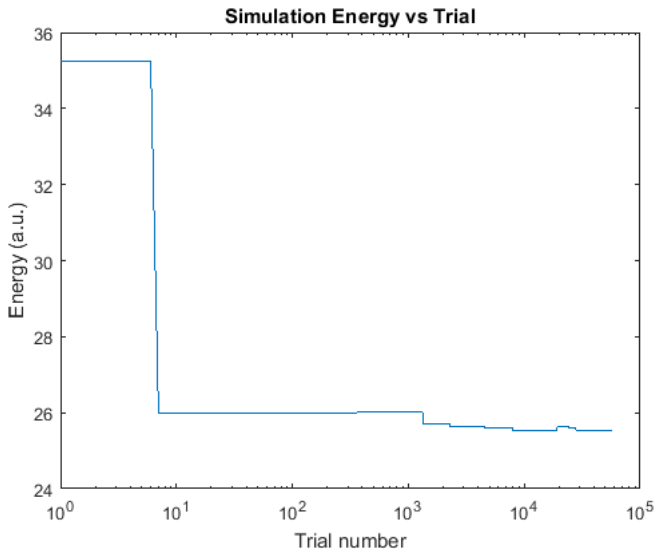

Figure 4.5: Example of the energy of the accepted vortex configuration vs. trial number.

configuration is taken as the lowest energy state for that tip location and external field. An example of the energy of the vortex configuration can be seen in Fig. 4.5

Once we have the lowest energy configuration at the first point, the tip field is moved to a new location to reflect motion of the cantilever. We take the previous configuration as the starting point for the configuration at this new location, and repeat the simulated annealing procedure. This is repeated for each point in the simulated scan area, which is a square encompassing one full plaquette, as well as extending past the edges of the plaquette by $\sim 15\%$ on all sides.

With the lowest energy configuration found at each point, the vortex configuration at each point is compared to the configuration in the adjacent points. If the vortex configuration changes between the points, the points are marked as locations where the vortex configuration changes. Plotting the locations of these configuration changes gives patterns like the one shown in Fig. 4.6, which match some of the observed patterns. By repeating this simulation procedure for different tip heights and external fields, we can find which patterns correspond to a given number of vortices trapped underneath the tip, as seen in Fig. 4.7. We can also note that these simulations match the observed patterns well, showing that the approximations made earlier are reasonable for these patterns. By this method, the configurations of vortex numbers between 2 and 8 were calculated. Greater vortex numbers are possible, with added annealing time typically being necessary for increasing vortex number.

The results of the simulated annealing procedure give results that qualitatively match many of the patterns that are observed in the experiment, but do not quantitatively predict the patterns to occur with

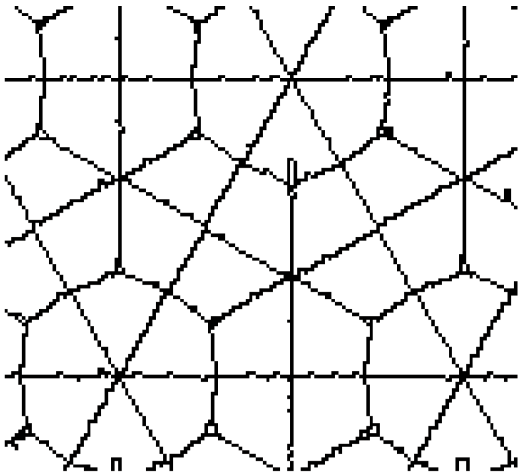

Figure 4.6: A pattern generated by the simulated annealing, with five vortices trapped underneath the tip. One full plaquette is simulated, with the vertices of the plaquette (islands) located at the center of the circular areas where the lines cross.

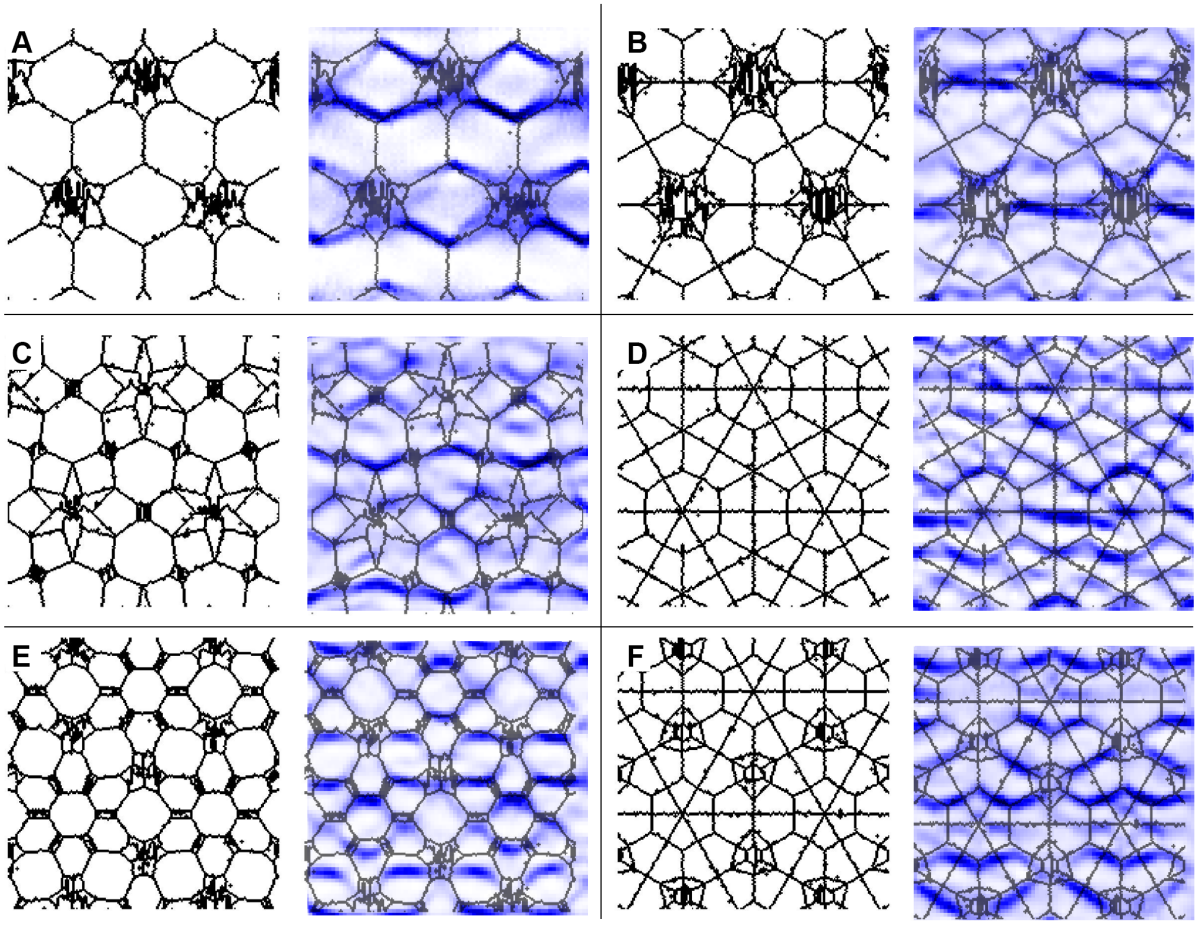

Figure 4.7: Matching number of vortices in a simulation to experimental patterns. (**A**) 2 vortices underneath the tip, and associated experimental pattern. (**B**) 3 vortices (**C**) 4 vortices (**D**) 5 vortices (**E**) 6 vortices (**F**) 7 vortices.

the same parameters as in experiment. For the simulated annealing, the external field required to generate a particular vortex pattern at a given tip height is not accurate. Additionally, the number of vortices in one simulated scan is fixed, preventing simulation of experimental patterns that have vortex configurations with differing vortex number in different areas of the image. To address these drawbacks, as well as reduce noise in the simulated images from the possible acceptance of states that are not locally the lowest energy, a second energy minimization procedure was adopted.

4.5 Energy Minimization and Change of Vortex Number

From the simulated annealing procedure discussed above, many vortex configurations were found for different numbers of vortices trapped underneath the tip. Taking all of the vortex configurations that the simulated annealing gave for the lowest energy at any point in the simulated images, we have a large list of vortex configurations that we can work with. By finding the energy of each configuration at a given tip position, tip height, and external field, we can find the configuration with the minimum energy, regardless of vortex number.

Implementing this procedure with the the energy as given in Eq. 4.14 still results in a mismatch between the experimental and simulated external fields where a given pattern will appear. We modify the energy with a "chemical potential" term, and add a parameter, p, in front of the vortex-vortex interaction term (V_{ij} term) that can be used to adjust the relative strength of that term relative to the vortex-field interaction (the U_i term). With those additions, the energy is now:

$$F = \sum_{i=1}^{N} U_i n_i + p \sum_{i,j=1}^{N} V_{ij} n_i n_j + \sum_i \mu n_i \tag{4.15}$$

where μ is the "chemical potential". We have also dropped the F_0, as it is the same for all configurations. With this addition, we can adjust p and μ to match the simulation to experiment at the correct external field and tip height values. By modifying p and μ, we can extract the relative energy scales of the system, telling us the relative strengths of different vortex interactions based on where the patterns appear in field and height space. For this system in particular, we can determine if vortex-field or vortex-vortex interactions differ from the values we would expect based on our theoretical interpretation. We can also extract the chemical potential of the system at the same time. In plotting the location of the configuration changes, we calculated an approximation of the force on the cantilever from the currents circulating in the array. We only plot configuration changes for which the change in force would act along the cantilever oscillation direction, to better fit the experimental data. In addition, we do not plot transitions where the energy

difference between the first two excited energy levels is small, reflecting the possible issue of the system moving non-resonantly between three or more states.

Using this calculation to match patterns and fields results in agreement of field and height values to within a few Oerstead in field, and about 10 nm in height, with the correct selection of p and μ. Matching of patterns between the energy minimization simulation and experimental patterns can be seen in Figs. 3.4, 3.13, and 3.14. Currently, the technique has not been used to match vortex patterns at the $f + 1$ fields, as that requires tracking the absence of anti-vortices. Such matching should be possible if the simulations are modified.

For arrays with lattice spacing of 500 nm, good agreement between simulated and experimental external fields are found with $p \sim 1.0$ and $\mu = (1.8 \pm 0.1)V_{11}$, where V_{11} is the energy of a single vortex in the array with no external or tip fields applied. Uncertainty in the values are due to the experimental and simulated patterns agreeing for multiple values of μ and p, as well as possible errors in determining the magnetic field of the tip. No dependence of μ on the number of vortices was found for the vortex numbers simulated. Arrays with lattice spacings of 440 nm and 560 nm were also simulated to compare to experiment. As stated previously, the 440 nm array requires more field to induce a vortex in a plaquette, and the Josephson coupling between Nb islands will be stronger vs. a 500 nm array. Opposite effects will be observed in the 560 nm array. The fields required to generate corresponding patterns to the experimental data are different for these array spacings, as predicted. Extracting the values of p and μ for these arrays leads us to find that $\mu = 0.9 \pm 0.1V_{11}$ for the 560 nm array, with $p \sim 0.7 - 0.9$, showing weaker vortex-vortex interactions vs. the vortex-field energies for this array as compared to the 500 nm lattice spacing. The simulations also show that p is dependent on field, and decreases while the externally applied magnetic field is increased. For the 440 nm lattice spacing, we find $\mu = 2.4 \pm 0.1V_{11}$, with $p \sim 1.2 - 1.4$, showing stronger vortex-vortex interactions compared to those in the other lattice spacings. We also find that p increases for increasing external magnetic fields for this lattice spacing. A summary of results can be found in Table 4.1.

Spacing	p	μ
440 nm	1.2-1.4	$(2.4 \pm 0.1)V_{11}$
500 nm	1	$(1.8 \pm 0.1)V_{11}$
560 nm	0.7-0.9	$(0.9 \pm 0.1)V_{11}$

Table 4.1: Values of the vortex-vortex interaction scaling and chemical potential with respect to the vortex-field interaction strength for three array spacings.

Chapter 5

Conclusions and future work

5.1 Summary of results

We have studied the vortex dynamics of small numbers of vortices trapped underneath a magnetic tip and moving between sites on a superconductor. This superconducting surface, created from a triangular array of Josephson junction fabricated from Nb islands on Au, gives a washboard-type potential for vortices to sit in. As the magnetic tip is scanned across the surface at a temperature slightly below T_c, points where the energies of two vortex configurations become equal appear as shifts in frequency of the cantilever due to the vortex configurations changing in resonance with the cantilever. We term this effect Stochastic Resonance Magnetic Force Microscopy. Mapping these points of energy degeneracy gives rise to patterns in the frequency image which reflect the vortex configurations and number of vortices trapped underneath the cantilever. A background subtraction method is used to highlight these patterns.

By adjusting the external magnetic field applied to the sample, the number of vortices trapped underneath the tip, and therefore the patterns seen, change. Using a simulated annealing procedure along with a simple model for the current/phase relation in the superconductor, patterns are generated which match well to those found in the experimental data. From these patterns, both the number of vortices trapped underneath the tip and the vortex configuration(s) at each point in the experimental images can be determined. We find that the patterns seen are generally due to a small number (1 to ~ 12) vortices trapped underneath the tip.

Adjustments of the height of the tip, as well as the lattice spacing of the Josephson junction array, can change the vortex configurations present in the array. For smaller tip heights, the field from the tip is greater, and the potential well generated is deep, leading to vortex configurations that are tightly packed. Larger tip heights have lower field values, and the potential well is flatter, giving rise to vortex configurations where the vortices may spread out more. These effects are seen in both the experimental data and simulations. Lattice spacing is also adjusted to be smaller and larger, giving rise to various effects similar to those above.

Using an energy minimization procedure based on the vortex configurations generated by the simulated annealing calculations, the minimum energy configuration and number can be found simultaneously. By

fitting the patterns generated by the minimization procedure to those seen in experiment, the relative energy scales of the system can be extracted. The energy scales for this experiment are the field-vortex interaction, the vortex-vortex interaction, and the chemical potential term. The chemical potential of the system appears to be independent to the external field, while the relative strength of the three terms vary with lattice spacing.

5.2 Future Work

With a new technique for measuring the energy degeneracy points of a small number of vortices, along with a way to manipulate the vortex configuration, many avenues for research are open. One avenue that is planned for exploration in the near future is using the stochastic resonance technique on superconductors paired with topological insulators (TIs). TIs coupled to superconductors are predicted to display Majorana modes[14,112], which we may be able to investigate with this technique. Samples such as those required for our system are currently being studied by the Mason group, and the design should be easily modified to work in our MFM microscope.

More theoretical work to achieve more agreement between the simulations and experiment is also an avenue to explore. The non-sinusoidal equations derived in Chap. 4 may not conform to the real experimental systems in situations where the phase difference between islands is large. Additionally, our simulations produce extra lines in many of the patterns that do not appear in the experimental images. This could be due to extraneous transitions, or due to a force below our detection threshold. A more accurate theoretical treatment may be able to resolve these issues and make more accurate predictions on the vortex configurations, degeneracy points, and forces on the cantilever.

This technique could be utilized for some basic quantum computing applications as well. Knowledge of the vortex configurations at each point may allow a particular vortex configuration to be created with the tip, and motion of the tip along a preselected path will move vortices in a controllable manner, possibly allowing braiding of two or more vortices. A readout scheme would need to be included near the array, as the cantilever is not sensitive to phase changes in the array. Manipulation of vortex states in multipart ring structures have been investigated by Hryhoriy Polshyn in our group, though using a standard s-wave superconductor, and a readout scheme has not been implemented at this time. Further afield, exotic superconductors, such as Sr_2RuO_4, may contain multiple superconducting condensates owing to their non-standard superconductivity and possible chiral nature[5,13,76,91,113]. Investigation of these exotic superconductors may be of interest to determine if we can resolve the individual condensates and probe their interactions.

Appendix A

Estimating the tip field

A.1 Tip field approximations

Determination of the magnetic field emanating from an MFM tip is a difficult exercise, requiring information on the internal microstructure of the magnetic tip. Generally, this microstructure is not known, and a number of approximation schemes have been used to extract quantitative results from MFM data. One of the most popular approximation schemes is the point-probe model, where the tip is assumed to be a magnetic monopole and/or dipole [95,114,115]. This model makes quantitative predictions only in a small volume, and is not accurate outside this volume. A more complicated model, where the magnet is approximated by a prolate spheroid that is uniformly magnetized, can also be used in a small volume near the tip of the probe, with interactions outside this volume being neglected [95]. These approximations work well in certain instances, such as for a Fe-filled carbon nanotube [116], but are less ideal for general tip shapes.

To move beyond these approximations and their limitations, numerical calculations based on probe geometry have been performed to attempt to determine the magnetic field from various tip shapes [115]. By using a sample with a known magnetic field profile, such as that from a thin current carrying line, the magnetic structure of the probe can be determined [117,118]. Since the response of the cantilever is determined by a convolution of the tip magnetization with the field from the surface, knowledge of the field generated by the sample allows for extraction of the tip magnetization and geometry. Simplification of the numerical calculations can be achieved by approximating the tip volume as a number of cubical magnetic elements.

A.2 Experimental setup for approximation

To calibrate the tips used in our experiments, we used a similar approach to the numerical calculations. A current carrying line with known magnetic structure was not used, however. To determine the magnetic fields of the tips, thin walled superconducting rings were imaged. These rings, an example of which can be seen in Fig. A.1, which varied in diameter from 1μm to 5μm, were made from superconducting Al, with

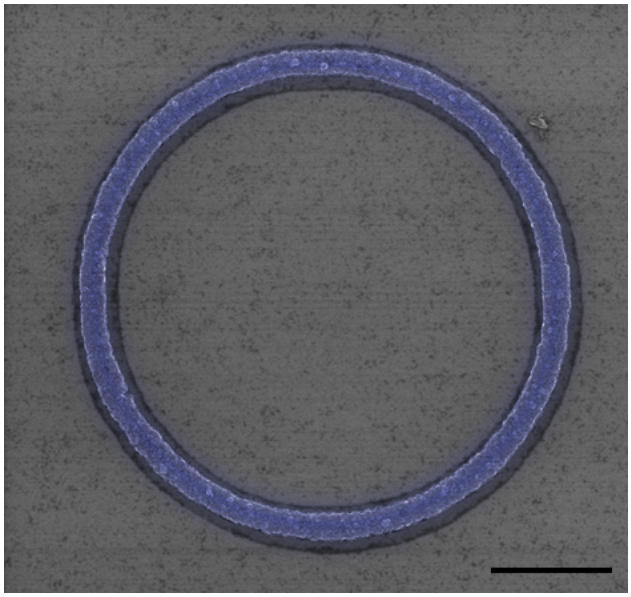

Figure A.1: An example ring of 4 μm diameter and 200 nm wall thickness. Rings with diameters of 1 to 5 μm were scanned, with wall widths of 100 to 200 nm. Scale bar is 1 μm.

wall widths of 100 to 200 nm, and a height of 50 nm. The Al was deposited via thermal or electron beam evaporation (dependent on sample), with a 5 nm sticking layer of Cr or Ti underneath to promote adhesion to the SiO_2 substrate. Rings were evaporated prior to the Au/Nb deposition, and were greater than 10 μm away from the edges of the Nb island arrays.

Scanning of the rings is done in the same way as for the arrays. The rings are raster scanned at a set offset height, with the fast axis and tip oscillations in the $\hat{y}$-direction. The external field is generally set to zero for these measurements, and the temperature is set slightly below T_c for the rings. T_c of the rings is measured by moving the tip over the wall of the ring and observing the cantilever frequency while the temperature is varied. The frequency of the cantilever will begin to shift at the transition temperature of the Al, as can be seen in Fig. A.2. The proximity of the tip did not significantly shift T_c, as determined by repeating the experiment at several tip heights. This frequency shift is due to supercurrents circulating in the ring[106].

Similarly to the patterns seen in the array, concentric circular bands of shifted frequency appear in the images of the rings, as seen in Fig. A.3. A brief explanation of these patterns follows, and a detailed explanation of the formation of these rings can be found in H. Polshyn *et al.*[106] for the interested reader. While scanning over the ring, the tip will move to a position where the flux penetrating the ring is equal to $(n + 1/2)\Phi_0$, where n is an integer. At these locations, the oscillation of the tip, combined with thermally activated phase slips (TAPS), cause fluxoid transitions in the ring. These fluxoid transitions are accompanied

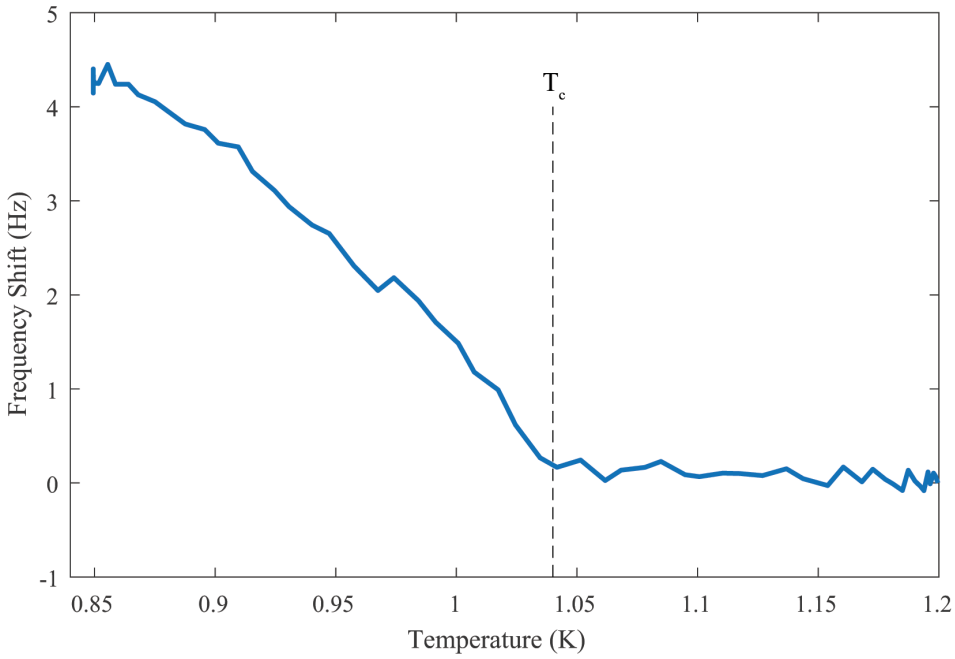

Figure A.2: Frequency vs. temperature for a ring similar to that in Fig. A.1. The cantilever is positioned over the wall of the ring as the temperature is changed. At T_c, the frequency of the cantilever starts to shift due to supercurrents in the ring.

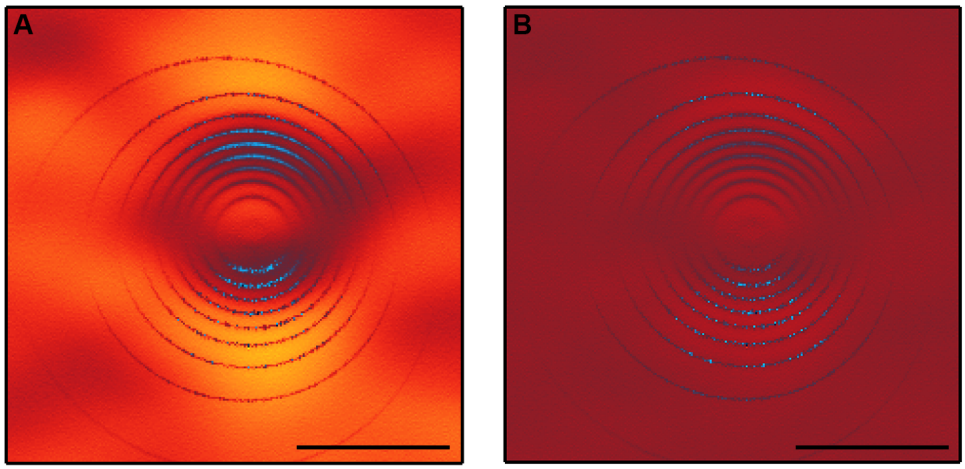

Figure A.3: Example of the frequency image while scanning a 2 μm ring slightly below T_c. At left is the raw frequency image. At right is the frequency image with a slowly varying background from topography subtracted off, highlighting the fluxoid transitions. Scale bars are 2 μm.

by a change in the current circulating around the ring, which changes the force on the cantilever in sync with the cantilever. This change in force causes a change in the cantilever frequency, resulting in the circular bands seen. Along the horizontal axis of the ring, there are no frequency shifts, since the cantilever oscillation does not result in a change in flux at those points. The images of the rings therefore show where the flux penetrating the ring is equal to $(n + 1/2)\Phi_0$, which we use to determine the profile of the magnetic field from the tip.

A.3 Tip modeling

By constructing a model of a magnetic tip and determining that magnetic field from that model, we can then find the magnetic flux penetrating a ring of equal size to that in the experiment, and compare the locations where the flux is equal to $(n+1/2)\Phi_0$ with experiment. A numerical model of the tip was constructed, with geometry based on SEM images of the magnetic tip from the focused ion beam shaping process. The model tip was formed from cubical dipolar elements with 50 nm sidelength, the strength of which could be adjusted to fit the experimental flux. The overall magnetization of the tip was set using the values measured using cantilever magnetometry.

In fitting the flux, n at the edges of the image was taken to be 0. The flux was calculated for several different heights, and the position of the simulated flux transitions matched to the experimental transitions, as seen in Fig. A.4. Field profiles at several heights for the two tips under consideration can be seen in Fig. A.5. These field profiles are used in the simulated annealing and energy minimization calculations described in Chap. 4.

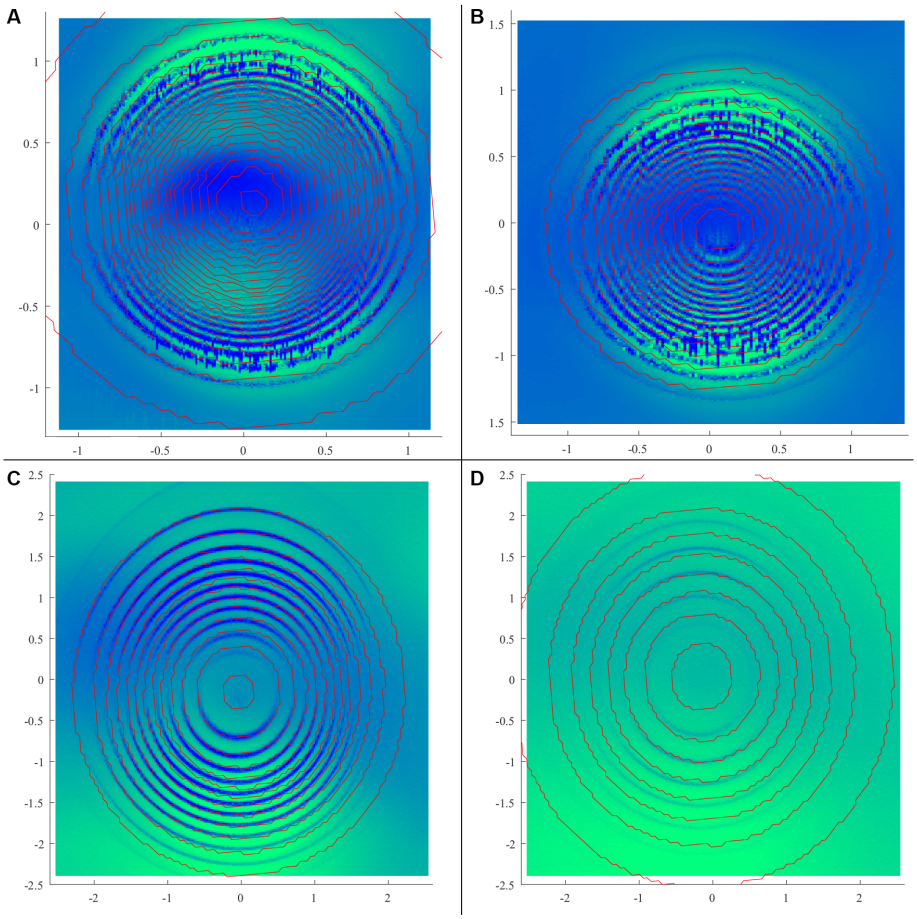

Figure A.4: Simulated fluxoid transitions (red) overlaid on frequency data for different rings and scanning heights. (**A**) Scan 300 nm above the surface of a 1 μm ring. (**B**) Scan 400 nm above the surface of a 1 μm ring. (**C**) Scan 800 nm above the surface of a 3 μm ring. (**D**) Scan 1200 nm above the surface of a 3 μm ring. All fits done for the tip shown in Fig. 2.9B.

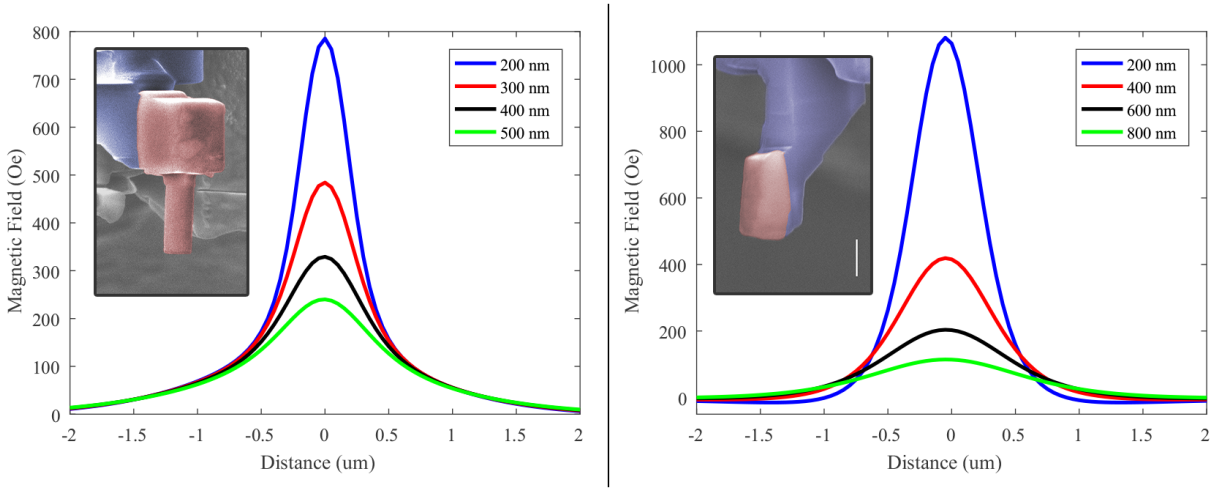

Figure A.5: One dimensional field profiles for two magnetic tips. Distance is measured from center of tip. SEM images of each tip are inset.

References

[1] L. Embon, Y. Anahory, A. Suhov, D. Halbertal, J. Cuppens, A. Yakovenko, A. Uri, Y. Myasoedov, M. L. Rappaport, M. E. Huber, A. Gurevich, and E. Zeldov. Probing dynamics and pinning of single vortices in superconductors at nanometer scales. *Scientific Reports*, 5, 2015.

[2] G. Blatter, M. V. Feigel'man, V. B. Geshkenbein, A. I. Larkin, and V. M. Vinokur. Vortices in high-temperature superconductors. *Reviews of Modern Physics*, 66(4), 1994.

[3] C.-S. Lee, B. Jankó, I. derényi, and A.-L. Barabási. Reducing vortex density in superconductors using the 'ratchet effect'. *Nature*, 400, 1999.

[4] D. F. Agterberg. Vortex lattice structures of Sr_2RuO_4. *Physical Review Letters*, 80(23), 1998.

[5] T. M. Riseman, P. G. Kealey, E. M. Forgan, A. P. Mackenzie, L. M. Galvin, A. W. Tyler, S. L. Lee, C. Ager, D. McK. Paul, C. M. Aegerter, R. Cubitt, Z. Q. Mao, T. Akima, and Y. Maeno. Observation of a square flux-line lattice in the unconventional superconductor Sr_2RuO_4. *Nature*, 396, 1998.

[6] Liviu F Chibtaru, Arnout Ceulemans, Vital Bruyndoncx, and Victor V Moshchalkov. Symmetry-induced formation of antivortices in mesoscopic superconductors. *Nature*, 408, 2000.

[7] M. Dolz, D. Antonio, and H. Pastoriza. Measurement of mesoscopic high-T_c superconductors using Si mechanical micro-oscillators. *Physica B*, 398, 2007.

[8] Tyler Morgan-Wall, Benjamin Leith, Nikolaus Hartman, Atikur Rahman, and Nina Marković. Measurement of critical currents of superconducting aluminum nanowires in external magnetic fields: evidence for a Weber blockade. *Physical Review Letters*, 114, 2015.

[9] C. A. Bolle, V. Aksyuk, F. pardo, P. L. Gammel, E. Zeldov, E. Bucher, R. Boie, D. J. Bishop, and D. R. Nelson. Observation of mesoscopic vortex physics using micromechanical oscillators. *Nature*, 399, 1999.

[10] I. V. Grigorieva, W. Escoffier, J. Richardson, L. Y. Vinnikov, S. Dubonos, and V. Obozmov. Direct observation of vortex shells and magic numbers in mesoscopic superconducting disks. *Physical Review Letters*, 96, 2006.

[11] A. Kanda, B J. Baelus, F. M. Peeters, K. Kadowaki, and Y. Ootuka. Experimental evidence for giant vortex sates in a mesoscopic superconducting disk. *Physical Review Letters*, 93, 2004.

[12] D. J. Resnick, J. C. Garland, J. T. Boyd, S. Shoemaker, and R. S. Newrock. Kosterlitz-Thouless transition in proximity-coupled superconducting arrays. *Physical Review Letters*, 47, 1981.

[13] Andrew Peter Mackenzie and Yoshiteru Maeno. The superconductivity of Sr_2RuO_4 and the physics of spin-triplet pairing. *Reviews of Modern Physics*, 75, 2003.

[14] Joel E. Moore. The birth of topological insulators. *Nature*, 464, 2010.

[15] V. Mourik, K. Zuo, S. M. Frolov, S. R. Plissard, E. P. A. M. Bakkers, and L. P. Kouwenhoven. Singatures of Majorana fermions in hybrid superconductor-semiconductor nanowire devices. *Science*, 336, 2012.

[16] A. D. K. Finck, D. J. Van Harlingen, P. K. Mohseni, K. Jung, and X. Li. Anomalous modulation of a zero-bias peak in a hybrid nanowire-superconductor device. *Physical Review Letters*, 100, 2013.

[17] Stevan Nadj-Perge, Ilya K. Drozdov, Jian Li, Hua Chen, Sangjun Jeon, Jungpil Seo, Allan H. MacDonald, B. Andrei Bernevig, and Ali Yazdani. Observation of Majorana fermions in ferromagnetic atomic chains on a superconductor. *Science*, 346, 2104.

[18] Xiao-Fei Zhang, Wei Han, Lin Wen, Peng Zhang, Rui-Fang Dong, Hong Chang, and Shou-Gang Zhang. Two-component dipolar Bose-Einstein condensate in concentrically coupled annular traps. *Scientific Reports*, 5, 2015.

[19] Davi S. Dantas, Aristeu R. P. Lima, A. Chaves, C. A. S. Almeida, G. A. Farias, and Milošević. Bound vortex states and exotic lattices in multicomponent Bose-Einstein condensates: The role of vortex-vortex interaction. *Physical Review A*, 91, 2015.

[20] Kenchi Kasamatsu, Makoto Tsubta, and Masahito Ueda. Vortex phase diagram in rotating two-component Bose-Einstein condensates. *Physical Review Letters*, 91(15), 2003.

[21] Simon J. Bending. Local magnetic probes of superconductors. *Advances in Physics*, 48(4), 1999.

[22] H. F. Hess, R. B. Robinson, R. C. Dynes, J. M. Valles, Jr., and J. V. Waszczak. Scanning-tunneling-microscope observation of the Abrikosov flux lattice and the density of states near and inside a fluxoid. *Physical Review Letters*, 62(2), 1989.

[23] Serena Eley, Sarang Gopalakrishnan, Paul M. Goldbart, and Nadya Mason. Approaching zero-temperature metallic states in mesoscopic superconductornormal superconductor array. *Nature Physics*, 2012.

[24] Serena Eley. *Proximity Effects and Vortex Dynamics in Mesoscopic Superconductor-Normal Metal-Superconductor Arrays.* PhD thesis, University of Illinois at Urbana-Champaign, 2012.

[25] R. S. Newrock, C. J. Lobb, U. Geigenm uller, and M Octavio. The two-dimensional physics of Josephson junction arrays. In Henry Ehrenreich and Frans Spaepen, editors, *Solid State Physics*, volume 54, pages 263–512. Academic Press, 2000.

[26] W. J. Zhang, S. K. He, H. Xiao, G. M. Xue, Z. C. Wen, X. F. Han, S. P. Zhao, C. Z. Gu, and X. G. Qiu. Transport measurements on nano-engineered two dimensional superconducting wire networks. *Physica C*, 480, 2012.

[27] V. V. Moshchalkov, V. Bruyndoncx, L. Van Look, M. J. Van Bael, Y. Bruynseraede, and A. Tonomura. Quantization and confinement phenomena in nanostructured superconductors. In H.S. Nalwa, editor, *Handbook of Nanostructured materials and nanotechnology*, volume 3: Electrical Properties, chapter 9. Academic Press, 2000. ISBN: 0-12-513763-X.

[28] H. D. Hallen, R. Seshadri, A. M. Chang, R. E. Miller, L. N. Pfeiffer, K. W. West, C. A. Murray, and H. F. Hess. Direct spatial imaging of vortices in a superconducting wire network. *Physical Review Letters*, 71(18), 1993.

[29] G. Binnig, C. F. Quate, and Ch. Gerber. Atomic force microscope. *Physical Review Letters*, 56(9), 1986.

[30] T. R. Albrecht, P. Grütter, D. Horne, and D. Rugar. Frequency modulation detection using high-Q cantilever for enhanced force microscope sensitivity. *Journal of Applied Physics*, 69(2), 1991.

[31] B. T. Matthias, T. H. Geballe, and V. B. Compton. Superconductivity. *Reviews of Modern Physics*, 35(1), 1963.

[32] Charles P. Editor Poole, Jr. *Handbook of Superconductivity.* Elsevier, 2000.

[33] Michael Tinkham. *Introduction to superconductivity.* Dover, New York, second edition edition, 2004.

[34] Yoichi Kamihara, Hidenori Hiramatsu, Masahiro Hirano, Ryuto Kawamura, Hiroshi Yanagi, Toshio Kamiya, and Hideo Hosono. Iron-based layered superconductor: Laofep. *Journal of the American Chemical Society*, 128(31), 2006.

[35] Yoichi Kamihara, Takumi Watanabe, Masahiro Hirano, and Hideo Hosono. Iron-based layered superconductor la$[o_{1-x}f_x]$feas ($x = 0.05 - 0.12$) with $t_c = 26$ k. *Journal of the American Chemical Society*, 130(11), 2008.

[36] Leon N. Cooper. Bound electron pairs in a degenerate Fermi gas. *Physical Review*, 104, 1956.

[37] L. P. Gor'kov. Microscopic derivation of the Ginzburg-Landau equations in the theory of superconductivity. *Soviet Physics JTEP*, 36(9)(6), 1959.

[38] Ernst Helmut Brandt. Vortex-vortex interaction in thin superconducting films. *Physical Review B*, 79, 2009.

[39] M. Tinkham. Effect of fluxoid quantization on transitions of superconducting films. *Physical Review*, 129(6), 1963.

[40] E. H. Rhoderick. Resistance transitions of thin superconducting films in magnetic fields. *Proceedings of the Royal Society of London A*, 267, 1962.

[41] J. Pearl. Current distribution in superconducting films carrying quantized fluxoids. *Applied Physics Letters*, 5, 1964.

[42] F. Tafuri, J. R. Kirtley, P. G. Madaglia, P. Orgiani, and G. Balestrino. Magnetic imaging of Pearl vortices in artificially layered $(Ba_{0.9}Nd_{0.1}CuO_{2+x})_m/(CaCuO_2)_n$ systems. *Physical Review Letters*, 92(15), 2004.

[43] In-Cheol Baek, Young-Je Yun, and Mu-Yong Choi. Critical behaviors of triangular josephson junction arrays in a magnetic field. *Journal of Physics and Chemistry of Solids*, 67(13):172 – 174, 2006.

[44] S. P. Benz, M. S. Rzchowski, M. Tinkham, and C. J. Lobb. Critical currents in frustrated two-dimensional Josephson arrays. *Physical Review B*, 42(10), 1990.

[45] J. M. Kosterlitz and D. J. Thouless. Ordering, metastability and phase transitions in two-dimensional systems. *Journal of Physics C: Solid State Physics*, 6, 1973.

[46] R. Córdoba, T. I Baturina, J Sesé, A. Yu Mironov, J. M. De Teresa, M. R. Ibarra, D. A. Nasimov, A. K. Gutakovskii, A. V. Latyshev, I Guillamón, H. Suderw, S. Vieira, M. R. Bakalonov, J. J. Palacios, and V. M Vinokur. Magnetic field-induced dissipation-free state in superconducting nanostructures. *Nature Communications*, 4, 2013.

[47] B. D. Josephson. Possible new effects in superconductive tunnelling. *Physics Letters*, 1(7), 1962.

[48] Rosario Fazio and Gerd Schön. Quantum vortex dynamics in Josephson arrays and optical lattices. *Annalen der Physik*, 524(3-4), 2012.

[49] H. S. J. van der Zant, F. C. Fritschy, T. P. Orlando, and J. E. Mooij. Vortex dynamics in two-dimensional underdamped, classical Josephson-junction arrays. *Physical Review B*, 47(1), 1993.

[50] J. R. Phillips, H. S. J. van der Zant, J. White, and T. P. Orlando. Influence of induced magnetic fields on the static properties of Josephson-junction arrays. *Physical Review B*, 47(9), 1993.

[51] H.S.J. van der Zant, H.A. Rijken, and J.E. Mooij. Phase transition of frustrated two-dimensional josephson junction arrays. *Journal of Low Temperature Physics*, 82(1-2):67–92, 1991.

[52] C. D. Chen, P. Delsing, D. B. Haviland, Y. Harada, and T. Claeson. Flux flow and vortex tunneling in two-dimensional arrays of small josephson junctions. *Phys. Rev. B*, 54:9449–9457, Oct 1996.

[53] B. J. van Wees, H. S. J. van der Zant, and J. E. Mooij. Phase transitions in Josephson-tunnel-junction arrays at zero and full frustration. *Physical Review B*, 35(13), 1987.

[54] C. J. Lobb, David W. Abraham, and M. Tinkham. Theoretical interpretation of resistive transition data from arrays of superconducting weak links. *Physical Review B*, 27(1), 1983.

[55] M. S. Rzchowski, S. P. Benz, M. Tinkham, and C. J. Lobb. Vortex pinning in Josephson-junction arrays. *Physical Review B*, 42(4), 1990.

[56] J. E. Mooij, G. Sch on, A. Shnirman, T. Fuse, C. J. P. M. Harmans, H. Rotzinger, and A. H. Verbruggen. Superconductor-insulator transition in nanowires and nanowire arrays. *New Journal of Physics*, 17, 2015.

[57] H. S. J. van der Zant, M. N. Webster, J. Romijn, and J. E. Mooij. Vortices in two-dimensional superconducting weakly coupled wire networks. *Physical Review B*, 50(1), 1994.

[58] S. Alexander. Superconductivity of networks. a percolation approach to the effects of disorder. *Physical Review B*, 27(3), 1983.

[59] R. Rammal, T. C. Lubensky, and G. Toulouse. Superconducting networks in a magnetic field. *Physical Review B*, 27(5), 1983.

[60] L. N. Vu, M. S. Wistrom, and D. J. Van Harlingen. Scanning SQUID microsopy of vortex configurations in superconductor arrays. *Physica B*, 194-196, 1994.

[61] A. V. Silhanek, L. Van Look, S. Raedts, R. Jonckheere, and V. V. Moshchalkov. Guided vortex motion in superconductors with a square antidot array. *Physical Review B*, 68, 2003.

[62] A I. Buzdin. Multiple-quanta vortices at columnar defects. *Physical Review B*, 47(17), 1993.

[63] G. S. Mkrtchyan and V. V. Shmidt. Interaction between a cavity and a vortex in a superconductor of the second kind. *Soviet Physics JTEP*, 34(1), 1972.

[64] M. Baert, V. V. Metlushko, R. Jonckheere, V. V. Moshchalkov, and Y. Bruynseraede. Composite flux-line lattices stabilized in superconducting films by a regular array of artificial defects. *Physical Review Letters*, 74(16), 1995.

[65] C. C. de Souza Silva, B. Raes, J. Brisbois, L. R. E. Cabral, A. V. Silhanek, J. Van de Vondel, and V. V. Moshchalkov. Probing the low-frequency vortex dynamics in a nanostructured superconducting strip. *Physical Review B*, 94, 2016.

[66] M. Vélez, J. I. Martín, J. E. Villegas, A. Hoffmann, E. M. González, J. L. Vicent, and Ivan K. Schuller. Superconducting vortex pinning with artificial magnetic nanostructures. *Journal of Magnetism and Magnetic Materials*, 320, 2008.

[67] David J. Morgan and J. B. Ketterson. Asymmetric flux pinning in a regular array of magnetic dipoles. *Physical Review Letters*, 80(16), 1998.

[68] M. J. Van Bael, K. Temst, V. V. Moshchalkov, and Y. Bruynseraede. Magnetic properties of submicron co islands and their use as artificial pinning centers. *Physical Review B*, 59(22), 1999.

[69] M. J. Van Bael, J. Bekaert, K. Temst, L. Van Look, V. V. Moshchalkov, Y. Bruynerseaede, G. D. Howells, A. N. Grigorenko, S. J. Bending, and G. Borghs. Local observation of field polarity dependent flux pinning by magnetic dipoles. *Physical Review Letters*, 86(1), 2001.

[70] J. E. Villegas, Sergey Savel'ev, Franco Nori, E. M. Gonzalez, J. V. Anguita, R. García, and J. L Vicent. A superconducting reversible rectifier that controls the motion of magnetic flux quanta. *Science*, 302, 2003.

[71] A. M. Chang, H. D. Hallen, L. Harriott, H. F. Hess, H. L. Kao, J. Kwo, R. E. Miller, R. Wolfe, J. van der Zeil, and T. Y Chang. Scanning Hall probe miscocopy. *Applied Physics Letters*, 61(16), 1992.

[72] L. Thiel, D. Rohner, M. Ganzhorn, P. Appel, E. Neu, B. Müller, R. Kleiner, D. Koelle, and P. Malentinsky. Quantitative nanoscale vortex imaging using a cryogenic quantum magnetometer. *Nature Nanotechnology*, 2016.

[73] Matthew Pelliccione, Alec Jenkins, Preeti Ovartchaiyapong, Christopher Reetz, Eve Emmanouilidou, Ni Ni, and Ania C. Bleszynski Jayich. Scanned probe imaging of nanoscale magnetism at cryogenic temperatures with a single-spin quantum sensor. *Nature Nanotechnology*, 2016.

[74] H.J. Hug, A. Moser, I. Parashikov, B. Stiefel, O. Fritz, H.-J. Güntherodt, and H. Thomas. Observation and manipulation of vortices in a $YBa_2Cu_3O_7$ thin film with a low temperature magnetic force microscope. *Physica C*, 235-240, 1994.

[75] Ophir M. Auslaender, Lan Luan, Eric W.J. Straver, Jennifer E. Hoffman, Nicholas C. Koshnick, Eli Zeldov, Douglas A. Bonn, Ruixing Liang, Walter N. Hardy, and Kathryn A. Moler. Mechanics of individual isolated vortices in a cuprate superconductor. *Nature Physics*, 5, 2009.

[76] J. Jang, D. G. Ferguson, V. Vakaryuk, R. Budakian, S. B. Chung, P. M. Goldbart, and Y. Maeno. Observation of half-height magnetization steps in Sr_2RuO_4. *Science*, 331, 2011.

[77] L. Bossoni, P. Carretta, and M. Poggio. Vortex lattice melting of a $NbSe_2$ single grain probed by ultrasensitive cantilever magnetometry. *Applied Physics Letters*, 104, 2014.

[78] E. W. J. Straver, J. E. Hoffman, O. M. Auslaender, D. Rugar, and Kathryn A. Moler. Controlled manipulation of individual vortices in a superconductor. *Applied Physics Letters*, 93, 2008.

[79] J. R. Kirtley. Fundamental studies of superconductors using scanning magnetic imaging. *Reports of Progress in Physics*, 73, 2010.

[80] Dimitri Roditchev, Christophe Brun, Lise Serrier-Garcia, Juan Carlos Cuevas, Vagner Henrique Loiola Bessa, Milorad Vlado Milošević, François Debontridder, Vasily Stolyarov, and Tristan Cren. Direct observation of Josephson vortex cores. *Nature Physics*, 11, 2015.

[81] J. R. Kirtley, C. C. Tsuei, Ariando, H. J. J. Smilde, and H. Hilgenkamp. Antiferromagnetic ordering in arrays of superconducting π-rings. *Physical Review B*, 72, 2005.

[82] S.G. Lachenmann, T. Doderer, D. Hoffman, R. P. Huebener, P. A. A. Booi, and S. P. Benz. Observation of vortex dynamics in two-dimensional Josephson-junction arrays. *Physical Review B*, 50, 1994.

[83] B Raes, C. C. de Souza Silva, A. V. Silhanek, L. R. E. Cabral, V. V. Moshchalkoc, and J. Van de Vondel. Closer look at the low-frequency dynamics of vortex matter using scanning susceptibility microscopy. *Physical Review B*, 90, 2014.

[84] B. Raes, J. Van de Voldel, A. V. Silhanek, C. C. de Souza Silva, J. Gutierrez, R. B. G. Kramer, and V. V. Moshchalkov. Local mapping of dissipative vortex motion. *Physical Review B*, 86, 2012.

[85] Brian W. Gardner, Janice C. Wynn, D. A. Bonn, Ruixing Liang, W. N. Hardy, R. Kirtley, John, Vladimir G. Kogan, and Kathryn A. Moler. Manipulation of single vortices in $YBa_2Cu_3O_{6.354}$ with a locally applied magnetic field. *Applied Physics Letters*, 80(6), 2002.

[86] B. L. T. Plourde, D. J. Van Harlingen, N. Saha, R. Besseling, M. B. S. Hesselberth, and P. H. Kes. Vortex distributions near surface steps observed by scanning SQUID microscopy. *Physical Review B*, 66, 2002.

[87] A. Moser, H.J. Hug, B. Stiefel, and H.-J. Güntherodt. Low temperature magnetic force microscopy of $YBa_2Cu_3O_7$ thin films. *Journal of Magnetis and Magnetic Materials*, 190, 1998.

[88] M. Roseman and P. Grütter. Magnetic imaging and dissipation force microscopy of vortices on superconducting nb films. *Applied Surface Science*, 188, 2002.

[89] N. Read and Dmitry Green. Paired states of fermions in two dimensions with breaking of parity and time-reversal symmetries and the fractional quantum Hall effect. *Physical Review B*, 61(15), 2000.

[90] D. A. Ivanov. Non-Abelian statistics of half-quantum vortices in p-wave superconductors. *Physical Review Letters*, 86(2), 2001.

[91] Chetan Nayak, Steven H. Simon, Ady Stern, Michael Freedman, and Sankar Das Sarma. Non-Abelian anyons and topological quantum computation. *Reviews of Modern Physics*, 80, 2008.

[92] G. Binnig, H. Rohrer, Ch. Gerber, and E. Weibel. Surface studies by scanning tunneling microscopy. *Physical Review Letters*, 49(1), 1982.

[93] Dror Sarid. *Scanning Force Microscopy*. Oxford University Press, New York, revised edition edition, 1994.

[94] Y. Martin and H. K. Wickramasinghe. Magetic imaging by "force microscopy" with 1000 Å resolution. *Applied Physics Letters*, 50, 1987.

[95] U. Hartmann. Magnetic force microscopy. *Annual Review of Materials Science*, 1999.

[96] Robert W. Stark, Tanja Drobek, and Wolfgang M. Heckl. Thermomechanical noise of a free v-shaped cantilever for atomic-force microscopy. *Ultramicroscopy*, 86, 2001.

[97] Hans-Jürgen Butt, Brunero Cappella, and Michael Kappl. Force measurements with the atomic force microscope: Technique, interpretation and applications. *Surface Science Reports*, 59, 2005.

[98] A. DiCarlo, M. R. Scheinfein, and R. V. Chamberlin. Magnetic force microscope utilizing an ultrasmall-spring-constant vertically cantilevered tip. *Ultramicroscopy*, 47, 1992.

[99] Enrico Volterra and E. C. Zachmanoglou. *Dynamics of Vibrations*. Charles E. Merrill Books, Inc., Columbus, Ohio, 1965.

[100] Y. Martin, C. C. Williams, and H. K. Wickramasinghe. Atomic force microscope-force mapping and profiling on a sub 100-Å scale. *Journal of Applied Physics*, 61, 1987.

[101] J. Mertz, O. Merti, and J. Mlynek. Regulation of a microcantilever response by force feedback. *Applied Physics Letters*, 62, 1993.

[102] J. L. Santos, A. P. Leile, and D. A. Jackson. Optical fiber sensing with a low-finesse Fabry-Perot cavity. *Applied Optics*, 31(34), 1992.

[103] J. L. Garbini, Bruland K. J., W. M. Dougherty, and J. A. Sidles. Optimal control of force microscope cantilevers. I. Controller design. *Journal of Applied Physics*, 80, 1996.

[104] T. D. Stowe, K. Yasumura, T. W. Kenny, D. Botkin, K Wago, and D. Rugar. Attonewton force detection using ultrathin silicon cantilevers. *Applied Physics Letters*, 71, 1997.

[105] Eric R. I Abraham and Eric A. Cornell. Teflon feedthrough for coupling optical fibers into ultrahigh vacuum systems. *Applied Optics*, 37(10), 1998.

[106] Hryhoriy Polshyn, Tyler R. Naibert, and Raffi Budakian. Imaging phase slip dynamics in micron-size superconducting rings. *arXiv.org*, 2017.

[107] Luca Gammaitoni, Peter Hänngi, Peter Jung, and Fabio Marchesone. Stochastic resonance. *Reviews of Modern Physics*, 70(1), 1998.

[108] R. W. Shonkwile and F. Mendivil. *Explorations in Monte Carlo Methods*. Springer Science + Business Media, LLC, Dordrecht, Heidelberg, London, New York, 2009.

[109] Wenbin Yu, K. H. Lee, and D. Stroud. Vortex motion in Josephson-junction arrays near $f = 0$ and $f = 1/2$. *Physical Review B*, 47(10), 1993.

[110] C. J. Olson, C. Reichhardt, and Franco Nori. Nonequilibrium dynamic phase diagram for vortex lattices. *Physical Review Letters*, 81(17), 1998.

[111] T. Giamarchi and P. Le Doussal. Moving glass phase in driven lattices. *Physical Review Letters*, 76(18), 1996.

[112] Martine Leijnse and Karsten Flensberg. Introduction to tolological superconductivity and Majorana fermions. *Semiconductor Science and Technology*, 27, 2012.

[113] C. Kallin and A. J. Berlinsky. Is Sr_2RuO_4 a chiral p-wave superconductor? *J. Phys.: Condensed Matter*, 21, 2009.

[114] U. Hartmann. The point dipole approximation in magnetic force microscopy. *Physics Letters A*, 137(9), 1989.

[115] Thomas Häberle, Felix Haering, Holger Pfeifer, Luyand Han, Balati Kuerbanjiang, Ulf Wiedwald, Ulrich Herr, and Berndt Koslowski. Towards quantitative magnetic force microscopy: theory and experiment. *New Journal Of Physics*, 14, 2012.

[116] S. Vock, F. Wolny, T. Mühl, R. Kaltofen, L. Schultz, B. Büchner, C. Hassel, J. Lindner, and V. Neu. Monopolelike probes for quantitative magnetic force microscopy: calibration and application. *Applied Physics Letters*, 97, 2010.

[117] T. Göddenheinrich, H. Lemke, M. Mück, U. Hartmann, and C. Heiden. Probe calibration in magnetic force microscopy. *Applied Physics Letters*, 57, 1990.

[118] J. Lohau, S. Kirsch, A. Carl, and E. F. Wassermann. Quantitative determination of the magnetization and stray field of a single domain Co/Pt dot with magnetic force microscopy. *Applied Physics Letters*, 76(21), 2000.